Université de Montréal

Strain Ultrasound Elastography of Aneurysm Sac Content after Randomized Endoleak Embolization with Sclerosing and Non-sclerosing Chitosan-based Hydrogels in a Preclinical Model

Par
Lojan Sivakumaran

Sciences biomédicales, Faculté de médecine

Mémoire présenté en vue de l'obtention du grade de maîtrise en sciences biomédicales, option recherche clinique

Août 2020

Université de Montréal

Unité académique : Sciences biomédicales, option recherche clinique

---

Ce mémoire intitulé

Strain Ultrasound Elastography of Aneurysm Sac Content After Randomized Endoleak Embolization with Sclerosing and Non-sclerosing Chitosan-based Hydrogels in a Preclinical model

Présenté par
Lojan Sivakumaran

A été évalué par un jury composé des personnes suivantes

Dr Alain Rivard
Président-rapporteur

Dr Gilles Soulez
Directeur de recherche

Dre Sophie Lerouge
Codirecteur

Dr André Denault
Membre du jury

Permission was obtained from the faculty to submit the present mémoire in English.

Résumé

Mise en contexte : La réparation endovasculaire des anévrismes de l'aorte abdominale est limitée par le développement des endofuites, qui nécessite un suivi à long terme par imagerie. L'élastographie sonore de déformation a été proposée comme méthode complémentaire pour aider à la détection des endofuites et la caractérisation des propriétés mécaniques des anévrismes. On s'intéresse ici également à la possibilité de suivre l'embolisation des endofuites, qui est indiquée dans certains cas mais dont le succès est variable. Un nouvel agent d'embolisation a été récemment créé en combinant un hydrogel de chitosane radio-opaque (CH) et le sclérosant tetradecyl sulfate de sodium (STS), qui s'appelle CH-STS. Le CH-STS démontre des propriétés mécaniques in vitro favorables, mais son comportement in vivo et son effet sur l'évolution du sac par rapport à un agent non-sclérosant pourraient être mieux caractérisés. L'objectif de cette étude était la caractérisation des propriétés mécaniques des composantes des endofuites embolisées avec CH-STS et CH avec élastographie sonore de déformation.

Méthodologie : Des anévrismes bilatéraux avec endofuites de type I ont été créés au niveau des artères iliaques communes chez neuf chiens. Chez chaque sujet, une endofuite a été embolisée avec CH, et l'autre, avec CH-STS, d'une façon aléatoire et aveugle. Des images d'échographie duplex et des cinéloops pour élastographie sonore de déformation ont été acquis à 1 semaine, 1 mois, 3 mois et (chez 3 sujets) 6 mois post-embolisation. La tomodensitométrie a été faite à 3 mois et (si pertinente) 6 mois post-embolisation. L'histopathologie a été faite au sacrifice. Les études radiologiques et les données d'histopathologie ont été co-enregistrées pour définir trois régions d'intérêt sur les cinéloops : l'agent d'embolisation (au sacrifice), le thrombus intraluminal (au sacrifice) et le sac anévrismal (pendant chaque suivi). L'élastographie sonore de déformation a été faite avec les segmentations par deux observateurs indépendants. La déformation axiale maximale (DAM) a été le critère d'évaluation principal. Les analyses statistiques ont été faites avec des modèles mixtes linéaires généralisés et des coefficients de corrélations intraclasses (ICCs).

Résultats : Des endofuites résiduelles ont été trouvées dans 7/9 (77.8%) et 4/9 (44.4%) des anévrismes embolisés avec CH et CH-STS, respectivement. Le CH-STS a eu une DAM 66 % plus basse ($p < 0.001$) que le CH. Le thrombus a eu une DAM 37% plus basse ($p = 0.010$) que le CH et 77% plus élevée ($p = 0.079$) que le CH-STS. Il n'y avait aucune différence entre les thrombi associés avec les deux traitements. Les sacs anévrismaux embolisés avec CH-STS ont eu une DAM 29% plus basse ($p < 0.001$) que ceux embolisés avec CH. Des endofuites résiduelles ont été associées avec une DAM du sac anévrismal 53% plus élevée ($p < 0.001$). Le ICC pour la DAM a été de 0.807 entre les deux segmentations.

Conclusion : Le CH-STS confère des valeurs de déformations plus basses aux anévrismes embolisés. Les endofuites persistantes sont associées avec des déformations plus élevées du sac anévrismal.

Mots clés : élastographie, anévrisme, endovasculaire, aorte, embolisation, endofuite, chitosane, STS

Abstract

Background: Endovascular aneurysm repair (EVAR) is the modality of choice for the treatment of abdominal aortic aneurysms (AAAs). EVAR is limited by the development of endoleaks, which necessitate long-term imaging follow-up. Conventional follow-up modalities suffer from unique limitations. Strain ultrasound elastography (SUE) has been recently proposed as an imaging adjunct to detect endoleaks and to characterize aneurysm mechanical properties. Once detected, certain endoleaks may be treated with embolization; however, success is limited. In this context, the embolic agent CH-STS—containing a chitosan hydrogel and the sclerosant sodium tetradecyl sulphate (STS)—was created. CH-STS demonstrates favorable mechanical properties in vitro; however, its behavior in vivo and impact on sac evolution compared to a non-sclerosing chitosan-based embolic agent (CH) merit further characterization.

Purpose: To compare the mechanical properties of the constituents of endoleaks embolized with CH and CH-STS—including the agent, the intraluminal thrombus (ILT), and the overall sac—via SUE.

Methods: Bilateral common iliac artery aneurysms with type I endoleaks were created in nine dogs. In each animal, one endoleak was randomly embolized with CH, and the other with CH-STS. Duplex ultrasound (DUS) and radiofrequency cine loops were acquired at 1 week, 1 month, 3 months, and—in 3 subjects—6 months post-embolization. Contrast-enhanced CT was performed at 3 months and—where applicable—6 months post-embolization. Histopathological analysis was performed at time of sacrifice. Radiological studies and histopathological slides were co-registered to identify three regions of interest (ROIs) on the cine loops: embolic agent (at sacrifice), ILT (at sacrifice), and aneurysm sac (at all follow-up times). SUE was performed using segmentations from two independent observers on the cine loops. Maximum axial deformation (MAD) was the main outcome. Statistical analysis was performed using general linear mixed models and intraclass correlation coefficients (ICCs).

Results: Residual endoleaks were identified in 7/9 (77.8%) and 4/9 (44.4%) aneurysms embolized with CH and CH-STS, respectively. CH-STS had a 66 % lower MAD ($p < 0.001$) than CH. The ILT had a 37% lower MAD ($p = 0.010$) than CH and a 77% greater MAD ($p = 0.079$; trending towards significance) than CH-STS. There was no difference in the ILT between treatment groups. Aneurysm sacs embolized with CH-STS had a 29% lower MAD ($p < 0.001$) than those with CH. Residual endoleak increased MAD of the aneurysm sac by 53% ($p < 0.001$), regardless of the agent used. The ICC for MAD was 0.807 between readers' segmentations.

Conclusion: CH-STS confers lower strain values to embolized aneurysms. Persistent endoleaks result are associated with increased sac strain, which may be useful for clinical follow-up.

Key words: elastography, abdominal aortic aneurysm, EVAR, embolization, endoleak, chitosan, STS

Table of Contents

Résumé 5

Abstract 7

Table of Contents 9

Table List 13

Figure List 15

Acronyms and Abbreviations 23

Acknowledgments 25

Part I - Introduction 27

Chapter 1 – Summary 28

Chapter 2 – Abdominal Aortic Aneurysms 31

2.1 The Aorta 31

2.1.1 Anatomy and Physiology of the Circulatory System 31

2.1.2 Anatomy of the Aorta 33

2.1.3 Histology of the Aorta 36

2.2 Introduction to Abdominal Aortic Aneurysms 38

2.2.1 Definition 38

2.2.2 Epidemiology and Risk Factors 38

2.2.3 Pathophysiology 41

2.2.4 Complications of AAA 41

2.2.5 Clinical Presentation 43

2.2.6 Screening for AAAs 43

Chapter 3 – Treatment of Abdominal Aortic Aneurysms 45

3.1 Indications for Intervention 45

3.2 Open Aneurysm Repair 45

3.3 Endovascular Aneurysm Repair 46

3.4 Comparison of Open Aneurysm Repair and Endovascular Aneurysm Repair 49

Chapter 4 – Endoleaks 50
4.1 Definition and Types 50
4.2 Follow-up Timeline 51
4.3 Conventional Imaging Modalities for EVAR Follow-up 51
4.3.1 Computed Tomography 51
4.3.2 Magnetic resonance imaging 55
4.3.3. Ultrasound 57
4.4 Treatment of Endoleaks 61
4.4.1 Treatment of Type I Endoleaks 61
4.4.2 Treatment of Type II Endoleaks 62
4.4.3 Treatment of Type III Endoleaks 63
4.4.4 Treatment of Type IV Endoleaks 64
4.4.5 Treatment of Type V Endoleaks 64
4.5 A New Agent to Treat Endoleaks: CH-STS 64
4.5.1 Limitations of Current Embolic Agents for the Treatment of Type II Endoleaks 64
4.5.2 Development and Evaluation of CH-STS in vitro and in vivo 65
Chapter 5 – Elastography 67
5.1 Introduction to Elastography 67
5.2 Strain Imaging 71
5.3 Dynamic Elastography – Shear Wave Elastography 73
5.4 Quasi-static Elastography in Vessels: Non-invasive Vascular Elastography using a Lagrangian Speckle Model Estimator 75
5.5 Elastography in the Context of EVAR 76
Part II – Strain Ultrasound Elastography of Aneurysm Sac Content after Randomized Endoleak Embolization with Sclerosing and Non-sclerosing Chitosan-based Hydrogels in a Preclinical Model 79
Chapter 6 – Objectives and Hypotheses 80
6.1 Objectives 80
6.2 Hypotheses 80

Chapter 7 – Methodology....81
7.1 Timeline and Ethical Considerations....81
7.2 Preclinical Canine Aneurysm and Endoleak Model....81
7.3 Preparation of Agents and Endoleak Embolization....82
7.4 Imaging Follow-up and Sacrifice....83
7.4.1 Ultrasound Imaging: Parameters and Follow-up Timeline....83
7.4.2 CT Imaging....84
7.4.3 Sacrifice, Macroscopy and Histopathological Analysis....84
7.5 Elastographic Analysis....86
7.5.1 Defining Regions of Interest....86
7.5.2 Display of RF Data for Elastography and Image Co-registration....86
7.5.3 Static Ultrasound Elastography of the Regions of Interest....89
7.6 Statistical Analysis....94
7.7 Relationship with Other Investigations and Original Contribution....95
Chapter 8 – Results....97
8.1 Baseline Characteristics....97
8.2 Elastograms of the Embolic Agent ROI....99
8.3 Elastograms of the ILT ROI....101
8.4 Comparison of the Embolic Agents and the ILT....103
8.5 Elastographic Analysis of Aneurysm Sac ROI....103
8.6 Comparison Between Readers....108
Chapter 9 – Discussion....109
9.1 Orientation of Discussion Section....109
9.2 Summary of Results....109
9.3 Elastographic Analysis of the Embolic Agents....110
9.4 Elastographic Analysis of the ILT....111
9.5 Comparison of the Elastographic Properties of the Embolic Agents and the ILT....113

9.6 Elastographic Analysis of the Aneurysm Sac 114
9.7 Inter-observer Reliability 116
9.8 Study Limitations 117
9.8.1 Limitations of the Canine Model 117
9.8.2 Limitations of SUE 117
9.8.3 Limitations of the Experimental Design 118
9.9 Conclusion 119
Bibliography 121

Table List

Table 1 Origins of notable branches of the abdominal aorta and examples of end organs that they perfuse. The table was generated using descriptions from (48, 50). T: thoracic vertebra; L: lumbar vertebra. 35

Table 2 Computed tomography (CT) findings of endoleaks. Adapted from (126, 127). 54

Table 3 Brightness mode (B-mode), Duplex ultrasound (DUS), CT (computed tomography), and histopathological appearance of various regions of interest (ROIs) to be characterized by strain ultrasound elastography (agent, thrombus, and aneurysm sac), as well as other ROIs used to help delineate them (endoleak and stent-graft). * Measured at the most representative level per aneurysm. † CH (CH hydrogel embolic agent) and CH-STS (chitosan hydrogel embolic agent with STS) are radiopaque given that they contain Visipaque™ (for visibility under fluoroscopy); however, their radiopacity lasts for only 48 hours (225). ‡The aneurysm sac mechanical properties represent sac stability. To account for the heterogeneity of the composition of the aneurysm sac, the mechanical properties for three levels of the sac (proximal, middle, and distal) were measured. ¶ Endoleaks were not assessed as an ROI using elastography because they had already been characterized as regions of high deformation caused by the heterogeneous effects of signal decorrelation due to slow blood flow and the presence of immature thrombus (28, 29). 87

Table 4 Derivation of the strain (deformation) and shear elastography parameters obtained using strain ultrasound elastography using a Lagrangian speckle model estimator. ROI: Region of interest. 94

Table 5 Mean (± standard deviation) of the maximum axial deformation, range cumulative axial deformation, and range cumulative axial shear of the embolic agent region of interest, at sacrifice, stratified by type of embolic agent used and presence of residual endoleak, as determined by (A) reader GS and (B) reader LS. CH: Chitosan hydrogel embolic agent; CH-STS: Chitosan hydrogel with sodium tetradecyl sulphate embolic agent; n: number of aneurysms. 99

Table 6 Multivariable linear mixed-effects model demonstrating the effect of use of CH-STS (versus CH) on the elastographic parameters of maximum axial deformation, range cumulative axial deformation, and range cumulative axial shear of the embolic agent region of interest obtained using the segmentations by reader GS. The estimate for the predictor CH-STS refers to the percentage change of the outcome parameter when CH-STS is used. CH: Chitosan hydrogel embolic agent. CH-STS: Chitosan hydrogel with sodium tetradecyl sulphate embolic agent. 100

Table 7 Mean (± standard deviation) of the maximum axial deformation, range cumulative axial deformation, and range cumulative axial shear of the intraluminal thrombus region of interest stratified by type of embolic agent used and presence of endoleak at sacrifice as determined by (A) reader GS and (B) reader LS. CH: Chitosan hydrogel embolic agent. CH-STS: Chitosan hydrogel with sodium tetradecyl sulphate embolic agent. 101

Table 8 Multivariable linear mixed-effects model demonstrating the effect of embolization with CH-STS (versus CH) and presence of residual endoleak (versus not) on the elastographic parameters of maximum axial deformation, range cumulative axial deformation, and range cumulative axial shear of the intraluminal thrombus obtained using the segmentations performed by reader GS. The estimates for the non-intercept predictors refer to the percentage change of the outcome when CH-STS is used (in comparison to CH) or when a residual endoleak is present (in comparison to not). CH: Chitosan hydrogel embolic agent. CH-STS: Chitosan hydrogel with sodium tetradecyl sulphate embolic agent. 102

Table 9 Mean (± standard deviation) of the (A) maximum axial deformation, (B) range cumulative axial deformation, and (C) range cumulative axial shear of the aneurysm sac region of interest stratified by embolic agent used (CH versus CH-STS), presence of residual endoleak, and time, as obtained by reader GS. CH: Chitosan hydrogel embolic agent. CH-STS: Chitosan hydrogel with sodium tetradecyl sulphate embolic agent; n: number of aneurysms (with three observations per aneurysm). 104

Table 10 Mean (± standard deviation) of (A) maximum axial deformation, (B) range cumulative axial deformation, and (C) range cumulative axial shear of the aneurysm sac region of interest stratified by embolic agent, presence of residual endoleak, and time, as obtained by reader LS. CH: Chitosan hydrogel embolic agent. CH-STS: Chitosan hydrogel with sodium tetradecyl sulphate embolic agent; n: number of aneurysms (three observations per aneurysm).....105

Table 11 Multivariable linear mixed-effects model demonstrating the effect of embolization with CH-STS (vs. CH), presence of residual endoleak (vs. not), and time on the elastographic parameters of maximum axial deformation, range cumulative axial deformation, and range cumulative axial shear obtained using the segmentations by reader GS. The estimates for the non-intercept predictors refer to the percentage change of the outcome when the predictor is present. CH: Chitosan hydrogel embolic agent. CH-STS: Chitosan hydrogel with sodium tetradecyl sulphate embolic agent.....106

Table 12 Multivariable linear mixed-effects model examining the effect of embolization with CH-STS (vs. CH) and presence of residual endoleak (vs. not) on the elastographic parameters maximum axial deformation, range cumulative axial deformation, and range cumulative axial shear of the aneurysm sac obtained using the segmentations by reader GS. The estimates for the non-intercept predictors refer to the percentage change of the outcome when the predictor is present. CH: Chitosan hydrogel embolic agent. CH-STS: Chitosan hydrogel with sodium tetradecyl sulphate embolic agent. 107

Table 13 Intraclass correlation coefficients comparing the inter-observer reliability of the maximum axial deformation, range cumulative axial deformation, and range cumulative axial shear obtained from the segmentations performed by the readers GS and LS.....108

Figure List

Figure 1 Schematic representation of the different types of endoleaks. Type I endoleaks are caused by blood flow into the aneurysm sac along the proximal or distal attachment sites of the EVAR stent, termed type Ia and type Ib endoleaks, respectively. Type II endoleaks are caused by collateral, retrograde flow into the aneurysm sac from a vessel that once was supplied by the aneurysm sac, such as the inferior mesenteric artery. Type III endoleaks are due to graft tears or component separation of the EVAR stent. Type IV endoleaks are caused by the transient passage of blood through pores in the stent graft during deployment on angiography. Type V endoleaks, also termed endotension, entail enlargement of the sac without blood flow visualized into the sac on imaging. Adapted from (101). EVAR: Endovascular aneurysm repair. 29

Figure 2 Schematic of the circulatory system. The pulmonary circulation and the systemic circulation are organized in series with the heart, which acts as a central pump. Within the systemic circulation, there are several parallel circuits supplying different organ systems. In general, blood is distributed by the arterial system to the peripheral tissues, where—at the level of the capillary—gas, nutrient, and waste exchange occurs. Blood is then returned to the heart via the venous system. There are several exceptions to this rule—such as in the digestive and the renal systems, where there is more than one capillary network and complex arterial inputs—but this is beyond the scope of the present document. Adapted from (46). 32

Figure 3 Illustration of the abdominal aorta with several its branches. The abdominal aorta originates at the aortic hiatus (at the level of the 12th thoracic vertebra) and terminates at the bifurcation of the common iliac vessels at (at the level of the 4th lumbar vertebra). Branches arise from the anterior, lateral, and posterolateral aspects of the abdominal aorta. Adapted from (48). 34

Figure 4 Illustration demonstrating the various layers of a representative artery, including the tunica intima, tunica media, and tunica adventitia. Adapted from (44). 36

Figure 5 The aorta is considered an elastic artery given its high content of elastin fibers. (A) Schematic of elastin in its relaxed and stretched states. The tendency for elastin to return to its relaxed state allows for recoil of the aorta during the cardiac cycle. Adapted from (55). (B) Histopathological slide of the human aorta that has been stained dark purple for elastic fibers. The aorta is rich in elastin, which provides resilience and elastic recoil. The superior aspect of the image is the vessel lumen and the inferior aspect of the image is the adventitia. Deep to the endoluminal surface, there is well-developed internal elastic lamina (arrow). Beneath this structure, the thick media contains several dark purple, undulating lines corresponding to layers of elastin fibers. Along the superficial aspect of the vessel, the elastic fibers can be seen blending with the adventitia. Adapted from (44).....37

Figure 6 Abdominal aortic aneurysms (AAAs) may be classified with respect to their location relative to the renal arteries. Suprarenal AAAs extent superiorly to the renal arteries and can involve visceral branches

such as the superior mesenteric artery or celiac artery. In pararenal AAAs, the renal arteries are involved but the aneurysmal dilatation does not extend superiorly to them. Juxtarenal AAAs extent to involve just the inferior aspect of the renal arteries. Infrarenal AAAs, the most common type of AAAs, begin at least 1 cm distal to the renal arteries. All aneurysm shown are of the fusiform morphology, although saccular aneurysms are possible. Finally, aneurysms may extend inferiorly to the common iliac arteries (or even more distal branches). Adapted from (67). 39

Figure 7 Abdominal aortic aneurysm (AAA) rupture. (A) Schematic of focal discontinuity within the wall of an abdominal aortic aneurysm indicating rupture. C: calcifications, which are displaced. (B) and (C) Contrast enhanced axial computed tomography angiogram images demonstrating rupture of an AAA. In (B), iodinated contrast material—which under normal circumstances is found within the confines of the arterial system on arterial imaging—is visualized leaving the confines of the enlarged, dysmorphic AAA lumen (L) and travelling into the retroperitoneum (R), as denoted by the arrows. This finding is termed extravasation and is specific for aneurysm rupture. In (C), the massively enlarged aorta is again visualized, with the extravasated contrast seen tracking inferiorly. Adapted from (90). 42

Figure 8 Schematic demonstrating open aneurysm repair of an abdominal aortic aneurysm (AAA). On the left, an infrarenal AAA is visualized. On the right, major steps in aneurysm repair are visualized. The aorta and the common iliac arteries can be seen cross-clamped. The aneurysm has been incised and a graft is being sewn in place at the level of the proximal and distal aneurysm. After the graft is sewn into place, the aorta is sewn over to cover the graft. Adapted from (109). 46

Figure 9 Endovascular aneurysm repair (EVAR) stent. This is a unibody model (AFX; Endologix). Other stents may have a separate, modular component for one of the iliac limbs. Adapted from (110). 47

Figure 10 Intraprocedural angiograms demonstrating endovascular aneurysm repair (EVAR) stent deployment. (A) The common femoral artery (CFA) has been punctured, catheterized and opacified with contrast material. CFA catheterization enables access to the abdominal aorta. (B) The deployment catheter (containing the EVAR stent, which is labelled Main Body) is visualized just inferiorly to the renal arteries. RA; renal artery. Rt: right; Lt: left. (C) The main body of the stent has been deployed. Of note, there is a long limb that extends to the ipsilateral side of the common iliac puncture. There remains a short limb that must be catheterized from the contralateral side. (D) The short limb is catheterized via a contralateral approach through the left CFA. (E) The deployment device for the short limb is passed into the gate for the short limb. Deployment is not shown. (F) Completion angiogram demonstrating opacification of the stent. Adapted from (82). 48

Figure 11 Simplified schematic of a computed tomography (CT) imaging system. The X-ray tube produces X-rays. The filter and collimator alter the beam-shape to optimize patient coverage. The X-ray detectors are located opposite to the X-ray tubes and detect incident X-rays that have not been attenuated by the patient.

The gantry, which actually contains several X-ray tubes and detectors, rotates during acquisition while the motorize table moves the patient through the scan field. Adapted from (125). 52
Figure 12 Type Ia endoleak. (A) and (B) Computed tomography (CT) angiograms post-EVAR demonstrating contrast opacification of the aneurysm sac originating from the region of the proximal attachment site (white arrowheads). (C) Angiography confirms the presence of a type I endoleak (black arrowheads). Adapted from (118).....53
Figure 13 Select illustrated principles of magnetic resonance imaging (MRI). (A) Every proton in the human body has an axis of nuclear magnetization termed a spin (dotted arrow). (B) When a homogenous magnetic field (B_0) is applied to a tissue, its protons will align themselves either parallel or antiparallel to the magnetic field and then precess (rotate) at the Larmor frequency. More protons will align their axes of nuclear magnetization parallel to B_0, so the net magnetization of the protons (M_z) will be in the direction of B_0. (C) The M_z is again shown in the direction of B_0. Adapted from (128). 56
Figure 14 Magnetic resonance images of a type II endoleak. (A) Computed tomography (CT) of an abdominal aortic aneurysm status post endovascular aneurysm repair (EVAR) and surgical clipping of paired lumbar arteries (arrows). As per the authors, the endoleak was occult. (B) T1 post-contrast axial image of the corresponding aneurysm demonstrates hyperintense contrast extending from the region of the clips (arrow) into the aneurysm sac, suggestive of a type II endoleak. Adapted from (108). 56
Figure 15 Ultrasound transducers use piezoelectric crystals to high frequency pressure waves with alternating regions of high pressure and low pressure. Adapted from (133).....58
Figure 16 Schematic of brightness mode (B-mode) ultrasound (US) imaging of the kidney. High-frequency sound waves are emitted by the ultrasound probe, which are returned back to the ultrasound probe due to reflection and scattering induced by the underlying tissue. The mechanical energy of the returning sound wave is converted into an electrical signal, which is used to produce brightness values on a coordinate system defined by the x-axis and y-axis. Adapted from (135). 59
Figure 17 Duplex ultrasound examination demonstrating foci of Doppler signal outside of the stent but inside the aneurysm sac (arrows) in keeping with endoleaks. Adapted from (137). 60
Figure 18 Transarterial coil embolization of a type II endoleak. (A) A type II endoleak fed by a lumbar artery is identified on contrast enhanced computed tomography (CT); the arrow points to the feeding vessel. (B) Selective angiogram of the right internal iliac artery demonstrates that the lumbar vessel (arrows) is fed by the right iliolumbar artery. (C) A microcatheter is advanced to the endoleak. (D) The endoleak nidus and feeding artery have been coiled. There is no opacification of the endoleak upon contrast administration. Adapted from (36). 63
Figure 19 Stress, strain, and elastic moduli. Elastic moduli are material properties that relate an applied stress to the strain that the material undergoes. The first column of shapes describes Young's modulus.

When a normal force per area (stress, σ_n) is applied to an object, there is a resultant relative change in its dimension along the vector of the force called the strain (ε_n). Young's modulus (E) is the ratio of the normal stress to the normal strain. The second column of shapes describes the shear modulus. When a tangential force per unit area (shear stress, σ_s) is applied to the surface of a material, the material undergoes an angular change in configuration, called the shear strain (ε_s). The shear modulus (G) is the ratio of the shear stress to the shear strain. F_n = normal force; F_s = shear force; A = area (normal stress: area perpendicular to the force vector; shear stress: area parallel to the force vector); l = length; θ = angle describing the shear; Δt = linear displacement surface of object surface parallel to shear force. Adapted from (180). 68

Figure 20 Schematic outlining the steps of elastographic imaging. A stimulus is applied to the tissue of interest. Imaging techniques are used to detect a response in the tissue. The measured pre- and post-excitation tissue changes are used to infer the mechanical properties of the tissue. These mechanical properties can then be used for clinical characterization and diagnosis. Adapted from (184). 69

Figure 21 Different types of ultrasound elastography with their commercial counterparts. Ultrasound elastography can be divided into two major categories: strain imaging and shear wave imaging. In strain imaging, a force parallel to the transducer is used to generate tissue deformation, which is subsequently measured. Strain elastography (a subtype of stain imaging) relies on the use of an external or internal compressive force to generate deformation. Acoustic radiation force impulse (ARFI) strain imaging, in contrast, uses an acoustic pushing pulse to displace the tissue. In shear wave imaging, shear waves are generated to calculate tissue elasticity. 1D transient elastography uses a mechanical vibrating device to create shear waves that travel parallel to the incident wave. In contrast, both point shear wave elastography and 2D shear wave elastography techniques use ARFIs to generate shear waves which travel perpendicularly to the transducer. In point shear wave elastography, one focal point is interrogated to calculate Young's modulus. In 2D shear wave imaging, ARFIs are directed in multiple focal zones, which generate multiple perpendicularly travelling shear waves. This allow for real time quantitative elastographic analysis during imaging. Harmonic elastography is not included in the present figure but will be described subsequently. Adapted from (180). 70

Figure 22 One form of strain elastography calculates the displacement of radiofrequency signals pre- and post-compression to estimate the mechanical properties of the imaged structure. Δl = change in length; RF = radiofrequency. Adapted from (180). 72

Figure 23 Schematic of strain imaging. On the left, a normal mechanical force is applied to a homogenous, compressible tissue. This causes a uniform displacement over the imaged depth and, consequently, strain analysis reveals a uniform strain. On the right, a stiff region is incorporated into tissue. When a similar normal mechanical force is applied, there is no displacement along the length of the stiff area, while the

remainder of the tissue deforms as in the schematic on the left. Strain analysis reveals a lower strain in this region. This can be used as an additional feature to characterize imaged tissue. Adapted from (166). 73
Figure 24 Shear wave imaging relies on the generation of shear waves. In shear waves, the particle motion is perpendicular to the direction of travel of the wave. The shear wave speed can be calculated to give an estimate of the shear modulus, which can be converted the elastic modulus via Poisson's ratio. c_s = wave speed; G = shear modulus; ρ = tissue density. Adapted from (180). 75
Figure 25 Bilateral iliac aneurysm model for testing of embolic agents. (A) Contrast-enhanced fluoroscopic image demonstrating the surgically created bilateral iliac artery aneurysm model. The arrows point to the implanted outflow tracts. (B) Schematic of the same model status post bilateral endovascular aneurysm repair and creation of type Ia endoleaks. Figures adapted from/with reference to (40, 43, 170, 171). 82
Figure 26 Procedural and imaging follow-up timeline. Surgical aneurysm creation was undertaken eight weeks prior to EVAR and endoleak creation. Embolization was performed on the same day as EVAR. (A) Six of the subjects were followed with imaging for three months after EVAR before sacrifice and histopathological analysis. Ultrasound-based acquisitions were obtained at all follow-up times (one week, one month, and three months); CT images were obtained at sacrifice. (B) Three of the subjects were followed with imaging for six months after EVAR before sacrifice and histopathological analysis. US-based acquisitions were obtained at all follow-up times (one week, one month, three months, and six months); CT was performed at three and six months. For both groups, all ultrasound-based acquisitions were obtained of the proximal, middle, and distal aneurysm sac. The aneurysm sac region of interest was segmented at all follow-up time points; the thrombus and embolic agent were only segmented at sacrifice. B-Mode: brightness mode ultrasound; CT: Computed tomography; DUS: Duplex ultrasound; Elasto: ultrasound cine loops for strain elastography; EVAR: endovascular aneurysm repair; FU: follow-up. 85
Figure 27 Multimodal image co-registration and segmentation at sacrifice of the mid-level aneurysm sac region of interest (segmented in green) for an endoleak three months post-embolization with the chitosan hydrogel embolic agent. The arrows indicate the stent-graft. (A) Selected B-mode image of the mid level of the aneurysm demonstrates the segmentation of the entire aneurysm sac. Note that the stent-graft was excluded. (B) Corresponding duplex ultrasound image suspected to have been taken at a slightly more caudal location, where an endoleak is visualized. Note that it has been excluded from the segmentation. (C) Contrast-enhanced CT examination of the aneurysm sac at the same level of (A) and the other remaining images. Note that an endoleak was not identified at this level, but was identified a few slices lower, suggesting that the image in (B) was more caudal. (D) and (E) Macroscopic cut and histopathological slide of the mid-level of the aneurysm; note that no endoleak is visible on these levels; an endoleak was confirmed more inferiorly (not shown). (F) Selected segmented B-mode image from the obtained cine loop used to produce the elastograms. Part of the aneurysm sac was not included because there was potentially an

endoleak in this region; this was done to avoid the high strains associated with signal decorrelation. The segmentation mask was propagated through the remainder of the cine loop using a semiautomatic technique. Appropriate segmentation requires the integration of all of the imaging modalities. 88
Figure 28 Multimodal image co-registration, segmentation, and post-processing of the embolic agent region of interest (segmented in green) for an endoleak three months post-embolization with the chitosan hydrogel embolic agent (CH) at sacrifice. (A) B-mode image of the mid level of the aneurysm demonstrates the segmentation of the embolic agent, which is slightly hyperechoic and heterogenous. (B) Duplex ultrasound image. Note that the endoleak has been excluded. (C) Contrast-enhanced CT examination. Note that the embolic agent and thrombus cannot be differentiated (the former's radiopacity is lost after 48 hours). (D) Macroscopic cut demonstrating the embolic agent. (E) Selected segmented B-mode image from the cine loop used to produce the elastogram. The segmentation mask was propagated through the remainder of the cine loop using a semiautomatic technique. (F) Instantaneous axial deformation elastogram of the embolic agent superimposed over a cine frame during systole. (G) Instantaneous axial deformation curve; the maximum axial deformation parameter (average of all peaks) is labelled. (H) Raw cumulative axial deformation curve. (I) Cycle-adjusted cumulative axial deformation curve adjusted for the cardiac cycle (thicker curve; the thinner curve is the axial deformation curve). The range cumulative axial deformation parameter is labelled. Some of these images have been included in (31, 43). 90
Figure 29 Multimodal image co-registration, segmentation, and post-processing of the agent region of interest (segmented in green) for an aneurysm three months after embolization with the chitosan hydrogel with sodium tetradecyl sulphate embolic agent (CH-STS) at sacrifice. The arrows indicate the stent-graft. All images were taken at approximately the same level but were subject to operator variability. The region indicated by (*) did not have a correlate on the cine loop and was therefore not included in the final segmentation. (A) B-mode image of the mid level of the aneurysm. The embolic agent is slightly hyperechoic and heterogenous. (B) Corresponding segmented duplex ultrasound image demonstrating an endoleak. (C) Corresponding contrast-enhanced CT confirming an endoleak. (D) Corresponding macroscopic cut demonstrating the agent and the endoleak. (E) Selected segmented B-mode image from the cine loop used to produce the elastograms. This image was likely obtained at a slightly different level compared to (A) and (D), resulting in a slightly different-appearing segmentation mask. It was important to exclude the endoleak and intraluminal thrombus to have a homogenous region of interest. (F) Instantaneous axial deformation elastogram of CH-STS superimposed over a cine frame during systole. (G) Instantaneous axial deformation curve. The maximum axial deformation parameter is labelled. (H) Raw cumulative axial deformation curve. (I) Cycle-adjusted cumulative axial deformation curve (thicker curve; the thinner curve is the axial deformation curve). The range cumulative axial deformation parameter is labelled.....91

Figure 30 Multimodal image co-registration, segmentation, and post-processing of the thrombus region of interest (segmented in green) for an aneurysm three months post-embolization with the chitosan hydrogel with sodium tetradecyl sulphate embolic agent (CH-STS) at sacrifice. The arrows indicate the stent-graft. All images were taken at approximately the same level but were subject to operator variability. (A) B-mode image of the mid level of the aneurysm. The hyperechoic region corresponds to CH-STS and the hypoechoic regions correspond to thrombus. (B) Corresponding duplex ultrasound. (C) Corresponding contrast-enhanced CT image. (D) Corresponding macroscopic cut. (E) Selected segmented B-mode image from the cine loop used to produce the elastograms. (F) Cumulative axial deformation elastogram of the thrombus superimposed over a cine frame during systole. (G) Instantaneous axial deformation curve; the maximum axial deformation parameter is labelled. (H) Raw cumulative axial deformation curve. (I) The cycle-adjusted cumulative axial deformation curve (thicker curve; the thinner curve is the axial deformation curve). The range cumulative axial deformation parameter is labelled. Of note, only complete cardiac cycles without motion artifact (seen on the cine) were included in the post-processing.....92
Figure 31 Multimodal image co-registration, segmentation, and post-processing of the aneurysm sac region of interest (segmented in green) for an aneurysm six months after successful embolization with the chitosan hydrogel embolic agent with sodium tetradecyl sulphate (CH-STS) at sacrifice. The arrows indicate the stent graft. (A) B-mode image of the distal level of the aneurysm demonstrates the segmentation of the sac. (B) Corresponding duplex ultrasound image; there is no endoleak to be excluded. (C) Corresponding contrast-enhanced CT image confirming the absence of endoleak. (D) Corresponding macroscopic cut. (E) Selected segmented B-mode image from the cine loop used to produce the elastograms. (F) Cumulative axial deformation elastogram of the sac superimposed over a cine frame during systole. (G) Instantaneous axial deformation curve; the maximum axial deformation parameter (average of all peaks) is labelled. (H) The cycle-adjusted cumulative axial deformation curve (thicker curve; the thinner curve is the axial deformation curve). The range cumulative axial deformation parameter is labelled. Note that frames containing motion artifact (seen on the cine loops) were excluded from the analysis. 93
Figure 32 Breakdown of the elastograms generated using the segmentations independently performed by each reader. The elastograms contain the data used to derive the maximum axial deformation, range cumulative axial deformation, and the range cumulative axial shear. (A) Elastograms generated of the aneurysm sac ROI. (B) Elastograms generated of the embolic agent ROI. *One subject embolized with CH-STS did not have any residual embolic agent, thus this ROI could not be segmented for the subject. (C) Elastograms generated of the ILT ROI. CH: Chitosan hydrogel; CH-STS: Chitosan hydrogel with sodium tetradecyl sulphate; FU: follow-up; ILT: intraluminal thrombus; ROI: region of interest; t: time. 98

Acronyms and Abbreviations

AAA	Abdominal aortic aneurysm
A-mode	Amplitude mode
ARFI	Acoustic radiation force impulse
BGP	β-glycerophosphate
B-mode	Brightness mode
CH	Chitosan hydrogel embolic agent
CH-STS	Chitosan hydrogel with sodium tetradecyl sulphate embolic agent
CI	Confidence interval
CT	Computed tomography
DAM	Déformation axiale maximale
DMSO	Dimethyl sulfoxide
DUS	Duplex ultrasound
EVAR	Endovascular aneurysm repair
EVOH	ethylene vinyl alcohol copolymer
HU	Hounsfield units
ICC	Intraclass correlation coefficient
ILT	Intraluminal thrombus
LSME	Lagrangian speckle model estimator
MAD	Maximum axial deformation
M-Mode	Motion mode
MMP	Matrix metalloproteinase
MRI	Magnetic resonance imaging
NIVE	Noninvasive vascular elastography
OAR	Open aneurysm repair
QSUE	Quasi-static ultrasound elastography
RCAD	Range cumulative axial deformation
RCAS	Range cumulative axial shear
RF	Radiofrequency
ROI	Region of interest
STS	Sodium tetradecyl sulphate
SUE	Strain ultrasound elastography
SWE	Shear wave elastography

SWI	Shear wave imaging
US	Ultrasound

Acknowledgments

Thank you sincerely to the members of the jury for agreeing to review my mémoire. I truly appreciate your willingness to dedicate your time and expertise to help me progress to the next stage of my career.

I would like to express my immense gratitude to Dr. Soulez for his never-ending guidance and mentorship. The confidence that he showed in me allowed me to develop that same confidence in myself. I would like to thank Dr. Lerouge for co-supervising my project and for trusting me to contribute to her research vision. I would like to thank Dr. Cloutier for allowing me to conduct my research using his laboratory's resources and innovations. I would like to thank Fatemeh Zehtabi and Marie-Hélène Roy Cardinal for contributing their expertise to help make this project a reality. I would like to thank Sahir Bhatnagar for his contribution to the statistical analysis. I would like to thank Michel Gouin and Hélène Héon for their role in the animal studies. I would like to thank Igor Salazkin, Antony Bertrand-Grenier, and Husain Alturkistani for their contributions to this work. I would like to thank all of the current and past members of the Laboratoire clinique du traitement de l'image, the Laboratoire de biomatériaux endovasculaires, and the Laboratoire de biorhéologie et d'ultrasonographie médicale for their cumulative contributions to this project. I would like to thank the Centre de recherche du Centre hospitalier de l'Université de Montréal, the Université de Montréal, and the Fonds de recherche en santé du Québec for supporting my research. I would like to thank the McGill Radiology Department and the McGill Radiology Research Committee for allowing me to pursue this project during my residency.

On a personal level, I would like to thank all of the people who encouraged me throughout the pursuit of my master's degree. Thank you to my friends for keeping me grounded. Thank you to Yanick for providing me with constant companionship at the research center. Thank you to Samuel RQ for motivating me to excel in my courses. Thank you to Jovi for keeping me company during our innumerable virtual writing sessions. Finally, thank you to my brothers, my extended family, and my parents for your never-ending support.

Part I - Introduction

Chapter 1 – Summary

Abdominal aortic aneurysm (AAAs) are defined as pathological dilatations of the abdominal aorta measuring > 3.0 cm (1). They are most prevalent in elderly Caucasian men with a history of smoking (2-4). The most feared complication of AAAs is rupture, which carries a high mortality (5, 6). AAAs were traditionally repaired with open aneurysm repair (OAR), an invasive surgery associated with a high incidence of post-operative complications (7-10). More recently, endovascular aneurysm repair (EVAR) has emerged as a minimally invasive alternative to OAR. In EVAR, an intravascular stent is percutaneously inserted into the abdominal aorta to bypass the diseased segment (11, 12). EVAR is associated with superior periprocedural outcomes and has become the preferred therapeutic modality for the treatment AAAs (6, 8, 9, 13, 14). However, EVAR is limited by the development of endoleaks—defined as persistent perfusion of the aneurysm sac around the stent—as well as other complications (15). There are five different types of endoleaks, which are described in further detail in **Figure 1**. Endoleaks may be associated with aneurysm growth, increased intervention, and potential rupture. Therefore, all patients post-EVAR require regular follow-up imaging (1, 16).

Ultrasound (US), computed tomography (CT), and magnetic resonance imaging (MRI) have all been described as non-invasive modalities for the surveillance of post-EVAR complications. However, each is associated with unique limitations. US with Doppler imaging (also called Duplex ultrasound (DUS)) is the least expensive and most widely available modality, but it is operator dependent and is the least sensitive (17, 18). Contrast-enhanced CT is the reference standard, but it is expensive, exposes patients to ionizing radiation, and may be associated with contrast reactions or contrast-induced nephropathy (1, 19, 20). MRI has the greatest sensitivity for endoleaks (21), but it is limited by high cost, low availability, and long acquisition times.

Strain ultrasound elastography (SUE) has emerged as a potential imaging adjunct for AAAs post-EVAR. SUE calculates tissue elasticity based on changes in US signal after the application of a force, such as from the pulsations of the cardiovascular system (22-24). Elasticity is of particular interest in the follow-up of AAA patients as thrombus immaturity is linked with aneurysm expansion pre-EVAR (25) and with aneurysm non-shrinkage post-EVAR (26). Stiffer intraluminal contents also tend to better decrease aneurysm wall stress (27). Therefore, the detection of immature sac contents may be useful in guiding management. SUE has previously been shown to be able to detect endoleaks and differentiate organized and fresh thrombus (28, 29). Other forms of elastography (such as shear wave imaging/elastography (SWI/SWE)) have been used to characterize aneurysm sac contents and endoleaks; however, these forms of elastography suffer from poor penetration and utilize algorithms that rely on potentially inappropriate assumptions about the underlying tissue composition (30-33).

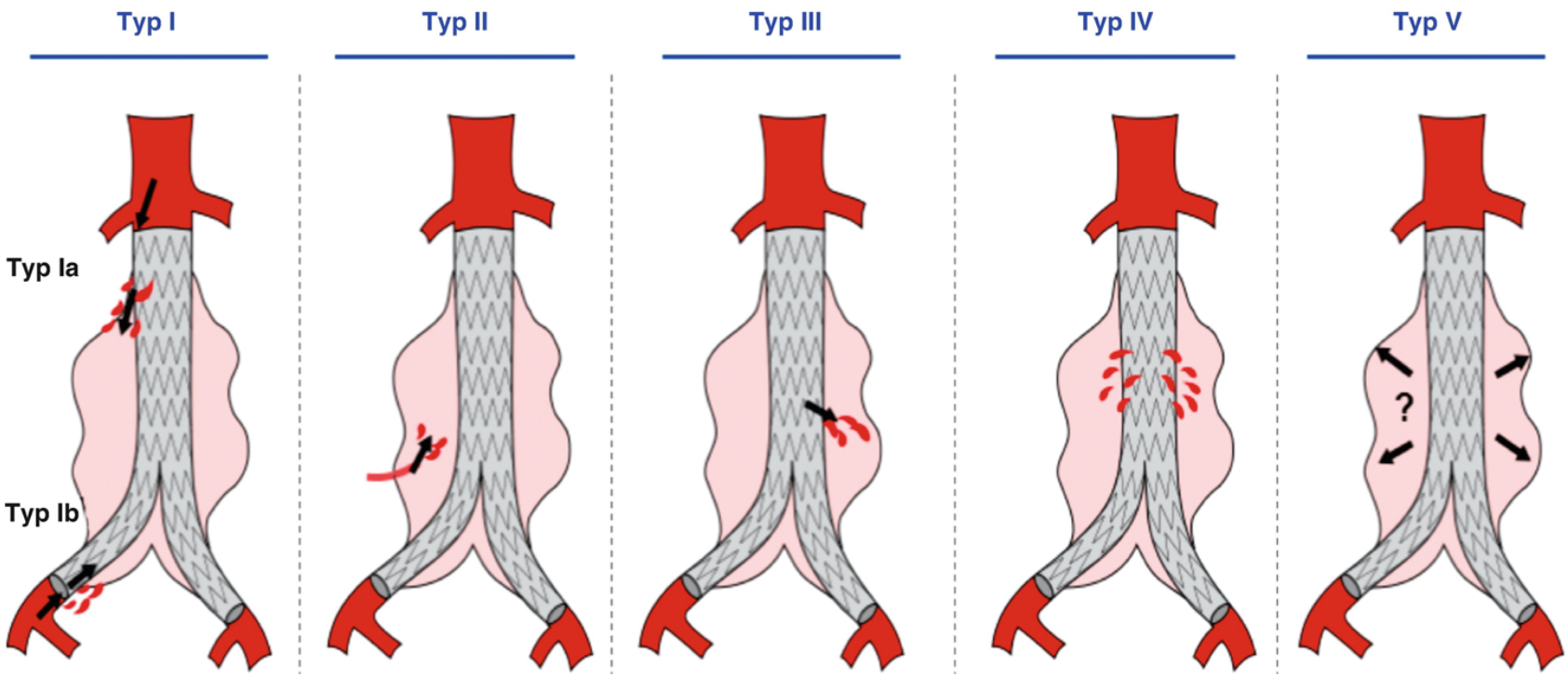

Figure 1 Schematic representation of the different types of endoleaks. Type I endoleaks are caused by blood flow into the aneurysm sac along the proximal or distal attachment sites of the EVAR stent, termed type Ia and type Ib endoleaks, respectively. Type II endoleaks are caused by collateral, retrograde flow into the aneurysm sac from a vessel that once was supplied by the aneurysm sac, such as the inferior mesenteric artery. Type III endoleaks are due to graft tears or component separation of the EVAR stent. Type IV endoleaks are caused by the transient passage of blood through pores in the stent graft during deployment on angiography. Type V endoleaks, also termed endotension, entail enlargement of the sac without blood flow visualized into the sac on imaging. Adapted from (101). EVAR: Endovascular aneurysm repair.

Once an endoleak is detected, therapy is directed at its type. Type II endoleaks—caused by retrograde blood flow into the aneurysm sac through collateral vessels (34)—are the most common and are typically treated via embolization when associated with aneurysm growth (1). There are several embolic agents that are available—including Onyx, coils, cyanoacrylate glue, and thrombin—however, they each suffer from disadvantages, including price, interference with follow-up imaging, technical difficulty during deployment, and efficacy (35-38). Furthermore, type II endoleaks are often refractory to treatment, with a long-term success of only approximately 40% across therapies (35). Endoleak persistence post-embolization is thought to be due to poor occlusivity of the embolic agent and the presence/persistence of endothelial cells lining the endoleaks (39, 40).

In this context, an embolization agent containing a biocompatible, radiopaque chitosan hydrogel mixed with the sclerosant sodium tetradecyl sulphate (STS), named CH-STS, was developed. CH-STS has demonstrated favorable in vitro mechanical properties and is associated with lower endoleak persistence post-embolization compared to a non-sclerosing chitosan hydrogel embolic agent (CH) (41-43). However, its behavior in vivo and its and impact on the mechanical properties of the associated intraluminal thrombus (ILT) and the overall aneurysm sac—in comparison to CH—merit further characterization using a robust and penetrating elastographic technique, such as SUE.

The goal of the present mémoire is to characterize the constituents of endoleaks embolized with chitosan-based embolic agents (both with and without STS) using SUE.

In the first section of the mémoire (**Part I**), a background literature review is provided, comprising **Chapters 1** to **5**. In **Chapter 1** (the present chapter), the reader is oriented to the contents of the mémoire. In **Chapter 2**, the circulatory system, the aorta, and the pertinent epidemiological, pathophysiological, and clinical details regarding AAAs are introduced. In **Chapter 3**, the treatment modalities available for AAAs are summarized, with particular emphasis on EVAR. In **Chapter 4,** endoleaks are re-introduced, the major imaging modalities that are used for their detection are described, and the most common options available endoleak for therapy are outlined (with particular emphasis on type II endoleaks). To conclude the chapter, the embolic agent CH-STS is introduced. In **Chapter 5**, elastography is described, with particular reference to SUE. The potential role of SUE to characterize AAA mechanical properties as well as to differentiate the mechanical properties of embolic agents is emphasized to set the stage for its use as the foundational imaging modality for this study. **Part II** is the experimental section of the mémoire. In **Chapter 6,** the specific objectives and hypotheses of the project are detailed. In **Chapter** 7, the methodology of the study is described. In **Chapter 8**, the results of the study are presented. Finally, in **Chapter 9,** the results of the study are interpreted with reference to the literature, the limitations of the study are described, and the future implications of the study are proposed.

Chapter 2 – Abdominal Aortic Aneurysms

2.1 The Aorta

2.1.1 Anatomy and Physiology of the Circulatory System

The cardiovascular (circulatory) system is a complex distribution system responsible for the delivery of essential substances throughout the body as well as for the removal of waste. The center of this system is the heart, which is a muscular pump that transmits blood in a unidirectional fashion throughout the cardiovascular system through two interlinked circuits called the pulmonary and systemic circulations (see **Figure 2**). Each circulation has its own arterial, capillary, and venous network. Blood enters the arterial system first, which is composed of arteries. Arteries are thick-walled vessels with varying amounts of smooth muscle cells, elastin, and collagen that distribute blood to end organs. Arteries divide in number exponentially as they course distally. This not only enables blood to be directed to different parts of the body but also increases the system's overall hypothetical cross-sectional area, resulting in slower blood flow velocities for eventual nutrient exchange (44). The most distal arteries are called arterioles. Arterioles are the entry points of the microcirculation. The microcirculation is the functional site of exchange between the circulatory system and the surrounding tissues and comprises vessels measuring less than 20 μm (45). Arterioles eventually divide into capillaries, which are tiny, thin-walled vessels through which blood cells may travel in single file. Capillaries are the site where nutrient, waste, and gas exchange occur with the surrounding tissues. Capillaries then drain into venules, which are the exit point of the microcirculation and the entrance into the venous system. Veins then combine as they course closer to the heart, eventually draining into one of the atria of the heart (46).

There are important differences between the pulmonary and systemic circulations. Blood in the pulmonary system is pumped by the right heart, beginning in the right atrium and then passing to the right ventricle, the pulmonary arteries, the pulmonary capillaries, the pulmonary veins, and then finally returning to the left heart. The major functions of this circuit the collection of O_2 and the offloading of CO_2 within the lungs. Once blood returns to the left side of the heart—passing through the left atrium and the left ventricle—it is pumped through the systemic circulation. The systemic circulation is responsible for the delivery of oxygen, nutrients, hormones, and other substances to the tissues throughout the body. Similar to the pulmonary system, the exchange of these substances occurs at the level of the capillary. Systemic venous blood drains into the right atrium of the heart via the superior vena cava (which drains the head, thorax, and upper extremities) and the inferior vena cava (which drains the abdomen/pelvis and lower extremities). See **Figure 2** for further details and exceptions (46).

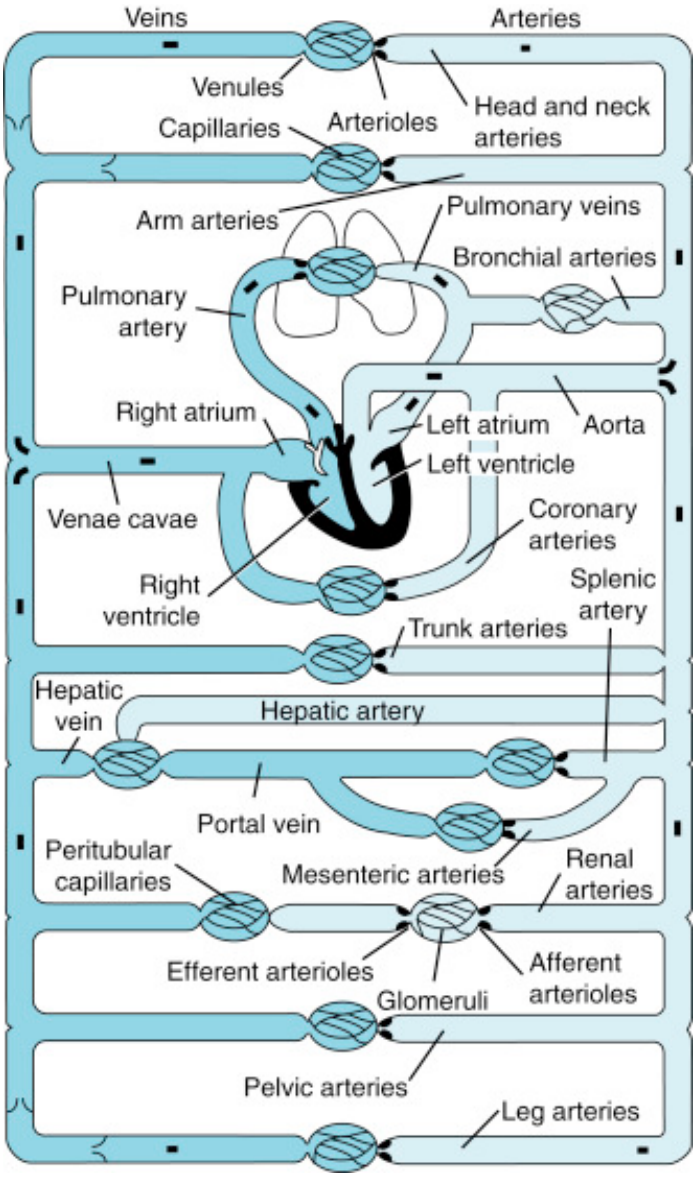

Figure 2 Schematic of the circulatory system. The pulmonary circulation and the systemic circulation are organized in series with the heart, which acts as a central pump. Within the systemic circulation, there are several parallel circuits supplying different organ systems. In general, blood is distributed by the arterial system to the peripheral tissues, where—at the level of the capillary—gas, nutrient, and waste exchange occurs. Blood is then returned to the heart via the venous system. There are several exceptions to this rule—such as in the digestive and the renal systems, where there is more than one capillary network and complex arterial inputs—but this is beyond the scope of the present document. Adapted from (46).

2.1.2 Anatomy of the Aorta

The aorta is the largest artery in the human body, spanning both the thoracic and abdominal cavities. It transmits blood from the left heart and is the first vessel of the systemic circulation. Within the chest, the aorta is defined by three anatomic regions: the ascending aorta, the aortic arch, and the descending aorta. The ascending aorta originates at the level of the aortic valve and it is covered by fibrous pericardium that extends from the heart. At its base, the ascending aorta gives off the left and right coronary arteries, which perfuse the heart. The ascending aorta then courses antero-superiorly and slightly towards the right in a vertical-oblique fashion to the level of the second costal cartilage. At this level, the aorta becomes the aortic arch, where it takes a predominantly horizontal, curved orientation, coursing posterolaterally towards the left. The arch gives off three major branches that perfuse the upper extremities and head: the brachiocephalic artery (which gives off the right common carotid and right subclavian arteries), the left common carotid artery, and the left subclavian artery. Distal to the left subclavian artery, the aorta again takes a more vertical, inferiorly-directed course as it becomes the descending aorta (47). The descending aorta courses slightly to the left of the anterior aspect of the vertebral column and gives the intercostal arteries, the bronchial arteries, as well as branches to the esophagus, the mediastinum and pericardium, and the thoracic wall (48, 49).

The abdominal aorta courses through the abdomen and is responsible for supplying blood to the abdominopelvic cavity as well as the lower extremity (see **Figure 3**). Its superior margin is defined by the aortic hiatus of the diaphragm, which occurs at the level of the 12th thoracic vertebra (T12), and its inferior margin is defined by its bifurcation into the left and right common iliac arteries at approximately the level of the 4th lumbar vertebra (L4) (48, 50). The normal diameter of the aorta is reported to be between 1.5-2.5 cm (51). There are several arteries that arise from the abdominal aorta that supply the abdominal viscera and parts of the abdominal wall; notable branches are detailed in **Table 1**.

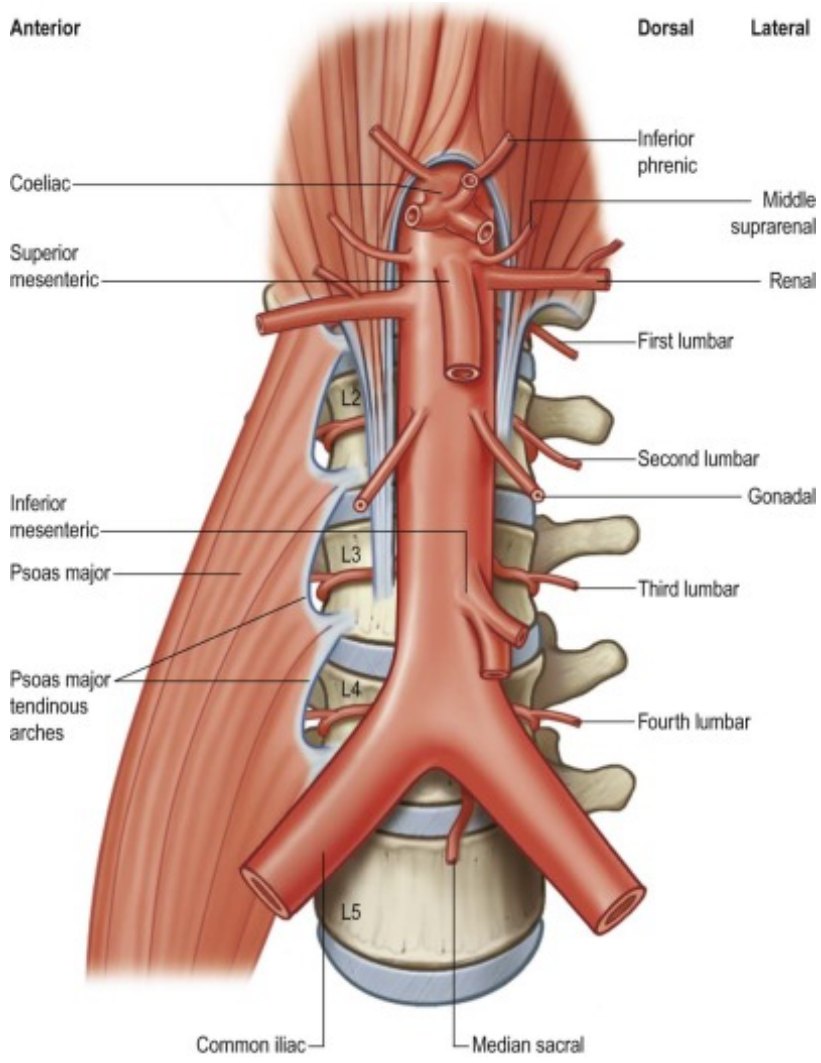

Figure 3 Illustration of the abdominal aorta with several its branches. The abdominal aorta originates at the aortic hiatus (at the level of the 12th thoracic vertebra) and terminates at the bifurcation of the common iliac vessels at (at the level of the 4th lumbar vertebra). Branches arise from the anterior, lateral, and posterolateral aspects of the abdominal aorta. Adapted from (48).

Branch of the aorta	Location	End organ
Celiac artery	Anterior aorta, T12-L1	Liver, gallbladder, spleen, stomach, pancreas, duodenum
Superior mesenteric artery	Anterior aorta, L1	Pancreas, duodenum, jejunum, ileum, colon (cecum, ascending colon, transverse colon until the splenic flexure), appendix
Inferior mesenteric artery	Anterior aorta, L3	Colon distal to the splenic flexure (distal transverse colon and descending colon), superior rectum
Paired inferior phrenic artery	Posterolateral, superior aorta (just inferior to the hiatus)	Diaphragm, adrenal gland
Paired middle suprarenal arteries	Posterolateral, superior abdominal aorta, slightly inferior to the inferior phrenic arteries, at the level of the superior mesenteric artery	Adrenal glands. Note that the paired superior suprarenal arteries and the paired inferior suprarenal arteries also perfuse the adrenal glands and arise from the inferior phrenic arteries and renal arteries, respectively.
Lumbar arteries	Posterolateral aorta, along vertebral segments (L1-L4)	Lumbar spinal cord and ganglia, lumbar vertebrae (osseous and soft tissue components), posterior abdominal wall
Renal arteries	Either side of the aorta, just below the takeoff of the superior mesenteric artery, approximately L1	Kidneys, ureters, adrenal glands
Gonadal arteries	Slightly inferior to renal arteries bilaterally	Testicles or ovaries
Median sacral artery	Midline, posterior, just above the common iliac bifurcation, L4-L5	L4-L5, sacrum, coccyx

Table 1 Origins of notable branches of the abdominal aorta and examples of end organs that they perfuse. The table was generated using descriptions from (48, 50). T: thoracic vertebra; L: lumbar vertebra.

2.1.3 Histology of the Aorta

Arteries comprise three layers: the tunica intima, tunica media, and tunica adventitia (see **Figure 4**). The tunica intima is the thinnest, most internal layer and is composed of a single layer of endothelial cells resting on top of a basal lamina and subendothelial connective tissue. The tunica media is the thickest layer and contains elastin, collagen, and smooth muscle cells. Finally, the tunica adventitia is the outer support layer that contains connective tissue—including elastin and collagen—as well vessels and nerves— termed the vaso vasorum and nervi vasorum, respectively (44). The adventitial layer is critical for resisting vessel expansion (52).

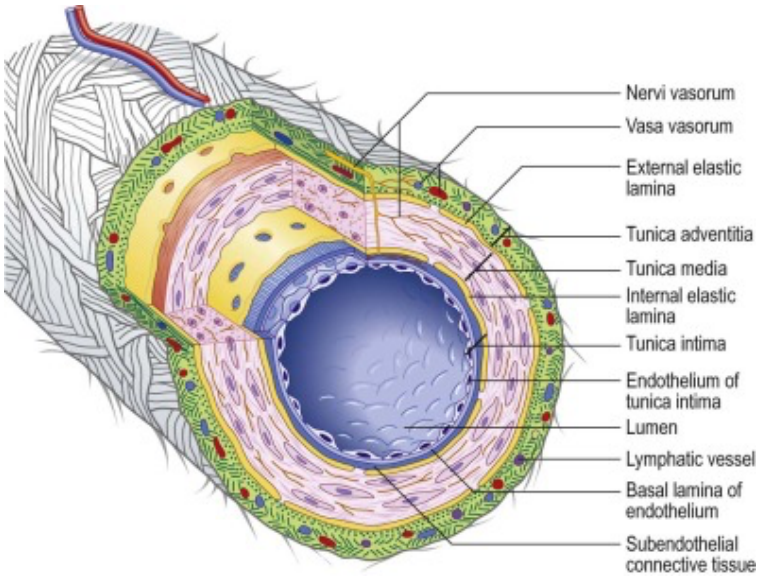

Figure 4 Illustration demonstrating the various layers of a representative artery, including the tunica intima, tunica media, and tunica adventitia. Adapted from (44).

The aorta is termed an elastic artery because of its high content of elastin (44). Elastin is a biopolymer that is responsible for resilience and elastic recoil within several tissues of the body (53). The aorta has a well-developed internal elastic lamina—found between the intima and the media—that is rich in elastin (44). The media also contains several layers of elastin (elastic lamellae), which alternate with layers of smooth muscles cells. The high proportion of elastin within this layer allows for the kinetic energy transmitted from the heart during systole to be stored as potentially energy, which is then released as kinetic energy during diastole. This allows for continuous blood flow throughout the arterial system during the cardiac cycle (54). Finally, the adventitia of the aorta is also particularly well developed and—in addition to elastin, collagen, nerves, and vessels—it contains fibroblasts, macrophages, mast cells, and lymphatic

vessels. There is an external elastic lamina between the media and adventitia as well, however, it is less distinctive when compared to more distal arteries (44). Please see **Figure 5** for further details.

The more distal arteries will be discussed briefly. Beyond the elastic arteries are found the muscular arteries and the arterioles. The muscular arteries have a much greater contribution of smooth muscle cells to the media (about 75% by mass). Furthermore, the overall proportion of elastin within the walls of the muscular arteries is less (although their external elastic lamina is more prominent). Arterioles are found distally to the muscular arteries and are the entry point into the microcirculation, as previously described. Their internal elastic lamina is either highly porous or absent. The smooth muscles cells of the arteriolar wall are tightly wound, which—in addition to the extensive connections with the autonomic nervous system—allows for strict regulation of blood flow into the capillary network (44).

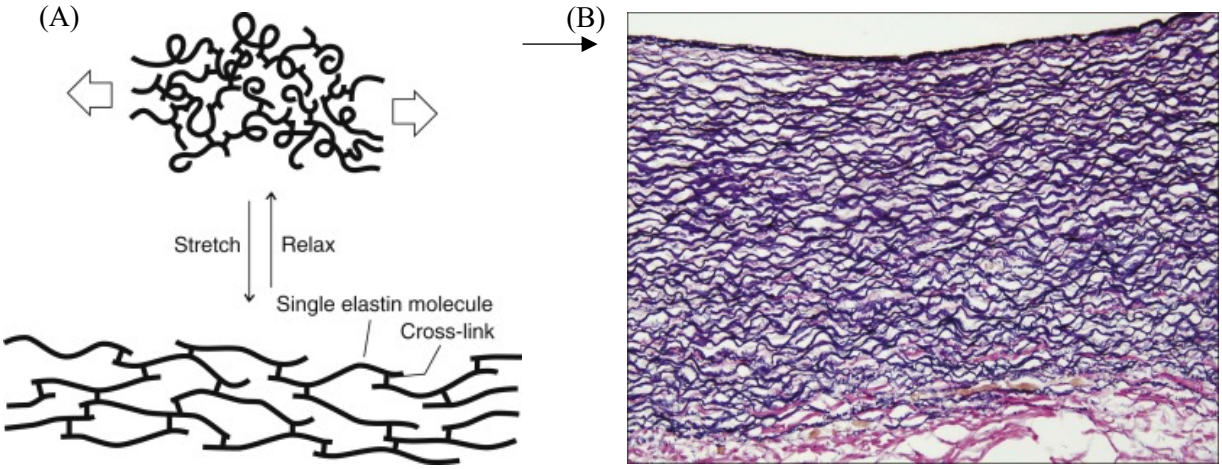

Figure 5 The aorta is considered an elastic artery given its high content of elastin fibers. (A) Schematic of elastin in its relaxed and stretched states. The tendency for elastin to return to its relaxed state allows for recoil of the aorta during the cardiac cycle. Adapted from (55). (B) Histopathological slide of the human aorta that has been stained dark purple for elastic fibers. The aorta is rich in elastin, which provides resilience and elastic recoil. The superior aspect of the image is the vessel lumen and the inferior aspect of the image is the adventitia. Deep to the endoluminal surface, there is well-developed internal elastic lamina (arrow). Beneath this structure, the thick media contains several dark purple, undulating lines corresponding to layers of elastin fibers. Along the superficial aspect of the vessel, the elastic fibers can be seen blending with the adventitia. Adapted from (44).

2.2 Introduction to Abdominal Aortic Aneurysms

2.2.1 Definition

Abdominal aortic aneurysms (AAAs) are conventionally defined as aneurysmal dilatations of the infrarenal abdominal aorta measuring ≥ 3.0 cm (1). AAAs have also been defined as dilatations of the abdominal aorta measuring 1.5 times that of the normal vessel (56). The average diameter of the abdominal aorta is dependent on several factors, including age, body surface area, and sex, but is approximately 2.0 cm (57). In defining AAAs, the maximum aneurysmal dilatation is typically measured below the renal ostia (i.e. in the infrarenal region); however, the aneurysmal dilatation may extend superiorly to involve the renal ostia or the suprarenal abdominal aorta (see **Figure 6**). Morphologically, AAAs may be fusiform or saccular. Fusiform aneurysms entail circumferential dilatation of the aorta, whereas saccular aneurysms entail a more focal outpouching. AAAs in the conventional sense refer to true aneurysms that involve all three layers of the vessel (the intima, media, and adventitia) (58); these aneurysms will be the focus of the present mémoire.

Aneurysms of the abdominal aorta that do not involve all three layers of the wall are termed pseudoaneurysms and will be briefly described. Pseudoaneurysms typically appear as focal outpouchings within the wall (i.e. having a saccular morphology) and are generally provoked by trauma, infection, or chronic inflammation. They result when a focal injury in the vessel wall allows blood to dissect and expand the surrounding media or adventitia (59). Aortic pseudoaneurysm are classically identified in thoracic aorta after trauma at the level of the isthmus but may be found in the abdominal aorta as well. Pseudoaneurysms tend to have a small neck with a more dilated pouch (60, 61) and are considered abnormal even at diameters < 3.0 cm (62). The distinction of a pseudoaneurysm and from a true saccular aneurysm may be difficult with imaging alone and often requires correlation with patient demographics, history of presenting illness, and prior imaging. Rapid interval onset, irregularity of involved wall, and adjacent hematoma may favor the presence of a pseudoaneurysm (63). Abdominal aortic pseudoaneurysms are considered at a high risk of rupture and merit rapid treatment (62). Given that these are a rare form of abdominal aortic dilatation, the remainder of the mémoire refers to conventional, true aneurysms of the abdominal aorta.

2.2.2 Epidemiology and Risk Factors

AAAs have an overall prevalence of 4.8% across studies (4) with an incidence of 0.4% per year in Western populations (64). Most aneurysms identified in screening programs are small (<4.0 cm) (65). There is a greater prevalence of AAAs in males (6.0%) than in females (1.6%) (4); however, it is unclear if this is due to underlying protective factors (such as estrogen) or due to underdiagnosis (66). There is heterogeneity in the prevalence of AAAs between different countries and ethnic groups; for example, AAAs are more prevalent in Western countries than in Asian countries (4). Similarly, in the United States of America,

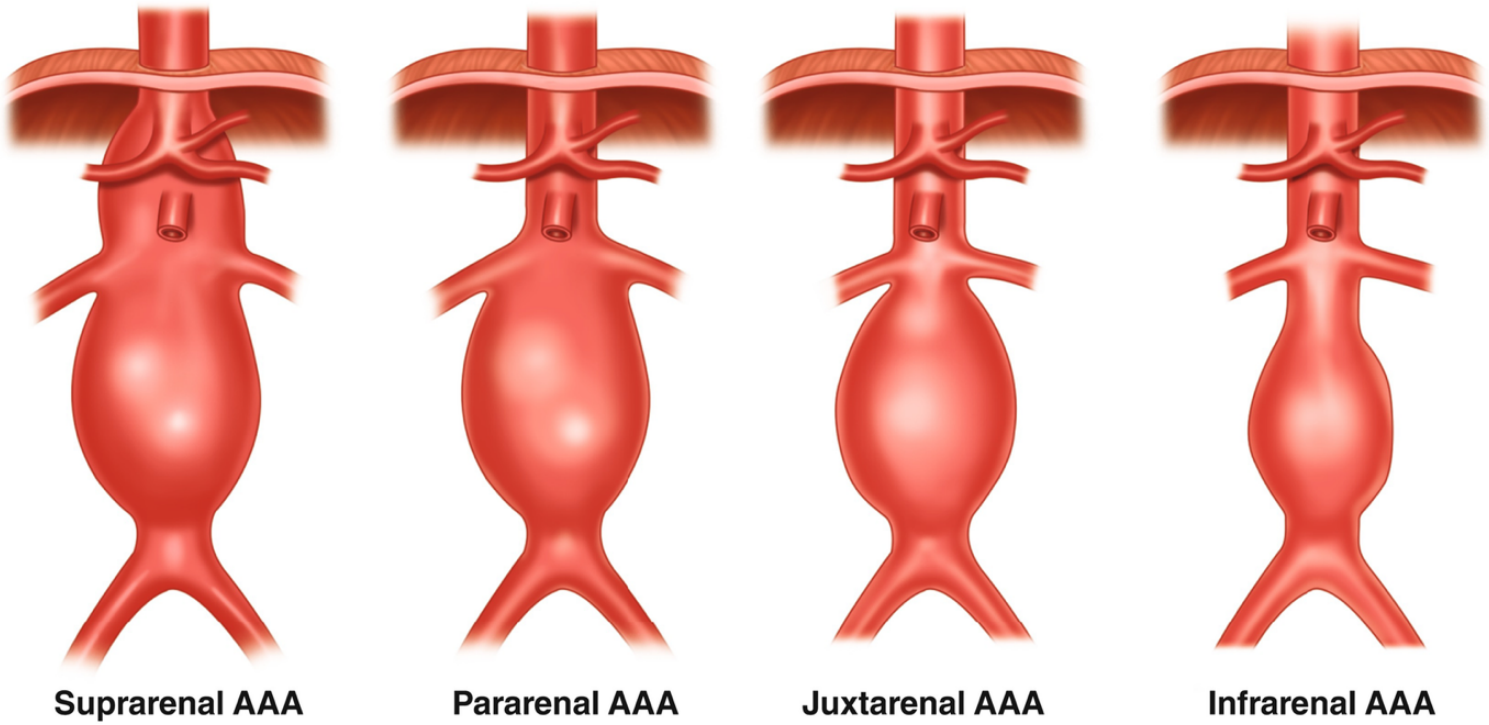

Figure 6 Abdominal aortic aneurysms (AAAs) may be classified with respect to their location relative to the renal arteries. Suprarenal AAAs extent superiorly to the renal arteries and can involve visceral branches such as the superior mesenteric artery or celiac artery. In pararenal AAAs, the renal arteries are involved but the aneurysmal dilatation does not extend superiorly to them. Juxtarenal AAAs extent to involve just the inferior aspect of the renal arteries. Infrarenal AAAs, the most common type of AAAs, begin at least 1 cm distal to the renal arteries. All aneurysm shown are of the fusiform morphology, although saccular aneurysms are possible. Finally, aneurysms may extend inferiorly to the common iliac arteries (or even more distal branches). Adapted from (67).

Caucasians have a higher prevalence of AAAs compared to other ethnic groups (3). While literature in the early 2000s suggested that there was an increasing incidence of AAAs (58), more recent studies have found that the prevalence of AAAs has been decreasing (68). This has been mainly attributed to the decrease in prevalence of smoking (69).

Smoking is the dominant risk factor for the development and growth of AAAs (2, 3). In a study of 126 196 participants, participants with a history of smoking had 2.97 times greater odds of having an aneurysm between 3.0-3.9 cm and 5.07 times greater odds of having an aneurysm ≥ 4.0 cm. In fact, three quarters of aneurysms ≥ 4.0 cm were accounted for by the excess prevalence of smoking (70). The number of cigarettes smoked and the duration of smoking are also associated with increased odds of having an AAA, while the number of years since cessation of smoking is inversely correlated with AAA incidence (3). The impact of smoking on the pathophysiology of AAAs has not been completely elucidate; however, it may be due to activation of matrix metalloproteinases (MMPs) (see **Section 2.2.3**) (71).

AAAs are more prevalent in the elderly population and increasing age is a significant risk factor for developing an AAA. For example, one study found that individuals between the ages of 80-84 had an odds ratio of 28.37 of having an AAA, while those between 55-59 had an odds ratio of 2.76 of having an AAA (3). One cohort study in Norway found no individuals under the age of 48 with an AAA (65). This observation supports the theory that most AAAs—particularly those that are fusiform—develop chronically.

AAAs are also thought to have a genetic basis. 10-20% of individuals with an AAA report disease within a first degree relative (72), with the highest prevalence amongst brothers (32%) (73). A twin study from Sweden also revealed that the odds ratio of a monozygotic twin having an AAA when their twin had one was 71 (74). The increased prevalence of AAAs in Caucasian men may have a genetic etiology (66). Studies have implicated mutations in genes responsible for forming constituents of the extracellular matrix, such as those involving collagen (such as collagen III), in the development of AAAs, although likely with low penetrance (75, 76). Genome-wide sequencing has implicated several other genes involved in lipid metabolism, the cell cycle, inflammation, cell signaling, and the renin-angiotensin system (77). Certain known connective tissue diseases, such as Marfan syndrome—caused by an autosomal dominant mutation in the *FBN1* gene—or Ehlers-Danlos syndrome—caused by a variety of mutations—are also highly associated with AAAs (78, 79)

Studies have also found a positive association between AAAs and dyslipidemia, atherosclerosis elsewhere within the body, aneurysms elsewhere within the body, and hypertension (3). Some of these findings give credence to the hypothesis that AAAs and atherosclerosis share similar developmental pathways; however, as will be seen **Section 2.2.3**, this explanation is incomplete.

The minority of aneurysm are thought to arise from a singular pathology, such as trauma, prior surgery, a penetrating atherosclerotic ulcer, or infection (58). These aneurysms are more likely to be saccular in morphology (28).

2.2.3 Pathophysiology

The precise pathophysiology underpinning the formation of AAAs is not completely understood. Conventionally, AAA development was thought to be a sequela of atherosclerosis (80). However, histopathological and biochemical data have called this conclusion into question. Atherosclerosis is predominantly an intimal disease characterized by the development of lipid-laden plaques. AAAs, in contrast, demonstrate profound degradation of the media and adventitia with evidence of oxidative stress, fragmentation of elastin and collagen fibers, depletion of vascular smooth muscle cells (likely through apoptosis), and inflammatory cell infiltration (77, 81, 82). While some of these features may be seen in atherosclerosis, others are somewhat distinct. Therefore, while atherosclerosis may play a role in the development of AAAs (or may simply co-exist with AAAs), it is felt that inflammation is the primary driver of AAA pathophysiology (83).

Matrix metalloproteinases (MMPs) are key role players in this inflammatory pathway (52). MMPs are secreted by mesenchymal cells and break down constituents of the extracellular matrix, including collagen, elastin, proteoglycans, and fibronectin (81). Elastin and collagen degradation are thought to be associated with aneurysmal distension and rupture, respectively (72), although some studies have emphasized the role of collagen degradation in both of these processes (84). When elastin within the media is attenuated and the vessel expands, the adventitia remodels and becomes thicker and more fibrotic. However, this wall, which is composed of water-soluble collagen, is weak and can be further degraded by MMPs (82). Smoking has been associated with increased MMP activity (85) and estrogens may be associated with decreased MMP activity (86).

The baseline composition of the abdominal aorta may also contribute to aneurysm formation. The infrarenal aorta has fewer functional units of elastin compared to more proximal parts of the aorta, which may predispose it to expansion (77). The media within the infrarenal aorta is poorly vascularized and reliant on simple diffusion for nutrient exchange, which may predispose it to inflammatory damage (77, 83). Finally, the precursor cells of the vascular smooth muscle cells of the abdominal aorta appear to be more susceptible to aneurysm formation in comparison to those that develop into the thoracic aorta (83).

2.2.4 Complications of AAA

The natural history of AAAs is progressive expansion and the most feared complication of AAAs is rupture (87). Aneurysm rupture occurs when the mechanical stress imposed on the aortic wall is greater than

the wall strength (88) (see **Figure 7**). In hospital mortality rates for ruptured AAAs were found to be up to 65.9% in England and 53.05% in the United States (5); however, many cases may not present to the hospital, and mortality rates may be higher (6). Other potential complications of AAAs include peripheral thrombotic disease (from thrombi originating in the aneurysm) and erosion into the surrounding structures (89).

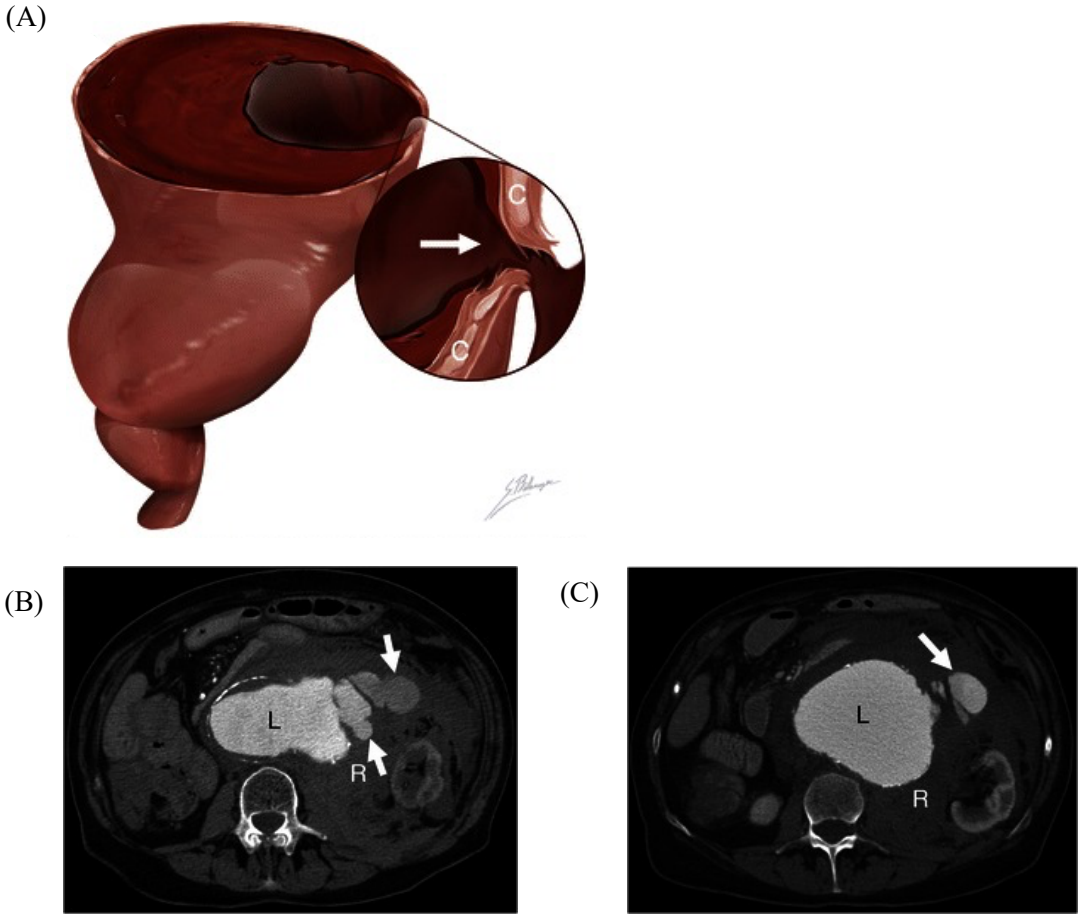

Figure 7 Abdominal aortic aneurysm (AAA) rupture. (A) Schematic of focal discontinuity within the wall of an abdominal aortic aneurysm indicating rupture. C: calcifications, which are displaced. (B) and (C) Contrast enhanced axial computed tomography angiogram images demonstrating rupture of an AAA. In (B), iodinated contrast material—which under normal circumstances is found within the confines of the arterial system on arterial imaging—is visualized leaving the confines of the enlarged, dysmorphic AAA lumen (L) and travelling into the retroperitoneum (R), as denoted by the arrows. This finding is termed extravasation and is specific for aneurysm rupture. In (C), the massively enlarged aorta is again visualized, with the extravasated contrast seen tracking inferiorly. Adapted from (90).

Aneurysm size is the most commonly used clinical parameter to predict risk of rupture. Smaller aneurysms tend to remain uncomplicated; in fact, elderly patients with small aneurysms are likely to die from other issues than from rupture. Larger aneurysms, conversely, are at a much higher risk of rupture (91). For example, aneurysms measuring greater than 8.0 cm have an annual risk of rupture of 30-50% per year, while those measuring <4 cm may have a rupture risk as low as almost 0% per year (92).

There are several additional factors that may predict aneurysm rupture. Aneurysms that grow rapidly (> 1 cm/year) are considered to be at higher risk for rupture (92). Continued smoking is associated with continued aneurysm expansion and rupture (2, 93). Women tend to present to hospital with rupture more commonly than men (21% vs. 15%) (94). Previous guidelines have indicated that saccular aneurysms are at higher risk of rupture due to the asymmetry of the wall (95, 96); however, some clinical reports have noted that saccular aneurysms do not have an increased growth rate compared to fusiform aneurysms (97). Other factors, such as hypertension, history of transplant, peak aortic wall stress, recent surgery, and antibiotic use may also be associated with an increased risk of rupture (83).

2.2.5 Clinical Presentation

AAAs may be detected asymptomatically, symptomatically, or as a ruptured aneurysm (89). The majority of AAAs are clinically silent. Asymptomatic AAAs may be detected through screening programs (98), as a pulsatile abdominal mass on physical exam (99), during the work-up for the management of peripheral vascular disease (such for claudication or after the discovery of a peripheral aneurysms) (89), or incidentally in the context of other radiological examinations (100). Symptomatic (non-ruptured) aneurysms typically present with abdominal pain, although pain radiating to the back, flank, or groin is possible (101). The pain may be dull, aching, and non-specific; it is thought to be secondary compression/erosion of the surrounding structures, rapid expansion, and/or low-grade inflammation (89). Symptomatic AAAs may also present with acute limb ischemia secondary to embolization of thrombus or debris (102). Ruptured AAAs present as severe acute abdominal pain with hemodynamic instability; however, presentation to medical attention may be delayed given the tamponading effect of the retroperitoneum (89).

2.2.6 Screening for AAAs

The United States Preventative Task Force published guidelines in 2019 recommending ultrasound screening for AAAs in men between the ages of 65-75 with a history of smoking (103). Furthermore, they also recommended selective US screening in men who were non-smokers between the ages of 65-75 (such as those with a family history). The task force recommended against screening women without family history or a history of smoking and cited insufficient evidence to recommend for/against the screening of women between 65-75 with a history of smoking or with a family history of AAAs (98). In contrast, the

Society of Vascular Surgery recommends the inclusion a one-time screening for women who have smoked or who have a family history of AAAs (1, 104). Screening in men over 65 has been shown to decrease mortality rate secondary to AAAs as well as ruptures rates; however, it is not associated with an overall improvement in mortality (105).

Chapter 3 – Treatment of Abdominal Aortic Aneurysms

This chapter will outline the two methods of treatment of AAAs: open aneurysm repair (OAR) and endovascular aneurysm repair (EVAR).

3.1 Indications for Intervention

The indications for treatment of AAAs are stratified based on the clinical presentation of the patient. In the elective, asymptomatic population, treatment is directed towards the prevention of complications—predominantly of rupture—and is predicated on the aneurysm size and growth. Repair is indicated for aneurysms that are ≥ 5.5 cm in diameter (1). Women with aneurysms ≥ 5.0 cm in diameter may also be considered for repair given their tendency to present with rupture at smaller aneurysm sizes. (1, 66). Asymptomatic aneurysms that grow rapidly (≥ 1 cm year in diameter) should also considered for repair (106). In the symptomatic patient (particularly in the case of rupture), prompt treatment is indicated (1).

3.2 Open Aneurysm Repair

OAR is an invasive surgical procedure. It may be performed via a transperitoneal or a retroperitoneal approach. The transperitoneal approach will be described as it is the more classic form, although the retroperitoneal approach may be favored in certain circumstances (such as in the case of a hostile abdomen). OAR is performed under general anesthesia. The surgeon performs a midline laparotomy to gain access to the abdominal cavity. The overlying structures are mobilized and retracted to visualize the aorta and its major branches. The surgeon cross-clamps the aorta proximal to the aneurysm, and, more distally, cross-clamps either the distal aorta (less common), iliac arteries, or external iliac arteries (depending on the extent of repair desired); distal control may be achieved first to prevent embolic showering to the pelvis/lower extremities. The aorta is then transected vertically and a graft made of polyester or polytetrafluoroethylene is anastomosed to the proximal and distal sites. The aortic wall is sewn over the graft and the abdomen is closed (107). See **Figure 8** for further details.

OAR tends to be a more durable repair when successful performed; however, it is limited by high peri-procedural morbidity and mortality. Studies quote periprocedural mortality in the region of 3-5% (7-10); death tends to be caused by multi-organ failure (107). In surviving patients, OAR is also associated with more frequent end-organ complications (including cardiopulmonary, renal, and gastrointestinal complications) in comparison to EVAR, with cardiopulmonary complications being most common. There is also the risk of development of an anastomotic aneurysm, graft infection, and lower extremity ischemia (1). A substantial number of patients post-OAR will also have long term laparotomy complications (108). OAR is contraindicated when the risk of rupture is outweighed by the risk of the procedure. Other factors,

such as obesity and significant medical or surgical comorbidities, may act as relative contraindications to OAR and steer the treating team towards EVAR (107).

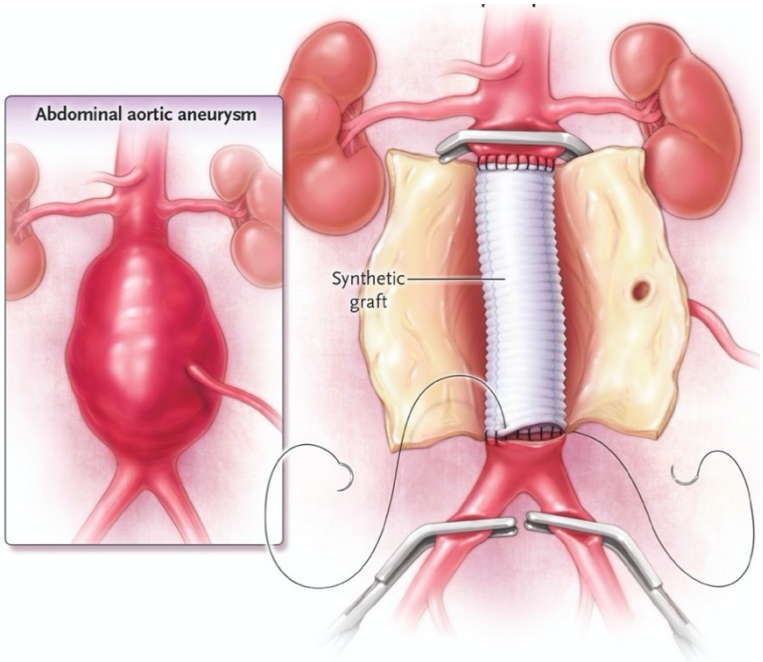

Figure 8 Schematic demonstrating open aneurysm repair of an abdominal aortic aneurysm (AAA). On the left, an infrarenal AAA is visualized. On the right, major steps in aneurysm repair are visualized. The aorta and the common iliac arteries can be seen cross-clamped. The aneurysm has been incised and a graft is being sewn in place at the level of the proximal and distal aneurysm. After the graft is sewn into place, the aorta is sewn over to cover the graft. Adapted from (109).

3.3 Endovascular Aneurysm Repair

EVAR is the minimally invasive counterpart to OAR in the treatment of AAAs (72). EVAR may be performed under conscious sedation (73). In EVAR, an intraluminal stent-graft (see **Figure 9**) is deployed within the abdominal aorta under fluoroscopic guidance with the use of injected intravascular contrast agents for localization. Access to the aorta is achieved in a retrograde fashion using vascular sheaths that are inserted in the common femoral arteries either percutaneously or via a surgical cutdown (73). The deployment device, as well as various other catheters, are inserted into the aorta to deploy the stent. Once deployed, the stent excludes blood flow from the aneurysm sac, thereby allowing the sac to depressurize, shrink, and thrombose (74). After a successful EVAR, the aneurysm sac tends to decrease in diameter over time (75). See **Figure 10** for further procedural details.

Several anatomic considerations may preclude the performance of EVAR and should be identified on pre-procedural imaging. Of note, a hostile proximal neck (the region between the aneurysm and the renal

arteries) that is short, angulated, tortuous, or highly thrombosed/calcified may act as a relative contraindication to EVAR. While EVAR is best suited for smaller, infrarenal AAAs, fenestrations within the graft as well as more advanced techniques make the treatment of juxtarenal, pararenal, and suprarenal aneurysms possible (74, 76).

The principle complications of EVAR include endoleaks (77), ischemic complications (78), and stent-graft migration/kinking (79). Endoleaks are a broad topic and will be discussed in **Chapter 4**. The ischemic complications of EVAR are diverse and may include colonic ischemia, spinal ischemia, buttock claudication, and lower limb ischemia. They may occur due to branch occlusion during stent deployment, thrombosis of a stent-graft limb, or the showering of thrombi. (78). Of note, many of these complications are shared with OAR (12). Stent-graft migration refers to caudal migration of the stent, which may incompletely exclude blood flow from the aneurysm sac. Histopathological examinations of explanted stented aortas reveal that there is often little tissular infiltration of the stent-graft from the aorta to promote anchoring (80); thus, the graft relies mechanical forces to retain its configuration. Over time, the downward pulsation of blood flow in combination with changes in aneurysm morphology may overcome these resistive forces. Clinically, risk of migration has been associated with small proximal fixation length (79) as well as dilatation of the infrarenal aortic neck (81). Stent-graft migration may be treated with the insertion of an extensor module, conversion to open repair, or watchful waiting (79).

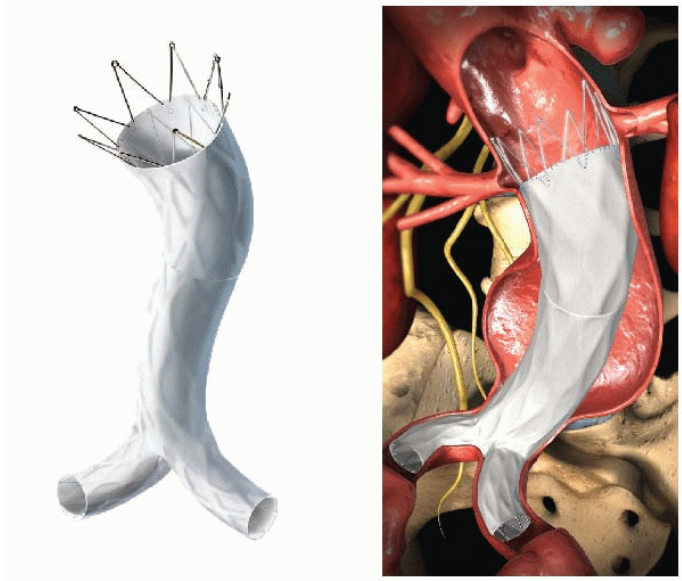

Figure 9 Endovascular aneurysm repair (EVAR) stent. This is a unibody model (AFX; Endologix). Other stents may have a separate, modular component for one of the iliac limbs. Adapted from (110).

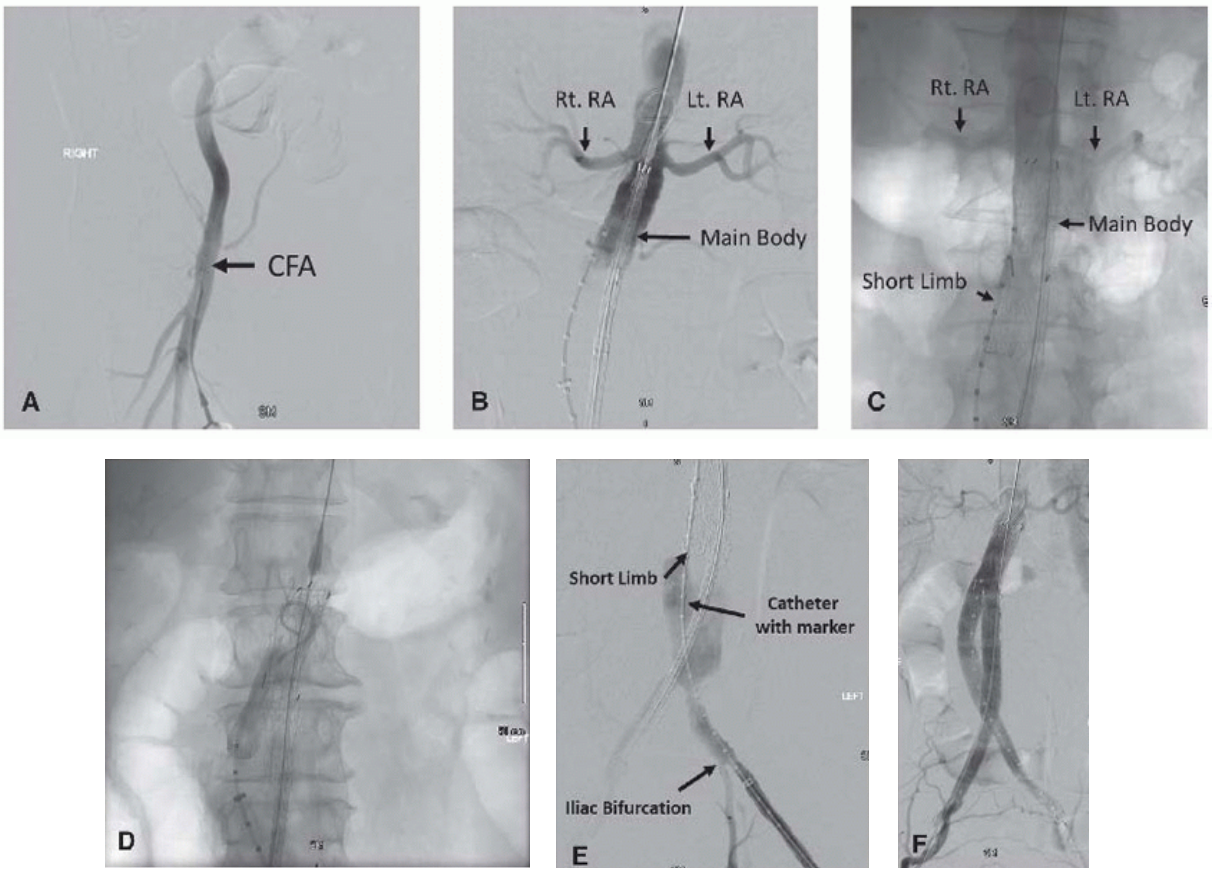

Figure 10 Intraprocedural angiograms demonstrating endovascular aneurysm repair (EVAR) stent deployment. (A) The common femoral artery (CFA) has been punctured, catheterized and opacified with contrast material. CFA catheterization enables access to the abdominal aorta. (B) The deployment catheter (containing the EVAR stent, which is labelled Main Body) is visualized just inferiorly to the renal arteries. RA; renal artery. Rt: right; Lt: left. (C) The main body of the stent has been deployed. Of note, there is a long limb that extends to the ipsilateral side of the common iliac puncture. There remains a short limb that must be catheterized from the contralateral side. (D) The short limb is catheterized via a contralateral approach through the left CFA. (E) The deployment device for the short limb is passed into the gate for the short limb. Deployment is not shown. (F) Completion angiogram demonstrating opacification of the stent. Adapted from (82).

3.4 Comparison of Open Aneurysm Repair and Endovascular Aneurysm Repair

EVAR has emerged as the preferred therapeutic modality for AAAs in the elective population. In the cohort included in the National Surgical Quality Improvement Program between 2005 and 2011, 74.9% of AAA repairs were performed endovascularly (12). EVAR is associated with a significantly lower peri-procedural mortality (0.5-1.7%) in comparison to OAR (3-4.7%). However, there was no significant difference between the two modalities with respect to aneurysm-related mortality or overall mortality at intermediate follow-up (up to four years) or long-term follow-up (greater than four years) (6, 8, 9, 13, 14). Procedural time, loss of blood, and length-of-stay (in both the intensive care unit and the hospital overall) are lower with EVAR. However, patients who undergo EVAR are more likely to require secondary reinterventions (although the majority are minimally invasive) (6). OAR is associated with only a 1.4% rupture rate on long-term follow-up, in contrast to 5.4% with EVAR. Given this, OAR may be safer in a low-to-moderate risk group with minimal comorbidities, good pre-operative fitness, and a longer life expectancy (111).

Both EVAR and OAR may also be used in the context of ruptured AAAs. A 2017 Cochrane review demonstrated that—given the limitations of the paucity of data available—there was moderate evidence suggesting that there was no difference between EVAR and OAR with respect to periprocedural mortality in the treatment of ruptured aneurysms (112). The review could not comment upon the mid- and long-term effectiveness of either treatment. Clinical guidelines, however, recommend EVAR over OAR whenever possible in this context (1).

The data within the literature regarding the cost effectiveness of the OAR and EVAR are inconsistent but appear to favor OAR. For example, a systematic review and economic model of the mid-term data of the major clinical trials comparing OAR and EVAR suggested that EVAR was not a cost-effective alternative to OAR with respect to quality adjusted years of life (113). In contrast, a systematic review of the long-term data suggested that EVAR may be cost-effective in the United States, but not in European countries, with EVAR costing £73 000 for every quality adjusted life year due to surveillance and reintervention in the United Kingdom (114). A more recent review has suggested that the answer is simply unclear, given the underlying heterogeneity of the data reported in the literature (115). However, given the rapid evolution of stent-graft technology, changes in fee structures, improved technical expertise with respect to EVAR, changes in indications for reintervention for EVAR-related complications, and the cultural shift in preference of EVAR, it is unclear as to how relevant these cost analyses will be in future years.

Chapter 4 – Endoleaks

4.1 Definition and Types

Endoleaks are the most common complication of EVAR and may occur in upwards of approximately 35% of cases. They are defined as blood flow within the aneurysm sac but outside of the stent-graft (15, 116). There are five types of endoleaks (see **Figure 1** in **Chapter 1**).

Type I endoleaks occur when blood travels beyond the proximal or distal stent-graft attachment sites into the aneurysm sac in an anterograde or retrograde fashion. These are subdivided as type IA endoleaks (proximal attachment site) and type IB endoleaks (distal attachment site). Type I endoleaks tend to occur in patients with complex anatomy, extensive calcification, or extensive thrombus formation at the level of the proximal neck or common iliac arteries (117). They may also develop over time as the configuration of the aneurysm changes (118). Type I endoleaks are considered high pressure endoleaks and are associated with aneurysm growth and rupture (1, 118).

Type II endoleaks are the most common type of endoleak and have a pooled prevalence of 22% across studies (34). They occur secondary to retrograde blood flow into the aneurysm sac through a collateral vessel—such as the inferior mesenteric artery or a lumbar artery. This flow may be low velocity and low pressure (118) or reach close to systemic pressures (119). Type II endoleaks that are not associated with aneurysm growth may be followed with serial imaging, as many remain stable in size or spontaneously regress (120). However, type II endoleaks that persist over six months are associated with adverse outcomes such as aneurysm expansion, increased intervention, conversion to open repair, and rupture (121).

Type III endoleaks are caused by a defect/tear in the graft material or a disconnection between the modular components of the graft, allowing blood to enter the aneurysm sac. These defects may be caused by repetitive stress on the graft from aortic pulsations or due to changes in biomechanics of the graft as the aneurysm shrinks (117). These, like type I endoleaks, are considered high pressure leaks (118).

Type IV endoleaks refer to the transient flow of blood through the stent graft material seen intraprocedurally on angiography. These tend to resolve once intraprocedural anticoagulation is halted. While they are of little clinical concern, care should be taken to exclude other types of endoleak (117, 118)

Type V endoleaks refer aneurysm expansion without radiological evidence of blood flow into the aneurysm sac. These endoleaks are also called endotension. The nature of type V endoleaks are unclear; they may be positional, secondary to a slow flowing or even sealed endoleaks, or be secondary to the accumulation of fresh thrombus (26, 122). These are considered low pressure endoleaks (118).

4.2 Follow-up Timeline

Routine imaging post-EVAR is mandatory to assess for complications, namely for endoleaks, but also for stent-graft migration, kinking, and thrombosis (amongst other complications). The Society for Vascular Surgery recommends that a follow-up computed tomography (CT) examinations be performed 1 month and 12 months post-procedurally (12); if the 1-month CT demonstrates evidence of a complication that does not require immediate intervention (such as a type II endoleak), then an additional CT at 6 months can be performed (100). If there is no complication after one year of follow-up, patients may be followed with duplex ultrasound (DUS). While MRI is more sensitive than both CT and DUS (see below), it is not specifically recommended for routine surveillance and is typically reserved for problem solving. Endoleaks may present years after EVAR, thus, life-long surveillance is mandatory (12).

4.3 Conventional Imaging Modalities for EVAR Follow-up

4.3.1 Computed Tomography

Computed tomography is a form of cross-sectional imaging that employs X-rays, a form of ionizing electromagnetic radiation. CT scanners contain multiple X-ray tubes with diametrically opposed detectors that are affixed to a circular gantry that rotates around the patient during acquisition. As the gantry rotates, the patient is moved through a predetermined scan field on a motorized table to acquire three dimensions of images. During each acquisition, X-rays are projected from the X-ray tubes towards the patient; some of these X-rays are attenuated (absorbed or scattered) by the patient, while others pass through the patient and are detected by the detectors (see **Figure 11**). The amount of energy that is detected is inversely related to amount of energy that is attenuated by the patient's body. Within a given axial cross-section of the patient's body, different tissues will attenuate X-rays differently. The tissue attenuation (expressed mathematically as its attenuation coefficient) is related to the tissue's density as well as its atomic numbers. Structures with high attenuation coefficients (e.g. bone and metal) will attenuate much of the incident X-ray beam, while structures with low attenuation coefficients (e.g. air and fat) will attenuate less of the incident X-ray beam. The detected X-rays can be used to generate maps (images) of the relative attenuation values for the different tissues within the patient's cross-section, with each pixel on this map corresponding to a particular attenuation coefficient. Clinically, the attenuation coefficients are expressed as Hounsfield units (HU). By definition, water is 0 HU and air is -1000 HU. Fat is less than 0 HU (usually around -100 HU) and bone is much greater than 0 HU (usually > 1000 HU). On greyscale CT imaging, structures with higher attenuation coefficients appear brighter/whiter (123).

Intravenous contrast agents are often employed during CT examinations to improve contrast resolution. CT contrast agents contain iodine, which has a high atomic number and a high attenuation coefficient. The

distribution of contrast material through the body is considered to be flow-limited; thus, the location of enhancement (i.e. area of increased attenuation) is dependent on where it has been pumped by the cardiovascular system. Contrast is typically administered via a peripheral vein and progressively travels through the venous system, the right heart, the pulmonary circulation, the left heart, the systemic circulation, the end organs, and then back through the venous system; eventually, it is excreted by the kidneys into the bladder. Different structures will show greater enhancement depending on when the image is taken with respect to the time of injection of the contrast (124). Contrast administration is crucial in the assessment of post-EVAR complications.

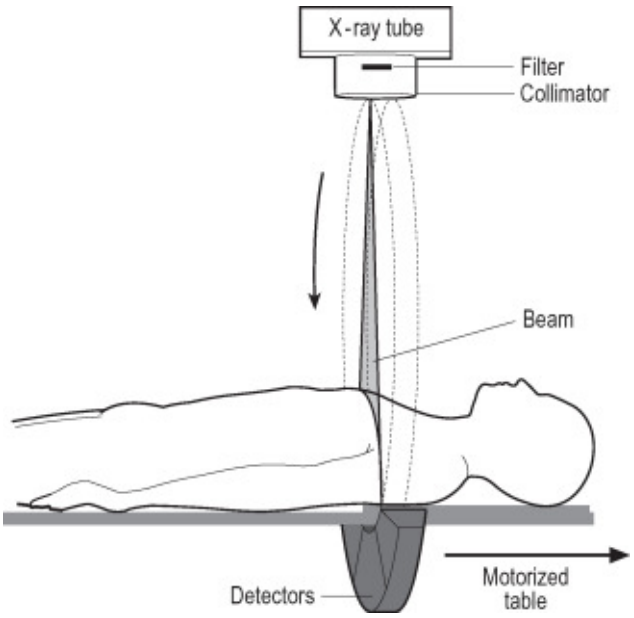

Figure 11 Simplified schematic of a computed tomography (CT) imaging system. The X-ray tube produces X-rays. The filter and collimator alter the beam-shape to optimize patient coverage. The X-ray detectors are located opposite to the X-ray tubes and detect incident X-rays that have not been attenuated by the patient. The gantry, which actually contains several X-ray tubes and detectors, rotates during acquisition while the motorize table moves the patient through the scan field. Adapted from (125).

CT is the reference standard for EVAR follow-up given its high sensitivity and specificity for endoleaks (92% and 90%, respectively) (105), low-intermediate cost, and widespread availability (106). See **Figure 12** for an example of an endoleak diagnosed with CT. In the follow-up of EVAR, imaging is typically performed in the unenhanced, arterial, and portovenous phases (107). The unenhanced phase is useful for the detection of mural calcification and other spontaneously hyperdense materials that may be misinterpreted as an endoleak on the enhanced phases. Contrast-enhanced studies are mandatory to assess for stent patency as well as for the presence of an endoleak, which will be seen as contrast opacification

outside of the stent but inside the aneurysm sac. The portovenous study is useful for the detection of slow flow endoleaks and also provides the optimal enhancement of the end-organs visualized within the study. The specific imaging characteristics of a given endoleak will be predicated on its type, as seen in **Table 2**. All phases may be used to detect sac growth, stent kinking, and stent migration. The use of CT is limited by the cumulative radiation exposure associated with multiple follow-up studies; the potential harm of contrast agents, which are nephrotoxic and which may cause allergic reactions; and the cumulative cost of repeated studies (106). Furthermore, given that it is a static modality, CT may misclassify endoleaks (108).

Figure 12 Type Ia endoleak. (A) and (B) Computed tomography (CT) angiograms post-EVAR demonstrating contrast opacification of the aneurysm sac originating from the region of the proximal attachment site (white arrowheads). (C) Angiography confirms the presence of a type I endoleak (black arrowheads). Adapted from (118).

Endoleak type	CT imaging features
Type I:	General: Often associated with sac expansion when compared to prior imaging. Unenhanced: May detect spontaneously hyperdense material within the aneurysm sac near the proximal or distal attachment site, suggestive of acute hemorrhage. Enhanced: Collection of contrast material inside the sac, visibly arising from the proximal or distal attachment sites (types Ia or Ib endoleaks, respectively).
Type II:	General: Often not associated with increased sac size; may spontaneously decrease in size or thrombose. Unenhanced: Spontaneously hyperdense material within the periphery aneurysm sac (i.e. may be away from the stent) near a collateral vessel Enhanced: Contrast material within the aneurysm sac adjacent to an enhancing collateral branch (e.g. lumbar, inferior mesenteric artery), which may represent an inflow vessel. There may be delayed opacification given that some of these endoleaks are slow flow. Note that an opacified vessels may not necessarily be source of the endoleak, but rather the outflow vessels from a type I or type III endoleak
Type III:	General: Often associated with sac expansion when compared to prior imaging. Unenhanced: Spontaneously hyperdense acute hemorrhage near the body of the stent-graft, away from the attachment sites. May see component separation. Enhanced: Large enhancing collection near the body of the stent-graft. Contrast may be seen exiting a defect in the stent or at a site of component separation.
Type IV:	Not applicable. Type IV endoleaks are transiently seen during stent-graft implantation and resolve once anticoagulation has been halted.
Type V:	General: Sac expansion without demonstrable evidence of an endoleak (i.e. no contrast opacification of the sac).

Table 2 Computed tomography (CT) findings of endoleaks. Adapted from (126, 127).

4.3.2 Magnetic resonance imaging

Magnetic resonance imaging (MRI) applies the principles of electromagnetism to generate diagnostic images (128). MRI machines apply a strong, uniform magnetic field to the patient. This causes hydrogen atoms, which are found ubiquitously throughout the body—although in different amounts and in different microstructural environments—to precess (or spin) at the Larmor frequency, either anti-parallel, or, more frequently, parallel to the uniform magnetic field (see **Figure 13**). This creates a net weak nuclear magnetization in the direction of the applied field. Radiofrequency (RF) pulses can then be applied—using RF coils—at the Larmor frequency perpendicular to magnetic field to cause a net magnetization shift into the transverse plan (i.e. perpendicularly to the previously described direction of net nuclear magnetization). The hydrogen atoms may then return to the original direction of net nuclear magnetization. The changes in magnetization induce voltages within the RF coil and, after many repetitions, the signal can then be used to generate images. Additional coils—called gradient coils—are used concurrently to help with signal localization in either two dimensions or three dimensions—the latter of which is useful for creating multiplanar reformats.

Two major imaging sequences—T1- and T2-weighted images—can be derived from the received signal. The signal intensities (brightness) of a given tissues in each sequence depends on the environment of the hydrogen atoms (128). On T1 images, fat is hyperintense and water is hypointense, whereas on T2 images, fat and water are hyperintense. Modifications can be applied to these sequences to improve contrast resolution (for example, fat-suppression techniques on T2 imaging, so that only water is hyperintense), but the specifics are beyond the scope of the present document (128, 129). Gadolinium-based contrast agents—much like iodinated contrast agents in CT—can be used to increase signal intensity and improve tissue contrast, such within the arterial system. In contrast to iodinated contrast agents—which attenuate X-rays—gadolinium-based contrast agents decrease the T1 relaxation time, resulting in increased T1 signal (129).

MRI protocols for EVAR follow-up include several sequences. A standard protocol may include an axial T2-weighted sequence, an axial T1-weighted pre-contrast study, two bolus-timed 3D T1-weighted post-contrast studies (the addition of the second study is thought to improve sensitivity, although it is not universal), and a final axial post-contrast T1 weighted 2D sequence (130-132). On MR, endoleaks are defined as areas of enhancement within the aneurysm sac but outside on the stent-graft on gadolinium-enhanced T1-weighted images (see **Figure 14)**. They may be categorized in a similar fashion compared to **Table 2** for CT (130-132). T2 imaging may also be used to identify fresh clot (hyperintense), which may be contributory to endotension or sac non-shrinkage (26).

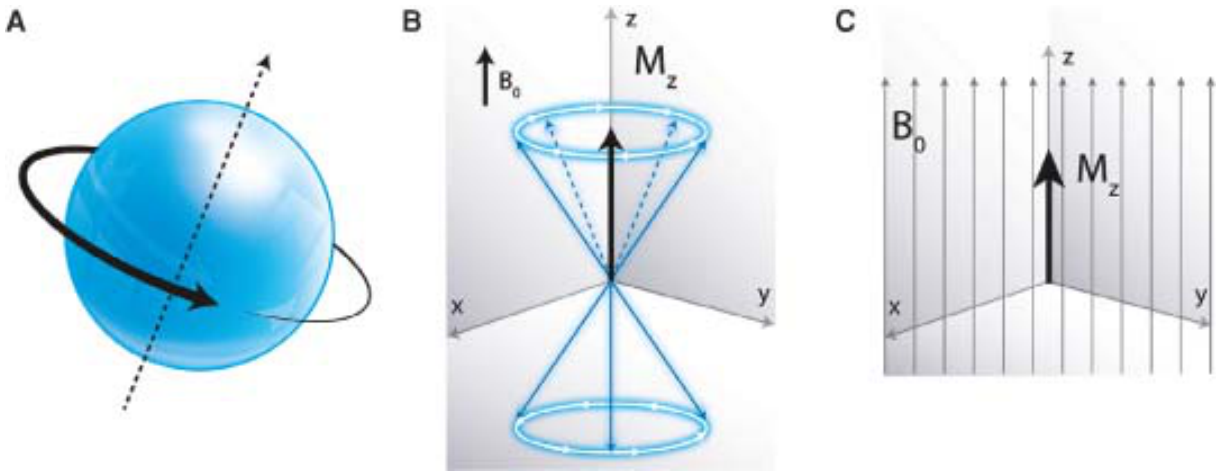

Figure 13 Select illustrated principles of magnetic resonance imaging (MRI). (A) Every proton in the human body has an axis of nuclear magnetization termed a spin (dotted arrow). (B) When a homogenous magnetic field (B_0) is applied to a tissue, its protons will align themselves either parallel or antiparallel to the magnetic field and then precess (rotate) at the Larmor frequency. More protons will align their axes of nuclear magnetization parallel to B_0, so the net magnetization of the protons (M_z) will be in the direction of B_0. (C) The M_z is again shown in the direction of B_0. Adapted from (128).

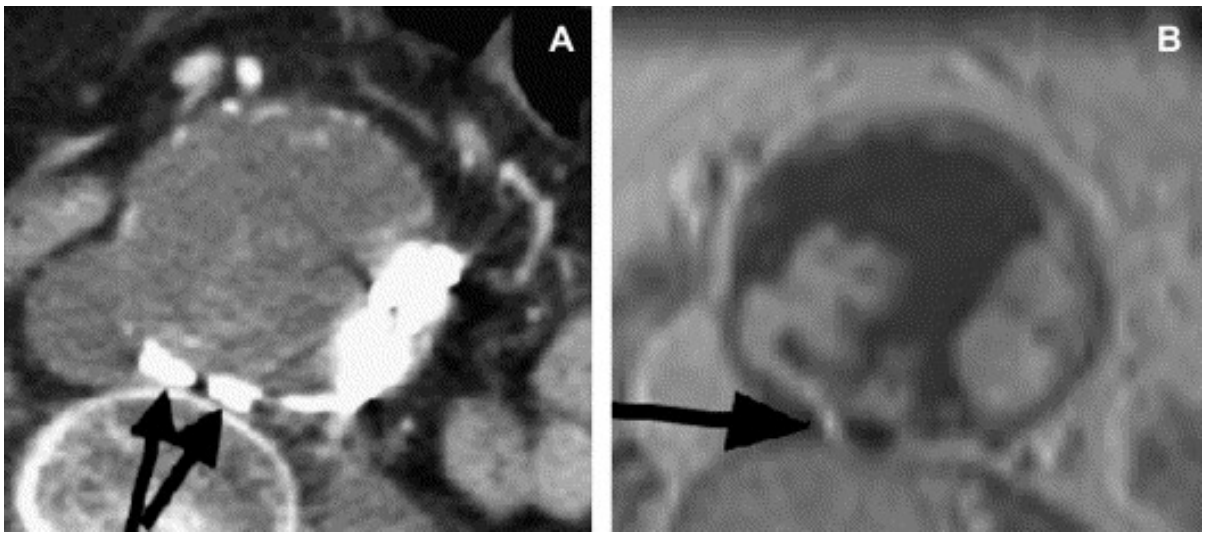

Figure 14 Magnetic resonance images of a type II endoleak. (A) Computed tomography (CT) of an abdominal aortic aneurysm status post endovascular aneurysm repair (EVAR) and surgical clipping of paired lumbar arteries (arrows). As per the authors, the endoleak was occult. (B) T1 post-contrast axial image of the corresponding aneurysm demonstrates hyperintense contrast extending from the region of the clips (arrow) into the aneurysm sac, suggestive of a type II endoleak. Adapted from (108).

MRI is the most sensitive modality for detecting endoleaks. It is considered superior to the reference standard, CT, given its superior soft tissue contrast (130). A review published in 2013 found that MRI was able to detect 126 additional endoleaks compared to CT, although it did miss two. While the majority of the endoleaks detected by MRI were type II endoleaks (69%), 10% were type III endoleaks (which typically require urgent therapy); the remainder were indeterminate. The use of albumin-binding contrast agents, which remain intravascularly longer and result in increased T1-shortening, may improve sensitivity for endoleaks (21). The majority of present-day stent-grafts, which are nitinol-based, do not result in significant susceptibility artifact (signal alteration due to magnetic field inhomogeneities), except perhaps at the level of the struts. MRI also avoids the use of ionization radiation and, like CT, is much less operator dependent than ultrasound. While these advantages make MRI an enticing modality for post-EVAR follow-up, it does suffer from several disadvantages. MRI has increased scan times compared to CT. It may be poorly tolerated by claustrophobic patients. It is less widely available compared to CT and ultrasound. Its use is contraindicated in patients with certain implanted devices (such as certain pacemakers). Finally, stainless steel and Elgiloy® alloy EVAR stent-grafts may generate susceptibility artifacts, which may decrease the sensitivity of the study (130).

4.3.3. Ultrasound

Ultrasound (US) imaging will be described in detail because it is the basis of elastography, which will be further described in **Chapter 5**.

US imaging involves the emission and detection of high frequency (1-20 MHz) ultrasound waves. US waves are mechanical pressure waves that propagate through media via the sequential compression and rarefaction of particles (see **Figure 15**). In US imaging, US waves are produced and detected using handheld probes that contain piezoelectric crystal transducer elements. These crystals convert electrical energy into ultrasound waves and vice-versa. A conventional probe may have several elements organized in an array, each of which emits and detects ultrasound waves along a line of sight. Each element sequentially emits a short pulse of sound waves through the tissue; they then detect subsequently reflected soundwaves and convert the energy into an electrical signal. This signal contains information regarding depth and contrast of the underlying tissue (133). The totality of the lines of sight can be used to produce an US image (134).

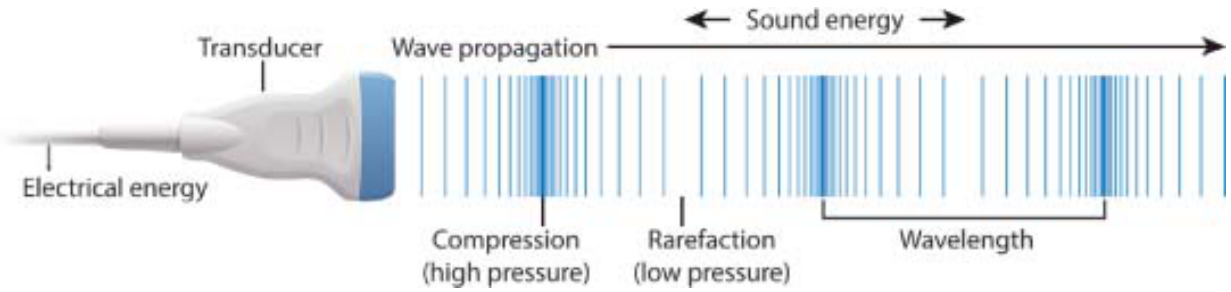

Figure 15 Ultrasound transducers use piezoelectric crystals to high frequency pressure waves with alternating regions of high pressure and low pressure. Adapted from (133).

A fundamental concept that allows for tissue contrast in ultrasonography is acoustic impedance. Acoustic impedance is the product of tissue density and the speed at which sound travels through the tissue. Sound waves travel faster in non-compressible materials (such as bone) and slower in compressible materials (such as air). When two tissues of dissimilar acoustic impedances are adjacent, ultrasound waves will reflect from their interface and may be detected by the transducer. Tissues with greater differences in acoustic impedance will reflect a greater proportion of incident ultrasound waves (133).

Another important US principle is scatter. Incident US waves scatter in random directions away from the beam when they encounter structure much smaller than their wavelength. Many organs/tissues have a complex microstructure that cause characteristic ultrasound wave scattering patterns. These patterns are intrinsic to the tissues and changes in the speckle pattern may be indicative of disease. On imaging, different tissues and lesions may be described by their relative echogenicity in comparison to surrounding tissues. Tissues that are hyperechogenic scatter more than the surrounding tissue, while the opposite is true for tissues that are hypoechoic (133).

Depth on US imaging is derived from the time it takes for an emitted US bream to return to the probe. Ultrasound technology assumes that waves travel through tissue at a constant velocity of 1540 cm/s. Thus, once a pulse is emitted, a reflected echo that takes longer to be detected by an element is calculated to be farther away from the probe than one that is detected sooner. Of note, the further away an object is from the transducer, the more signal is lost (such as from scattering and absorption)—this is termed attenuation. A time gain compensation is applied to the received signal to compensate for this (134). Lower frequency transducers attenuate less (and therefore penetrate more) and may be used to image deeper structures; however, they also tend to have lower spatial resolution (133). The fundamental assumption that ultrasound waves travel at 1540 cm/s is fairly accurate for soft tissue, but not for other structures (such as bone and air), which may result in signal loss or artifacts.

There are several different modes of US display. Regardless of the method of presentation, the raw signal (radiofrequency (RF) signal) must be post-processed to create a diagnostic image. Two of the most common modes of display are B-mode (brightness mode) and M-mode (motion mode) imaging. In B-mode imaging, a brightness value—related to the detected signal amplitude—is presented at each depth for each line of sight (on the y-axis) across the lateral distribution of the scan lines (x-axis). This provide a real time cross-sectional image of the scan field. B-mode imaging is the most common display mode used in diagnostic imaging (see **Figure 16**). M-mode imaging, in contrast, presents time on the x-axis and depth on the y-axis, again with different tissue echogenicities presented at each depth, for a narrow line-of-sight. M-mode is useful for analyzing motion of a limited line of sight over time, such for visualizing cardiac valves. A-mode imaging, which plots depth on the x-axis and signal amplitude on the y-axis is infrequently used clinically but is involved in 1-D transient elastography (see **Section 5.3**) (134).

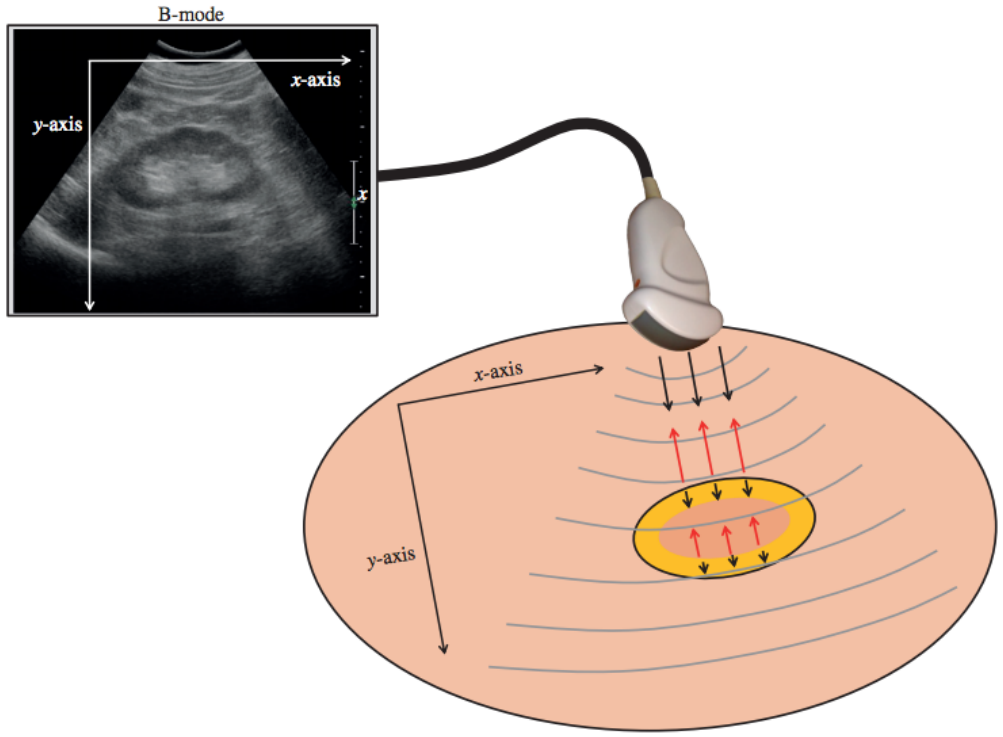

Figure 16 Schematic of brightness mode (B-mode) ultrasound (US) imaging of the kidney. High-frequency sound waves are emitted by the ultrasound probe, which are returned back to the ultrasound probe due to reflection and scattering induced by the underlying tissue. The mechanical energy of the returning sound wave is converted into an electrical signal, which is used to produce brightness values on a coordinate system defined by the x-axis and y-axis. Adapted from (135).

Doppler imaging is an important adjunct to B-mode imaging and is used to characterize moving objects. Doppler analysis hinges on the Doppler effect: as a moving source of sound comes closer to an observer, the perceived frequency of the sound increases; as the source moves further away, the perceived frequency of the sound decreases. Similarly, in the context of US, as an object moves closer to the transducer, the frequency of its backscattered echoes increases; as it moves away, the frequency of these echoes decreases. One of the main uses of Doppler analysis is in the characterization of blood flow. Color Doppler analysis presents the average frequency shifts of the individual pixels within a region of interest (such as a blood vessel) as a two-dimensional image. The average value of these shifts is color-coded; by convention, red indicates motion towards the probe, and blue represents motion away from the probe. Color Doppler signals are generally superimposed upon B-mode images to combine motion information with the baseline reflector characteristics of the tissue. This is termed Duplex ultrasound (DUS). Pulse-wave Doppler is another form of Doppler imaging that allows for waveform characterization of a small region of interest (134).

Both B-mode and Doppler imaging are critical in sonographic follow-up post-EVAR. B-mode imaging is used to assess for changes in aneurysm diameter as well as to assess stent-graft morphology and location. Given that the probe can be angulated to adjust for the tortuosity of aneurysmal vessels, US may have a greater sensitivity for true aneurysmal diameter than axial CT slices (although the standard is to use obliquely reformatted CT images when the aneurysm is tortuous) (136). Endoleaks may be visualized as mobile echoes within the aneurysm sac but are best characterized as abnormal regions of Doppler signal within the aneurysm sac, outside of the stent-graft (see **Figure 17**). The type of endoleak will be predicated on the origin of Doppler flow within the aneurysm sac. While certain wave forms patterns on Doppler imaging have been associated with endoleak closure, progression, or resistance to treatment, these findings are controversial (137).

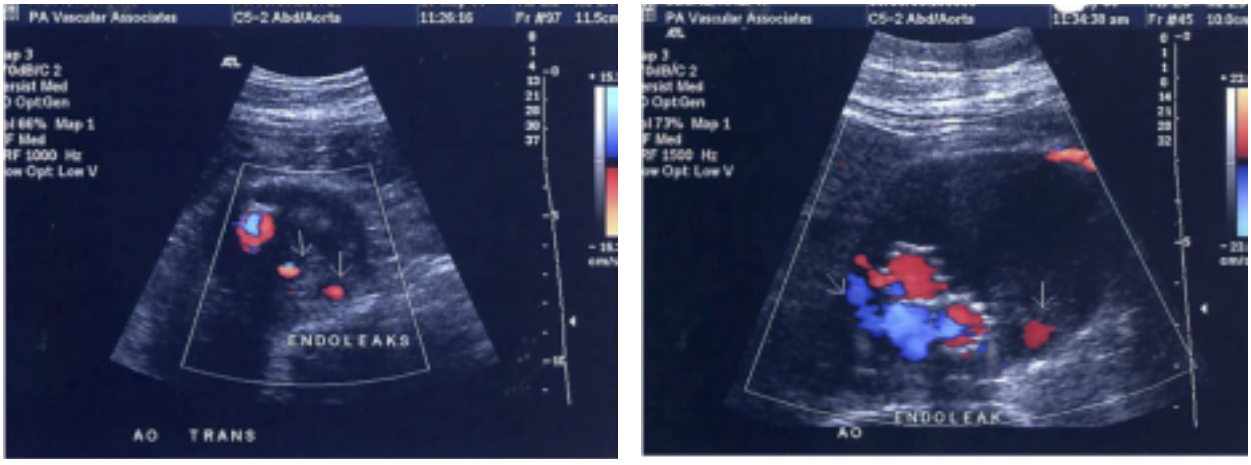

Figure 17 Duplex ultrasound examination demonstrating foci of Doppler signal outside of the stent but inside the aneurysm sac (arrows) in keeping with endoleaks. Adapted from (137).

Duplex ultrasound is recommended for follow-up imaging after EVAR once there is no evidence of complications on post-procedural CT scans (1). It is safe, widely available, inexpensive, and avoids the harms of ionizing radiation. It is also dynamic; high velocity endoleaks (favoring type I or type III) may be missed or misinterpreted as type II endoleaks on static CT images (138, 139). However, US is operator dependent (140), may be non-diagnostic in obese patients due to low penetration (141), and may be technically limited due to obscuration of the sonographic window by overlying structures. Ultrasound is also less sensitive and specific than CT. An early meta-analysis comparing the two modalities (with CT being considered the reference standard) found that US had a pooled sensitivity of 69.1% and a specificity of 90.6% (18); a more recent Cochrane review found that ultrasound had a sensitivity of 82% and a specificity of 93% for endoleaks (17). In addition, US may miss or overcall findings that may change management. For example, in one study, US missed 27 endoleaks in 17 patients, two of which were type I endoleaks. There was also poor correlation between changes in aneurysm size detected by US in comparison to CT (141). However, other authors have suggested that the majority of endoleaks that are missed by US are type II endoleaks (142) and that CT identifies too many endoleaks that do not require therapy (138). Contrast-enhanced ultrasound, which uses a non-nephrotoxic contrast agent that contains echogenic microbubbles, has improved sensitivity for endoleaks (143). However, it may not be sensitive enough to detect stent-graft migration or kinking (144); its use is contraindicated in patients with certain underlying cardiac pathologies (144); and there are barriers to its uptake in clinical practice (145).

4.4 Treatment of Endoleaks

The treatment of endoleaks are geared towards their type. Special attention will be paid to type II endoleaks.

4.4.1 Treatment of Type I Endoleaks

Type I endoleaks are associated with high velocity blood flow and elevated sac pressures. As a result, they are at a high risk for sac expansion and rupture and are generally promptly treated. Type Ia endoleaks may be treated with balloon angioplasty, placement of a balloon expandable stent, placement of an extension cuff, placement of a fenestrated stent-graft (if the extension will extend above the renal, mesenteric and/or celiac arteries), or placement of endoluminal staples or anchors (1, 146). Embolization with coils and glue may also be considered (147). Type Ib endoleaks usually treated by inserting a leg extension (1). Refractory type I endoleaks may necessitate conversion to open repair (1).

4.4.2 Treatment of Type II Endoleaks

Type II endoleaks are commonly seen intraprocedurally during EVAR as well as on follow-up imaging. There is currently no indication for the treatment of type II endoleaks discovered intraprocedurally, as approximately half of type II endoleaks will spontaneously resolve (1). One study found that that while type II endoleaks were found in 24% of cases intraprocedurally, they were found in only 9% of cases at 6 months follow-up (148). When a persistent type II endoleak is present, approximately 25% of aneurysm will regress in size while approximately 25% will grow (1). Type II endoleaks may also spontaneously appear over one year after EVAR secondary to the recruitment of alternative vascular pathways; these endoleaks are suggested to have a lower tendency to resolve, with approximately 55% requiring intervention. Some authors have suggested increased screening and a lower threshold to intervene in these cases (149). Ultimately, there is controversy within the literature regarding the most appropriate time to intervene on type II endoleaks (150), with authors suggesting that a selective approach is both safer and more cost-effective (151). One review suggested that therapy should be pursued only if there is sac growth after six months, persistence of the endoleak over 12 months without sac growth, or if sac pressures reach over 20% of the systolic pressure (152). In contrast, another study found there was insufficient evidence to recommend a threshold for therapy (150). Overall, the majority of type II endoleaks do not require intervention (153).

When treatment of a type II endoleak is indicated, the favored approach is embolization (see **Figure 18**). Several approaches to embolization have been identified, including transarterial, translumbar, and transcaval embolization. The transarterial approach is currently favored when feasible as both diagnostic angiography and therapy can be performed simultaneously; however, a translumbar approach is an acceptable alternative (154). Complete embolization of the entire sac as well as the feeding and outflow vessels is recommended, as embolization of the feeding vessel alone may allow for the recruitment of other vessels. This behavior has led some to compare type II endoleaks to arteriovenous malformations (36, 37, 155). Several embolic agents—including thrombin, coils, n-butyl cyanoacrylate, and Onyx (ethylene vinyl copolymer acetate)—have been reported in the literature with varying degrees of success (see **Section 4.5.1**) (156-161). Surgical ligation of the feeding vessel is a more invasive possibility (162); however, this again may result in additional vascular recruitment. Regardless of the agent or approach used, type II endoleaks tend to be refractory to therapy, with overall long-term success in only approximately 40% of cases (35).

Prophylactic interventions to prevent endoleaks during stent deployment have also been reported. Such maneuvers include embolization of the lumbar vessels (163) and inferior mesenteric artery (164) or immediate thrombin injection within the aneurysm sac (165). However, given their associated risks, costs, and mixed evidence in the literature (166), these approaches have not been widely adopted. The one exception to this is prophylactic embolization of the internal iliac artery when its orifice will be covered by the stent (127).

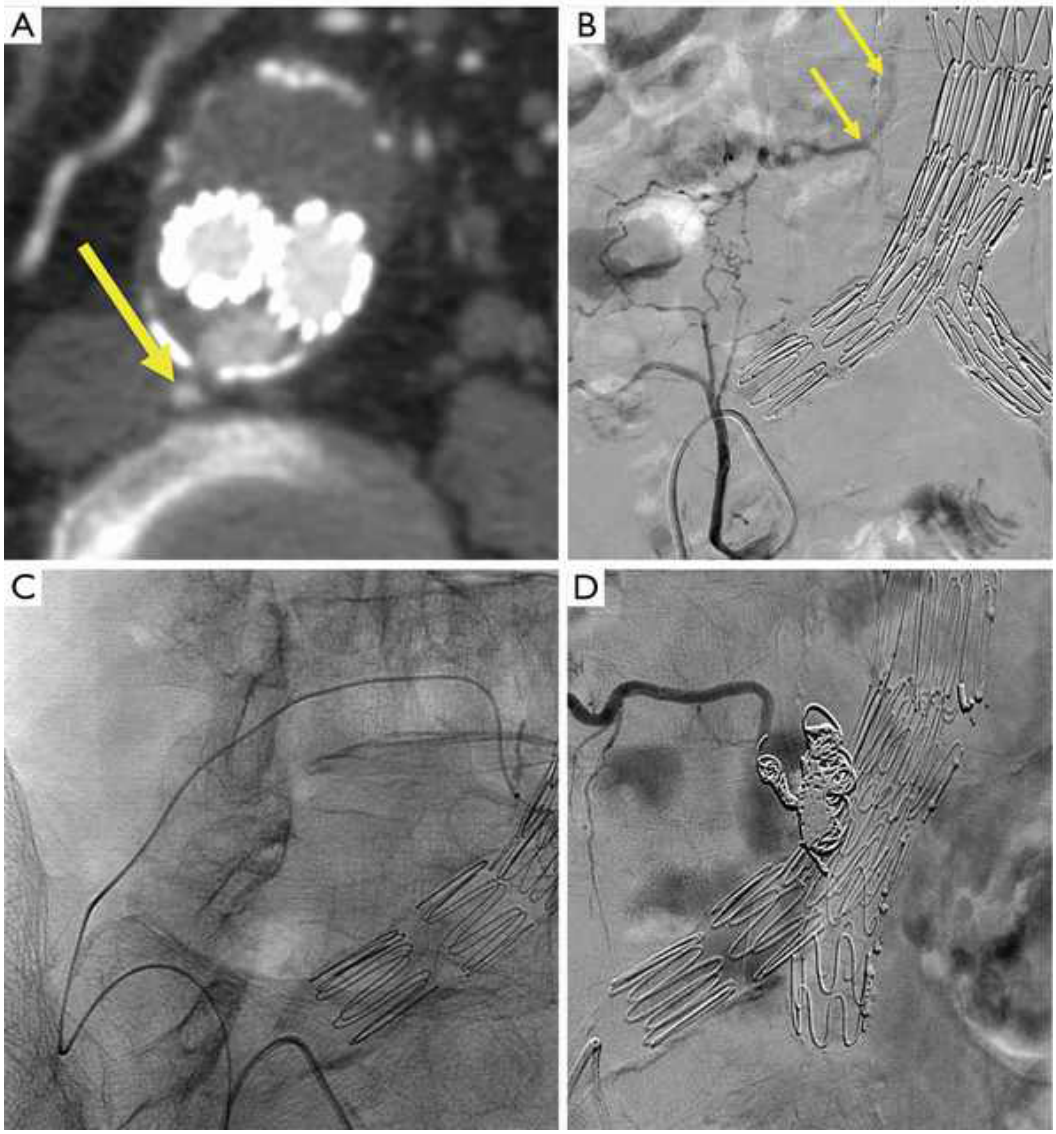

Figure 18 Transarterial coil embolization of a type II endoleak. (A) A type II endoleak fed by a lumbar artery is identified on contrast enhanced computed tomography (CT); the arrow points to the feeding vessel. (B) Selective angiogram of the right internal iliac artery demonstrates that the lumbar vessel (arrows) is fed by the right iliolumbar artery. (C) A microcatheter is advanced to the endoleak. (D) The endoleak nidus and feeding artery have been coiled. There is no opacification of the endoleak upon contrast administration. Adapted from (36).

4.4.3 Treatment of Type III Endoleaks

Type III endoleaks—like type I endoleaks—are associated with rapid aneurysm expansion and rupture and merit prompt treatment. These endoleaks may be treated with redeployment of a new stent-graft to reline

the original stent-graft, thereby covering the membrane perforation or bridging the gap between the stent-graft modules (1, 146).

4.4.4 Treatment of Type IV Endoleaks

Type IV endoleaks require no treatment and spontaneously resolve after re-normalization of coagulation parameters.

4.4.5 Treatment of Type V Endoleaks

Endotension is treated on an individualized approach. As type V endoleaks are not, by definition, associated with radiological evidence of blood flow within the aneurysm sac, they may be monitored clinically and radiologically. Follow-up imaging may reveal an occult type I-III endoleak, and treatment would be predicated on the type. Alternatively, if no other type of endoleak is found and there is continued expansion, therapy may involve relining the stent-graft with a new material, adding extension cuffs, or conversion to open repair (146).

4.5 A New Agent to Treat Endoleaks: CH-STS

4.5.1 Limitations of Current Embolic Agents for the Treatment of Type II Endoleaks

Type II endoleaks remain a therapeutic puzzle with long term success of only approximately 40% across therapies (35).

Onyx appears to be the most successful agent, with a clinical success rate of approximately 79% (157). Onyx is composed of ethylene vinyl alcohol copolymer (EVOH), which is dissolved in a solution of dimethyl sulfoxide (DMSO) prior to deployment. It also contains radiopaque tantalum powder to aid in fluoroscopic visualization. The major advantage of Onyx is that it can be deployed slowly to form a cast within the endoleak, enabling controlled embolization of the nidus as well as the inflow and outflow vessels (37). However, Onyx suffers from several disadvantages. While demonstrating superior initial clinical success when used as the primary therapeutic agent, its success rate is only about 50% when used after initial treatment failure, performing no better than other therapeutic options (35). Onyx is very expensive, costing approximately $2500 per 1 mL vial. It is tedious to prepare—as the powder and solvent must be heated and agitated—and it must be deployed slowly (0.16 mL/minute). DMSO is also a toxic solvent and that requires specialized catheters to prevent catheter damage. Finally, tantalum powder is permanently radiopaque, causing streak artifact on follow-up CT imaging that may limit the detection of recurrent endoleaks (35).

There are several other embolic agents that have been reported in the literature, all of which suffer from similar disadvantages. Coil embolization is the most widely used treatment option (36). However, it is associated with increased rates of reintervention due to preserved flow within the tracts between the individual coils. Furthermore, coils cause permanent streak artifact and can decrease the sensitivity of follow-up imaging for recurrent endoleaks. They are also expensive (although less so than Onyx) (35, 167). Cyanoacrylate glue is another commonly used agent (168). However, it is technically difficult to prepare and to deploy as it must be titrated with the contrast agent lipiodol, which affects polymerization time. This may result in non-target embolization and inadvertent gluing of the catheter to the surrounding structures (37). Thrombin is another proposed agent; however, even when used intraprocedurally, it is not associated with a significant decrease in post-procedural endoleaks (38).

Given the limitations of commercially available embolic agents, there was a demonstrable need for an improved therapeutic option for the treatment of type II endoleaks. Research in endovascular therapy has established that persistence of the endothelial lining is associated with treatment failure after embolization (169). Preclinical AAA models have shown that that endoleaks comprise channels lined with endothelial cells (39, 40) and that the mechanical ablation of the endothelial layer of the aneurysm wall promotes the closure of endoleaks. However, this effect is mitigated when a collateral vessel is present. Therefore, endoleak recanalization is thought to be mediated both by persistent blood flow as well as the deposition of progenitor endothelial cells (170, 171). It was therefore hypothesized that an embolic agent that promotes both vascular occlusion and endothelial denudation would be particularly valuable in the treatment of endoleaks (172).

4.5.2 Development and Evaluation of CH-STS in vitro and in vivo

Based on this hypothesis, Drs. Lerouge and Soulez collaborated at the Centre de recherche du Centre hospitalier de l'Université de Montréal (CRCHUM) to develop a sclerosing embolic agent named CH-STS. It has been patented and licensed to Cook Medical, an international leader in endovascular therapy.

CH-STS is an embolic agent that comprises chitosan, the sclerosant sodium tetradecyl sulphate (STS), and a non-ionic contrast agent. Chitosan is a biopolymer that is derived from chitin, which is found in fungi and the shells of crustaceans (173). It is non-toxic and—when combined with a gelation agent such as β-glycerophosphate (BGP)—it forms a thermosensitive hydrogel, transitioning from a non-Newtonian fluid to a gel when heated (174). Consequently, chitosan hydrogels may be injectable at room temperature and occlusive at body temperature (42). Chitosan hydrogels are also biodegradable, which may allow for progressive aneurysmal thrombosis, fibrosis, and shrinkage (43, 175). STS is an anionic surfactant that is commonly used in venotherapy. It causes endothelial denudation, local inflammation, and promotes vascular occlusion. In high flow situations, STS is often combined with an embolic agent, such as Gelfoam

or coils, to promote stasis and prevent non-target embolization (176). Finally, CH-STS contains the contrast agent Visipaque™ (GE Healthcare), which is a non-ionic, iodinated contrast agent used in diagnostic CT and angiographic examinations. Visipaque™ diffuses out of the agent over 48 hours, which allows for precise image-guided visualization during embolization without negatively impacting follow-up CT imaging (41-43).

CH-STS has demonstrated favorable characteristics for endoleak embolization both in vitro and in vivo. An initial iteration of CH-STS—containing chitosan 2% weight/volume, BGP 12% weight/volume, Isovue® 300 20% volume/volume, and STS 3% weight/volume—demonstrated almost immediate gelation after preparation with a storage modulus of 1357 Pa, above the threshold of 800 Pa thought to be necessary for vascular occlusion (42, 43, 177). The storage modulus of the gel also increased over time, reaching approximately 3000 Pa after 1 week (42). In addition, CH-based embolic agents with STS have been shown to effectively remove the endothelial layer from vessels in ex vivo arterial assays (42) and, when used to embolize the auricular arteries of rabbits, CH-STS with a concentration of 3% STS resulted in a greater occlusion length compared to lower concentrations of STS (41). In a preliminary canine bi-iliac endoleak model, none of the three aneurysms embolized with CH-STS had persistent endoleaks on long term follow-up (42).

The most recent formulation of CH-STS—composed of chitosan 2% weight/volume, 12% w/v β-GP, Visipaque™ 320 30% volume/volume (changed to increase its visibility on fluoroscopy), and STS 3% weight/volume—again demonstrated a storage modulus greater than 800 Pa upon preparation and could also withstand pressures up to 220 mm Hg when tested with an in vitro embolization bench test (43). The gel was also noted to form a continuous thread during injection, which was useful to completely occlude endoleak niduses. In the same canine bi-iliac endoleak model, embolization with this formulation of CH-STS was associated with an 88% initial technical success and a 77% long term success. In comparison to embolization with a non-sclerosing chitosan hydrogel embolic agent (CH; composed of chitosan 2% weight/volume, β-GP 20% weight/volume, and Visipaque™ 320 30% volume/volume), CH-STS was associated with an 85% lower probability of residual endoleak. Finally, as seen in the ex vivo arterial study, the aneurysms embolized with CH-STS showed evidence of endothelial denudation on histopathological analysis (43).

The ability of CH-STS to promote endothelial denudation has been established, as have its favorable mechanical properties in vitro. However, given the importance of occlusivity in preventing endoleak recurrence post-embolization, it is of interest as to how the agent affects the mechanical properties of embolized aneurysms in vivo over time. Ultrasound elastography, described in the following chapter, is well suited to address this question.

Chapter 5 – Elastography

5.1 Introduction to Elastography

In clinical applications, elastography is a predominantly image-based technique that measures tissue elasticity. Elasticity is a mechanical property that refers to a tissue's ability to resist deformation when a force is applied and its tendency to resume its original configuration thereafter. It has long been observed that tissues and organs undergo changes in their mechanical properties as they undergo physiological and pathological processes (22). For example, a developing scirrhous breast cancer will demonstrate much different mechanical properties than its surrounding fibroglandular and adipose tissues (22, 178). Elastography is able to characterize these changes in a similar manner to the physical exam maneuver of palpation; however, it can better characterize deeper, smaller structures and can provide semi-quantitative or quantitative information as well (178, 179). Different imaging modalities have been investigated in the pursuit of elastographic analysis; however, US elastography has gained particular interest given that US is widely available, inexpensive, and safe (180). While B-mode imaging is limited in its ability to characterize changes in tissue elasticity (as tissue echogenicity in of itself may not correlate with stiffness), the use the basic principles outlined in **Section 4.3.3** can be used—with the application of additional sources of deformation and intensive post-processing—to calculate tissue elasticity (178). Using these means, ultrasound elastography can provide information regarding tissue stiffness, depth, and contrast (180).

The concepts of stress and strain are fundamental to elastography. Stress (σ) is a force per area (with units N/m^2) and strain (ε) is a dimensionless deformation (expansion, compression, or change in configuration). Hooke's law relates the stress imposed upon an elastic material to its strain, whereby a material's strain is directly proportional to the applied stress (of note, this only applies to linear elastic materials or within the linear-elastic portion of the stress-strain curve for reversible deformation). The factor that relates these two parameters is the elastic modulus. There are different moduli depending on the type of force applied. In the case of a normal stress (σ_n)—a force applied perpendicularly to a surface—that causes a normal strain (ε_n)—being a relative change in length that is parallel to the stress—the modulus that relates these two parameters is called Young's modulus (E). Similarly, when a tangential stress (σ_s)—being a force that is applied tangentially to a surface—causes a shear strain (ε_s)—being an angular change in configuration—the modulus that relates these two parameters is called the shear modulus (G). Materials that have greater elastic moduli are stiffer (180). Visual descriptions of the described stresses, strains, and elastic moduli are provided in **Figure 19**.

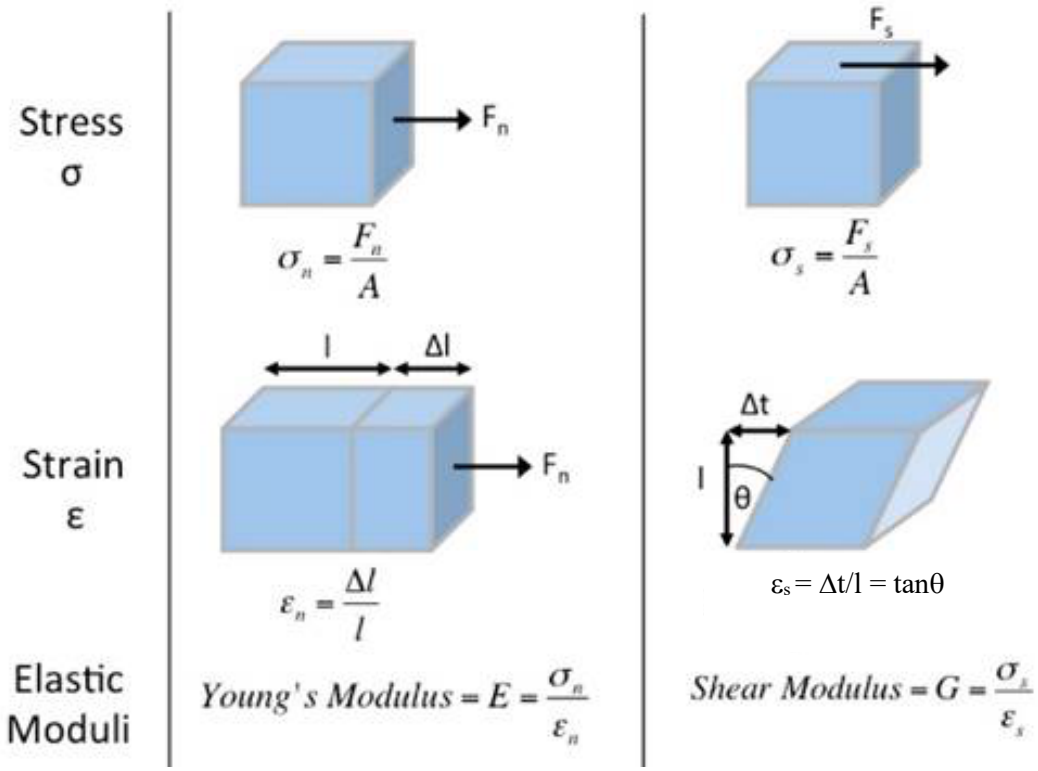

Figure 19 Stress, strain, and elastic moduli. Elastic moduli are material properties that relate an applied stress to the strain that the material undergoes. The first column of shapes describes Young's modulus. When a normal force per area (stress, σ_n) is applied to an object, there is a resultant relative change in its dimension along the vector of the force called the strain (ε_n). Young's modulus (E) is the ratio of the normal stress to the normal strain. The second column of shapes describes the shear modulus. When a tangential force per unit area (shear stress, σ_s) is applied to the surface of a material, the material undergoes an angular change in configuration, called the shear strain (ε_s). The shear modulus (G) is the ratio of the shear stress to the shear strain. F_n = normal force; F_s = shear force; A = area (normal stress: area perpendicular to the force vector; shear stress: area parallel to the force vector); l = length; θ = angle describing the shear; Δt = linear displacement surface of object surface parallel to shear force. Adapted from (180).

In all types of elastography, a stress is applied to the tissue, the tissue's resulting perturbations are measured, and the tissue's mechanical properties are inferred to aid in the characterization of pathology (179) (see **Figure 20**). There are several different methods of elastography, the most popular of which can be divided into strain imaging and shear wave imaging. Generally, in strain imaging, a normal stress is induced mechanically (22) or through an acoustic pushing pulse (181) to deform the tissue, and the normal strain is subsequently measured. Strain may be used as a surrogate/estimate for the Young's modulus. More sophisticated techniques may allow for multidirectional analysis and the calculation of shear using these techniques (182). In shear wave imaging, a mechanical device or an acoustic radiation force (183) is used to create a dynamic stress; this creates shear waves in the tissue, which may be measured either parallel or perpendicular to the initial force to calculate quantitative measurements of tissue strain and the elastic modulus (180). Further details regarding the types of impulses used in strain and shear wave imaging are provided in **Figure 21.** The present document will focus on strain ultrasonography, with reference to shear wave imaging as a comparison. Shear wave imaging in fact belongs to broader category of elastography termed dynamic elastography, which includes harmonic elastography; this type of elastography will be described briefly but will not be focused upon.

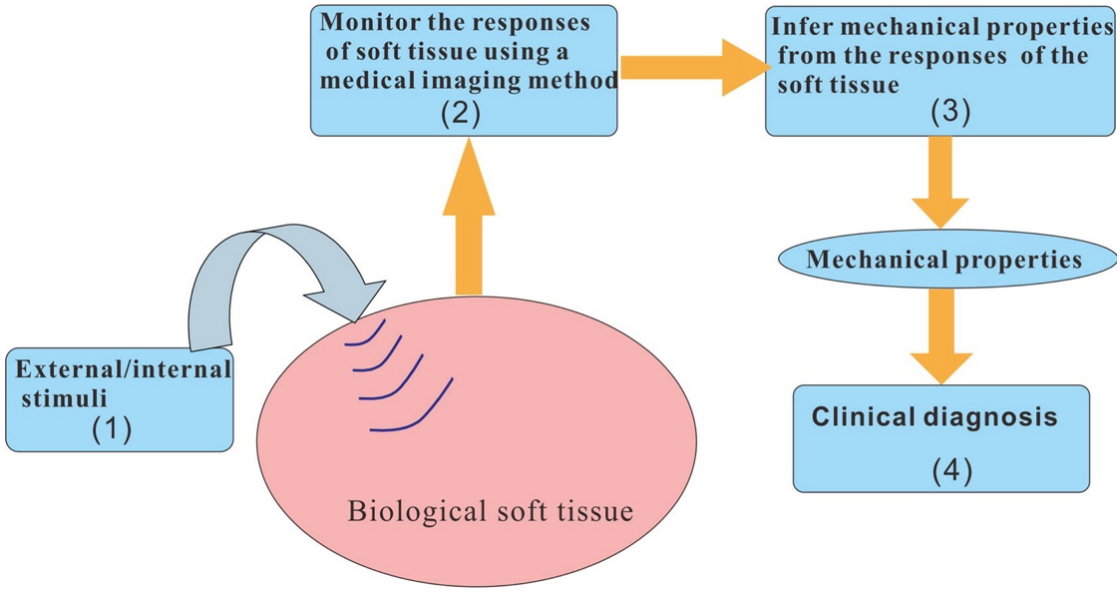

Figure 20 Schematic outlining the steps of elastographic imaging. A stimulus is applied to the tissue of interest. Imaging techniques are used to detect a response in the tissue. The measured pre- and post-excitation tissue changes are used to infer the mechanical properties of the tissue. These mechanical properties can then be used for clinical characterization and diagnosis. Adapted from (184).

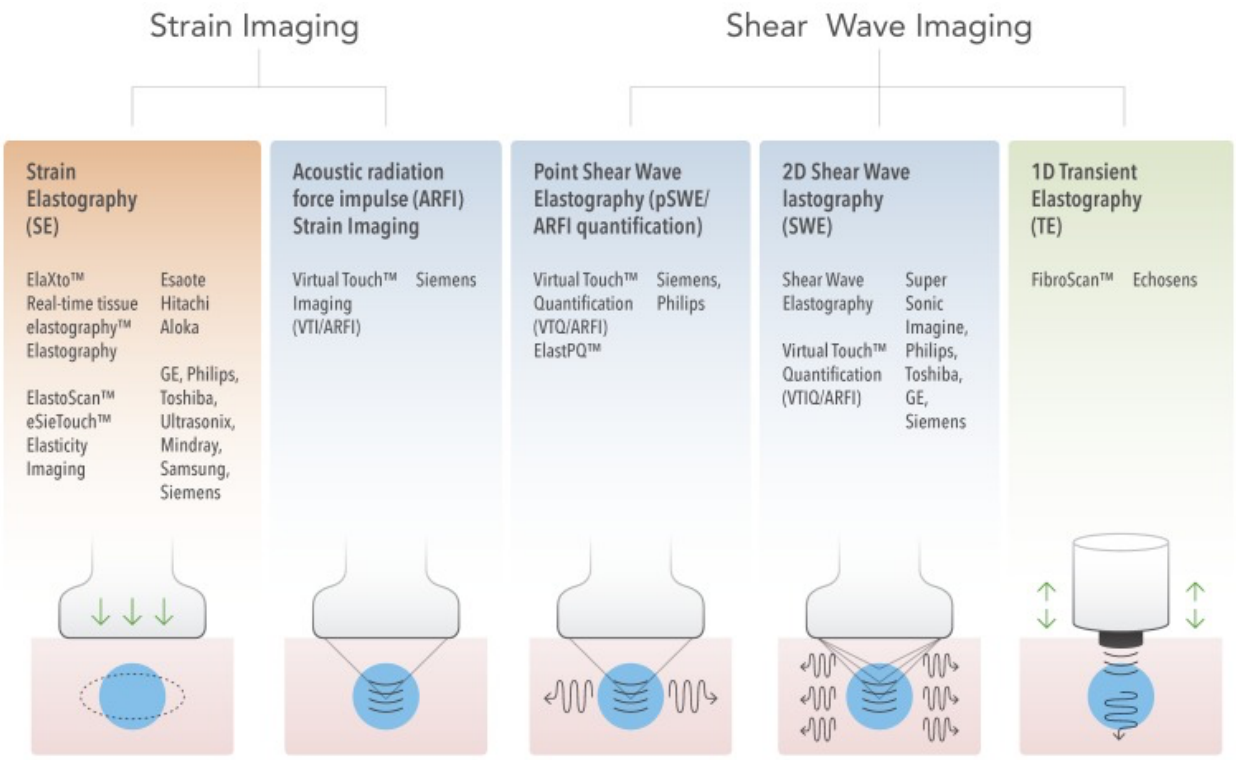

Figure 21 Different types of ultrasound elastography with their commercial counterparts. Ultrasound elastography can be divided into two major categories: strain imaging and shear wave imaging. In strain imaging, a force parallel to the transducer is used to generate tissue deformation, which is subsequently measured. Strain elastography (a subtype of stain imaging) relies on the use of an external or internal compressive force to generate deformation. Acoustic radiation force impulse (ARFI) strain imaging, in contrast, uses an acoustic pushing pulse to displace the tissue. In shear wave imaging, shear waves are generated to calculate tissue elasticity. 1D transient elastography uses a mechanical vibrating device to create shear waves that travel parallel to the incident wave. In contrast, both point shear wave elastography and 2D shear wave elastography techniques use ARFIs to generate shear waves which travel perpendicularly to the transducer. In point shear wave elastography, one focal point is interrogated to calculate Young's modulus. In 2D shear wave imaging, ARFIs are directed in multiple focal zones, which generate multiple perpendicularly travelling shear waves. This allow for real time quantitative elastographic analysis during imaging. Harmonic elastography is not included in the present figure but will be described subsequently. Adapted from (180).

5.2 Strain Imaging

Strain imaging traces its roots back to the early 1990s to the work by Ophir et al (22). Strain imaging generally relies on the application of a force during ultrasonographic examination to obtain RF signals both pre- and post-compression. In the original description of strain elastography, cross-correlation techniques were used to make pairwise comparisons between US A-mode signal lines to determine the amount of axial displacement of the tissue using a time-delay estimation (22, 178, 185) (see **Figure 22**). Since the 1990s, several innovations have been made in strain imaging with regards to the type signal information that can be used to calculate the strain as well as the number of dimensions that can be incorporated into the analysis (e.g. two and three dimensions) (185). Ultimately, in these techniques, tissues that are stiffer displace less on post-compression images and will have correspondingly lower measured strains (or deformations); this is used as a surrogate for a greater Young's modulus (see **Figure 23**) (180). Only small amounts of tissue compression are required during acquisition (0.1-2% axial dimension); since tissues deform non-linearly, excessive force may result in inaccurate/unreproducible strain measurements (185-187). The advantages of strain imaging lie in its favorable penetration and in its robustness (188). The major limitation of strain imaging is that since the stress distribution within the tissue is generally unknown, the Young's modulus cannot be readily calculated (179, 187). Strain imaging is therefore generally considered a qualitative technique, although quantitative estimates of strain may be provided. Despite this, strain imaging has gained interest in the characterization of breast lesions (189), thyroid lesions (190), and other pathologies (191).

The majority of strain elastography techniques fall under the category of quasi-static ultrasound elastography (QSUE). The descriptor "quasi-static" refers to the minimal transducer motion used during acquisition. Under the umbrella of quasi-static elastography, there are three broad categories of stress application (185). In the first type, the ultrasound transducer is used to elicit tissue deformation (22, 185). This method corresponds to the original method described by Ophir et al (22). Transducer pressure can be applied manually or with the aid of an apparatus and may be performed with only a pre- and post-compression images or with stepwise compressions (185, 192, 193). Another form of QSUE uses repetitive, cyclic, low-frequency deformations (1-10 Hz) to deform the tissue. This has been termed "palpation imaging". These frequencies are so low that they do not generate shear waves, and the deformations can be measured in a similar fashion as previously described (194). Finally, QSUE can use internal, physiological processes to generate the force, such as from the respiratory system (195) or the cardiovascular system (including the heart and major blood vessels) (196-198). The major advantage of these techniques is that they reduce operator variability with respect to the stress applied. However, the deformations can only be measured in regions near physiological stresses (e.g. near the diaphragm, heart, or major blood vessels) and the stress may not be uniformly applied in space or in time.

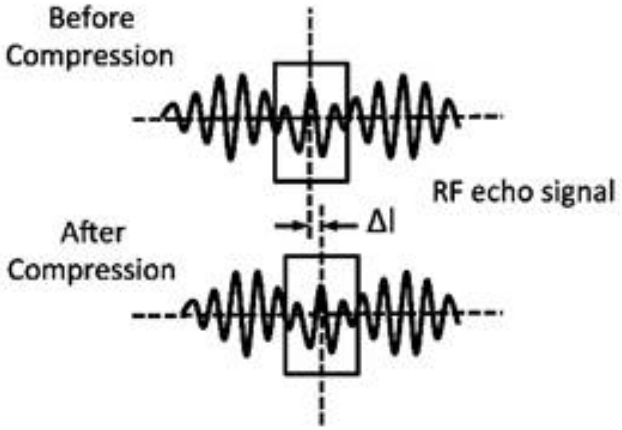

Figure 22 One form of strain elastography calculates the displacement of radiofrequency signals pre- and post-compression to estimate the mechanical properties of the imaged structure. Δl = change in length; RF = radiofrequency. Adapted from (180).

An additional, somewhat distinct form of strain imaging is acoustic radiation force impulse (ARFI) strain imaging (199). In this form of strain imaging, a short, intense, pushing pulse (ARFI) is directed towards the region of interest, which causes tissue displacement of a few hundred microns. The ultrasound probe then switches into speckle-tracking mode to calculate displacements using changes in the speckle pattern (180, 199). This technique stands in contrast to the shear wave ARFI imaging that uses ARFIs to generate shear waves, which will be described in the following section (180).

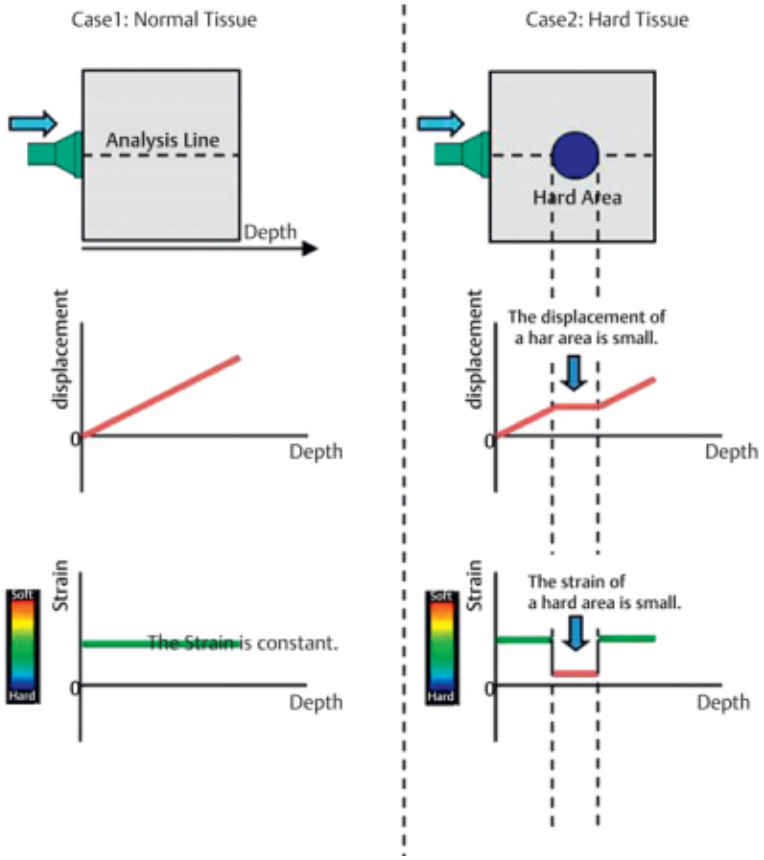

Figure 23 Schematic of strain imaging. On the left, a normal mechanical force is applied to a homogenous, compressible tissue. This causes a uniform displacement over the imaged depth and, consequently, strain analysis reveals a uniform strain. On the right, a stiff region is incorporated into tissue. When a similar normal mechanical force is applied, there is no displacement along the length of the stiff area, while the remainder of the tissue deforms as in the schematic on the left. Strain analysis reveals a lower strain in this region. This can be used as an additional feature to characterize imaged tissue. Adapted from (166).

5.3 Dynamic Elastography – Shear Wave Elastography

Shear wave imaging (SWI) or shear wave elastography (SWE) belong to a family of techniques known as dynamic elastography. There are essentially two major types of dynamic elastography: those that use harmonic excitation and those that use transient excitation (185). Harmonic elastography relies on the use of harmonic excitation to obtain a steady-state tissue response, which is subsequently used to infer the mechanical properties of the tissue (200). The steady-state excitation may be provided using vibration devices or acoustic radiation forces. Examples of dynamic elastography include sonoelastography (201, 202), shear wave induced resonance elastography (203), vibroacoustography (204), and harmonic motion imaging (205). Dynamic elastography using transient stimuli, in contrast, relies on the use of transient (as

opposed to harmonic) stimuli to generate internal shear waves within the imaged area to calculate its mechanical parameters. The most common form of dynamic transient elastography is shear wave elastography. This technique has garnered a substantial amount of attention in the literature and will be discussed in further detail (179).

There are three major forms of transient shear wave elastography: 1D transient elastography, point shear wave elastography, and 2D shear wave elastography. All forms of shear wave elastography involve the generation and characterization of shear waves to infer the imaged tissue's mechanical properties. Shear waves are low-velocity (1–50 m/s), low-frequency (10 Hz–2 kHz) waves in which the particle motion is perpendicular to the direction of wave propagation (179) (see **Figure 24**). Measurements of shear wave speed can be used to calculate the shear modulus and, subsequently, the Young's modulus.

1D transient elastography is perhaps the most basic form of shear wave elastography. In this technique, a mechanical punching device is integrated into the head of the ultrasound probe, which generates low-frequency, transient, spherical shear waves within the underlying tissue (206-208). Ultrafast imaging is used to detect tissue displacement via the diffused echoes to calculate the shear wave speed parallel to the probe, which can be used to estimate Young's modulus. 1D transient elastography relies on A-mode imaging exclusively, thus diagnostic imaging is not performed concurrently (180, 200, 206-208). 1D transient elastography is commercially available as the Fibroscan® and has been validated for the characterization of cirrhosis (209).

Point shear wave elastography and 2D shear wave elastography, in contrast, make use of ARFIs to create tissue deformation (183, 210, 211). In these techniques, ARFIs are directed into the underlying tissue, which are absorbed and generate perpendicularly-directed shear waves (212). These shear waves cause displacement of the tissues as they propagate and, again, by using an ultra-high frame rate scanner, the resulting wave speed within the tissue can be measured (for example, using a speckle-tracking algorithm). The wave speed can then be used to estimate the Young's modulus (212). Point shear wave elastography relies on the interrogation of a single focal zone to estimate wave speed (213). 2D shear wave imaging (also called supersonic shear imaging), in contrast, makes use of multiple ARFIs to generate a cylindrical shear wave cone (called a Mach cone), which is interrogated rapidly over multiple focal zones (210). This allows for the real time generation of quantitative elastograms, which can be superimposed over the corresponding B-mode images (180). The major advantage of these techniques is that they are quantitative. However, these techniques tend to have limited penetration and they also may be less robust when imaging deep, heterogenous, and/or anisotropic tissues (30-32, 188).

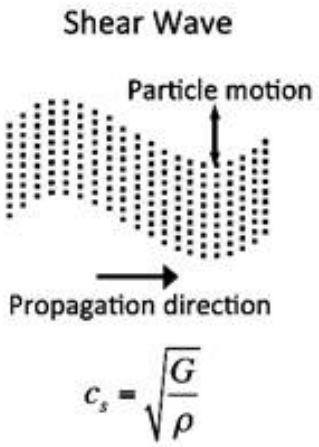

Figure 24 Shear wave imaging relies on the generation of shear waves. In shear waves, the particle motion is perpendicular to the direction of travel of the wave. The shear wave speed can be calculated to give an estimate of the shear modulus, which can be converted the elastic modulus via Poisson's ratio. c_s = wave speed; G = shear modulus; ρ = tissue density. Adapted from (180).

5.4 Quasi-static Elastography in Vessels: Non-invasive Vascular Elastography using a Lagrangian Speckle Model Estimator

Vascular elastography is a subset of elastography concerned with the mechanical properties of the vascular system. It has gained particularly interest in the assessment of the carotid and coronary arteries (214). Intravascular, catheter-based elastography is a common technique described in the literature (215-217); however, it is invasive and may not be suitable for routine screening or surveillance. Furthermore, factors such as catheter eccentricity, catheter movement within the vessel, and vessel asymmetry may result in signal decorrelation (23, 218). Thus, non-invasive forms of vascular elastography have been developed, employing both strain and shear techniques (219-221) One particular example of vascular elastography that employs QSUE has been entitled NIVE (non-invasive vascular elastography) (23).

NIVE using QSUE utilizes physiological stresses to generate tissue deformations within vascular tissue (23, 218). Algorithms for NIVE must address to two key problems: the complexity of vessel motion and the heterogeneity of the tissue. As previously described, most forms of SUE calculate strain based on a normally applied stress. However, in a vessel that is imaged transaxially, the stress is directed radially, being parallel to the ultrasound beam at only 0° and 180°. Furthermore, vascular tissue is inherently heterogeneous and may contain areas of thrombus, plaque, calcification, and lipid. These various regions may respond non-uniformly to the applied stress and have complex tissue deformations. Thus, one-dimensional correlation

techniques may be considered insufficient (23, 218). The Lagrangian speckle model estimator (LSME) was developed to respond to these limitations (24).

The LSME uses speckle motion to aid in elastographic analysis (23). As previously described, the speckle pattern of a tissue on ultrasonography is related to its inherent microstructure (133). With compression, changes in speckle pattern may be secondary to the movement of the speckles or changes in their morphology. If the local speckle field is considered to be a continuum of the material's mechanical property and (for small movements) the acoustic characteristics of the speckles are considered stable, then a Lagrangian description of movement can be applied. In this system, each speckle acts as its own coordinate system and its position is described as a function of time (24, 222). To apply this, a given region of interest is divided into small windows, in which motion is presumed to be affine (222). Speckle motion within each window is tracked using an optical flow algorithm, and displacement between frames is calculated from the Taylor series expansion (23). This generates a 2-D strain tensor as well as displacement maps between consecutive serial frames, which contain the strain and shear parameters (24, 198, 222). NIVE using LSME has been successfully utilized to discriminate vulnerable atherosclerotic plaques in the carotid arteries (198). Given the confusion of terms within the literature, SUE ultrasound elastography will be used as a general term to describe this technique in the remainder of the mémoire.

5.5 Elastography in the Context of EVAR

AAA diameter and growth rate are two of the most commonly used imaging parameters to guide management in patients post-EVAR; however, they are somewhat crude and do not identify all patients that are at risk for complications (88, 223, 224) Recently, the mechanical properties of aneurysm/endoleak constituents have been investigated for their ability to provide information regarding sac stability and evolution. After a successful EVAR procedure, blood that is trapped between the stent and the aortic wall eventually coagulates to form thrombus (in the absence of endoleak); however, it does not necessarily evolve into organized thrombus. In fact, there may be a mixture of fresh and organized thrombus within the aneurysm sac for years after EVAR (26). Fresh thrombus is unstructured and tends to be less stiff than organized thrombus (28, 30, 31). Speelman et al found that for a given thrombus volume in an idealized AAA model, intraluminal thrombi (ILTs) with greater shear moduli (which is proportional to the elastic modulus in soft tissue) tended to decrease wall stress to a greater extent than those with lower shear moduli (27). Furthermore, the accumulation of fresh thrombus may account for aneurysm non-shrinkage aneurysm or endotension (type V endoleaks), which may require subsequent intervention (26). Therefore, the in vivo characterization of the mechanical properties of AAA content post-EVAR may be useful in guiding management.

Elastography is well suited for this task. Both SUE and SWE have been used to characterize the constituents of aneurysms. In a canine preclinical model, SUE showed significant differences in the strain values between endoleaks, fresh thrombus, and organized thrombus (28). Of note, endoleaks tended to have the highest strain values because of signal decorrelation due to slow blood flow and the high deformations associated with the presence of immature thrombus (28, 29). Interestingly, this study found no difference in the mechanical properties of type I and type II endoleaks and that there was no correlation between sac pressure and the measured strain parameters. SWI has also been shown to be able to detect endoleaks, distinguish fresh from organized thrombus, characterize embolic agents, and demonstrate a trend towards increased thrombus organization over time after EVAR in preclinical studies (30, 31). Given the importance of both occlusivity and sac stiffness in preventing recanalization and adverse outcomes, the in vivo characterization of the mechanical properties of aneurysm sacs post-embolization with novel agents, such as CH-STS, are of clinical interest. This could be readily achieved using a penetrating and robust technique such as SUE.

Part II – Strain Ultrasound Elastography of Aneurysm Sac Content after Randomized Endoleak Embolization with Sclerosing and Non-sclerosing Chitosan-based Hydrogels in a Preclinical Model

Chapter 6 – Objectives and Hypotheses

6.1 Objectives

Endoleak embolization using CH-STS is associated with a decrease in the persistence of endoleaks compared to embolization with a non-sclerosing chitosan hydrogel embolic agent (CH) (43). In addition to its ability to remove the endothelial layer, the success of CH-STS is suspected to be mediated by its favorable mechanical and biomechanical properties, which are thought to promote occlusivity and prevent recanalization (42). Stiffer intraluminal contents also better decrease wall stress (27), which may theoretically reduce the risk of catastrophic complications. In short-term in vitro studies, CH-STS has demonstrated stiffer mechanical properties than CH. However, the behavior of these agents in vivo over an extended time course merits further characterization. This would be readily achieved with SUE. The specific objectives of the present in vivo investigation are to use SUE to:

1) Compare the mechanical properties of CH-STS and CH after embolization.
2) Compare the mechanical properties of the ILTs generated by embolization with CH-STS and CH.
3) Compare the mechanical properties of CH and CH-STS with the generated ILTs.
4) Compare the effect of CH-STS and CH embolization on the mechanical properties of the overall aneurysm sac contents over time.
5) Determine whether measurements of the mechanical properties of the above regions (embolic agent, ILT, aneurysm sac,) obtained using segmentations from two independent readers show favorable inter-observer reliability.

6.2 Hypotheses

1) CH-STS embolic agent will demonstrate stiffer mechanical properties than CH in vivo.
2) There will be no difference detected in the mechanical properties of the ILT generated by either embolic agent.
3) CH-STS will be stiffer than the ILT. CH will be less stiff than the ILT.
4) The aneurysm sacs of endoleaks embolized CH-STS with demonstrate better mechanical properties than those embolized with CH; this effect will persist over time.
5) The obtained measurements of mechanical properties will share favorable inter-observer reliability.

Chapter 7 – Methodology

7.1 Timeline and Ethical Considerations

The study data were acquired prospectively. Image analysis was performed between 2017-2019. All protocols were approved by the institutional animal care committee at the CRCHUM in accordance with Canadian Council of Animal Care guidelines.

7.2 Preclinical Canine Aneurysm and Endoleak Model

Bilateral iliac artery aneurysms with a surgically implanted outflow vessel were created in nine female mongrel dogs according to a previously described technique by a vascular surgeon (IS) with over twenty years of experience (40, 171). The procedure will be briefly summarized. The surgery was performed under general anesthesia using sterile technique. First, a lateral neck incision was performed to harvest one of the external jugular veins, which was conserved in heparinized solution. Then, a low-midline laparotomy was performed to expose and mobilize the common iliac arteries and the sacroiliac trunks. The proximal and distal aspects of one common iliac vessel were cross-clamped and a longitudinal arteriotomy was performed. A branch of the sacroiliac trunk was then identified, transected, and its distal end was anastomosed to the arteriotomy lip to create the outflow vessel. A 45 mm patch was cut from the harvested external jugular vein and sutured over the arteriotomy to simulate aneurysm dilatation. This was then repeated on the contralateral common iliac artery. The incisions were closed. Post-operatively, the animals received analgesia.

EVAR was performed eight weeks post-operatively by an interventional radiologist with over 20 years of experience (GS). Under fluoroscopic guidance, a 59-mm-long balloon-expandable stent-graft (iCAST; Atrium, Hudson, USA) was deployed in each aneurysm to a diameter of 7 or 8 mm, depending on the size of the proximal landing zone. Type Ia endoleaks were created by inflating a 3.5 mm balloon (Savvy; Cordis, Warren, New Jersey) in the proximal landing zone between the stent-graft and the wall to create a plastic deformation of the stent-graft. Of note, high flow type Ia endoleaks were created—as opposed to type II endoleaks—as they tended to create larger, more challenging endoleaks (171). The presence of an endoleak was confirmed with percutaneous angiography (Koordinat 3D II; Siemens Healthcare, Erlangen, Germany) using 20 mL of Isovue® 200 injected at 10 mL/s (Bracco Diagnostic, Anjou, Canada). Animals received aspirin 80 mg per day starting from the day of procedure until sacrifice. See **Figure 25** for a schematic of the experimental set-up.

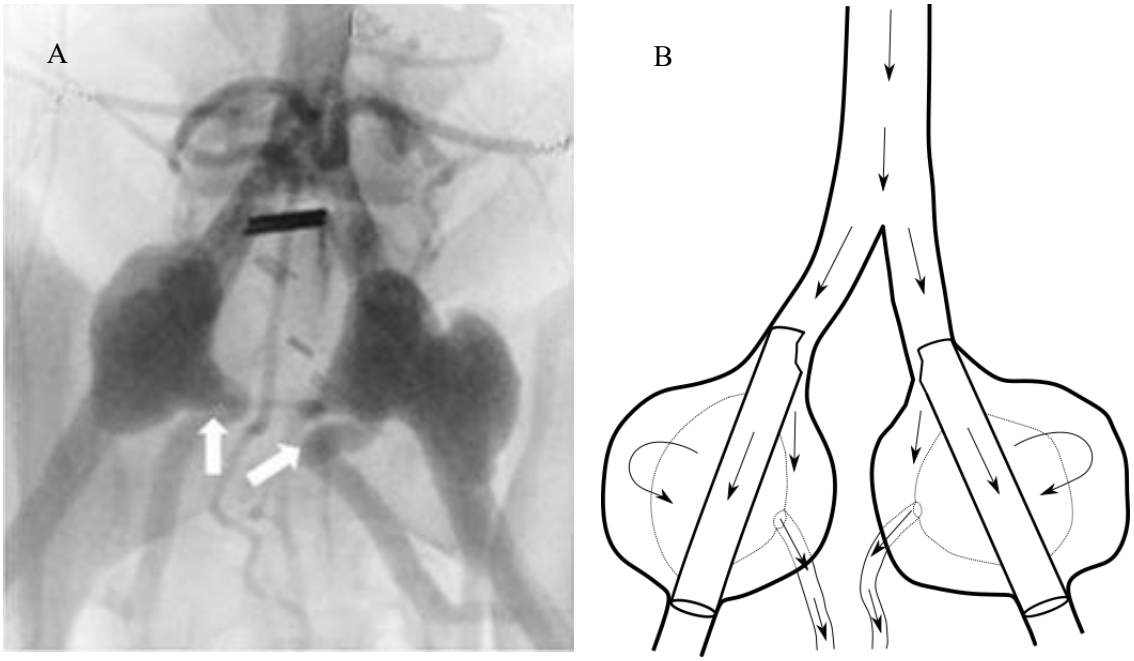

Figure 25 Bilateral iliac aneurysm model for testing of embolic agents. (A) Contrast-enhanced fluoroscopic image demonstrating the surgically created bilateral iliac artery aneurysm model. The arrows point to the implanted outflow tracts. (B) Schematic of the same model status post bilateral endovascular aneurysm repair and creation of type Ia endoleaks. Figures adapted from/with reference to (40, 43, 170, 171).

7.3 Preparation of Agents and Endoleak Embolization

CH-STS and CH were prepared according to previously described techniques (42, 43, 177); this will be briefly summarized. For CH-STS, chitosan (Marinard Biotech; Rivière-au-Renard, Canada) was dissolved in a solution of hydrochloric acid (0.1 M), deionized water, and Visipaque^{TM} 320 (GE Healthcare, Rahway, New Jersey). The solution was mixed for 24 hours and then sterilized using an autoclave. A second solution containing β-glycerophosphate disodium hydrate (BGP; Sigma Aldrich, Oakville, Canada) and STS (Sigma Aldrich, Oakville, Canada) was prepared and sterilized using a 0.2 μm filter. Immediately prior to embolization, the two solutions were mixed using two syringes and a luer lock connector, with a volume ratio of 3/2. The final concentration of the constituents of CH-STS were as follows: chitosan 2% weight/volume, Visipaque^{TM} 320 30% volume/volume, BGP 12% weight/volume, and STS 3% weight/volume. CH was prepared in a similar fashion with the following exceptions: the final concentration of BGP was 20% weight/volume and there was no STS included.

In each animal, one iliac aneurysm was randomly assigned to be embolized with CH and the other was assigned to be embolized with CH-STS. Prior to each paired embolization, the embolic agents were prepared by the biomedical engineer, randomly coded as “1” or “2”, and then inserted into an appropriately labelled

envelope. The envelopes were then provided to the interventional radiologist, who independently selected one aneurysm to be embolized with "1" and the other to be embolized with "2"; thus, the interventional radiologist was blinded to the type of gel used. Transarterial embolization was performed through a 4 French catheter (Glidecath; Terumo, Tokyo, Japan) that was inserted into the aneurysm sac through a contralateral puncture before stent-graft deployment. Following stent-graft deployment and creation of the type I endoleak, 3-5 mL of gel was injected under fluoroscopic guidance (Koordinat 3D II; Siemens Healthcare, Erlangen, Germany) with a balloon inflated at the level of the proximal common iliac artery to temporarily occlude blood flow. The embolization endpoint was occlusion of the aneurysm sac and the origin of the outflow vessel. The side embolized by each coded agent was recorded. The numbers corresponding to each agent were decoded only at the termination of the experiment to determine which side was embolized with which agent.

7.4 Imaging Follow-up and Sacrifice

Six of the animals were followed with imaging for a total of three months before sacrifice and three of the animals were followed with imaging for a total of six months before sacrifice in the context of another experiment (43). The timing of follow-up for each modality is described below and summarized in **Figure 26**.

7.4.1 Ultrasound Imaging: Parameters and Follow-up Timeline

Static B-mode images, DUS images, and RF cine acquisitions for SUE were obtained at one week, one month, and three months post-embolization in all nine animals; additional acquisitions were obtained at six months in three of the animals who were sacrificed at that time. Static B-mode and DUS images were obtained using the SuperLinear^{TM} 256 element SL15-4 7.5 MHz transducer (Aixplorer, Aix-en-Provence, France). Static B-mode images were used to assess sac morphology (including aneurysm size and stent-graft position) to aid in the image coregistration with other modalities. DUS was used to identify endoleaks and evaluate stent-graft patency. The following parameters were used: scale to 10 cm/s, smoothing to 0, wall filter to low, high-definition frame rate to middle, and steer angle to 0°, 60° right anterior oblique, and 60° left anterior oblique. RF acquisitions for SUE were obtained using the Sonix Touch^{TM} 128-element L14-5/38 10 MHz transducer (Ultrasonix Medical Corporation; Vancouver, Canada). The transducer has a frame rate of 25 Hz and a bandwidth of 60%. RF acquisitions were sampled at 40 MHz for approximately 4 seconds at each level.

7.4.2 CT Imaging

CT angiograms were obtained with the SOMATOM Sensation 64 (Siemens Medical; Forcheim, Germany) using 60 mL of Omnipaque^{TM} 300 (GE Healthcare; Mississauga, Canada) injected at 4 mL/s. CTs were obtained at three months for all animals and at six months for the three of the animals that were sacrificed at that time. The studies were prospectively gated and reconstructions of 10 images/cycle were obtained during the diastolic phase. Acquisition parameters were as follows: voltage 120 kVp, current 724 mA, pitch 0.2 mm, and collimation 0.6 mm.

7.4.3 Sacrifice, Macroscopy and Histopathological Analysis

Six of the subjects were sacrificed at three months and the remaining subjects were sacrificed at six months. The subjects were sacrificed with intravenous pentobarbital sodium (108 mg/kg; Bimeda-MTC Animal Health Inc., Cambridge, Canada). After sacrifice, the common iliac aneurysms were harvested en bloc and fixated in buffered formalin. Serial axial macroscopic sections of the aneurysms were produced using a cutting-grinding system (EXAKT Advanced Technologies GmbH, Norderstedt, Germany), which were then photographed for macroscopic analysis. Histological correlation was performed on conventional slides obtained after stent graft removal and paraffin embedding.

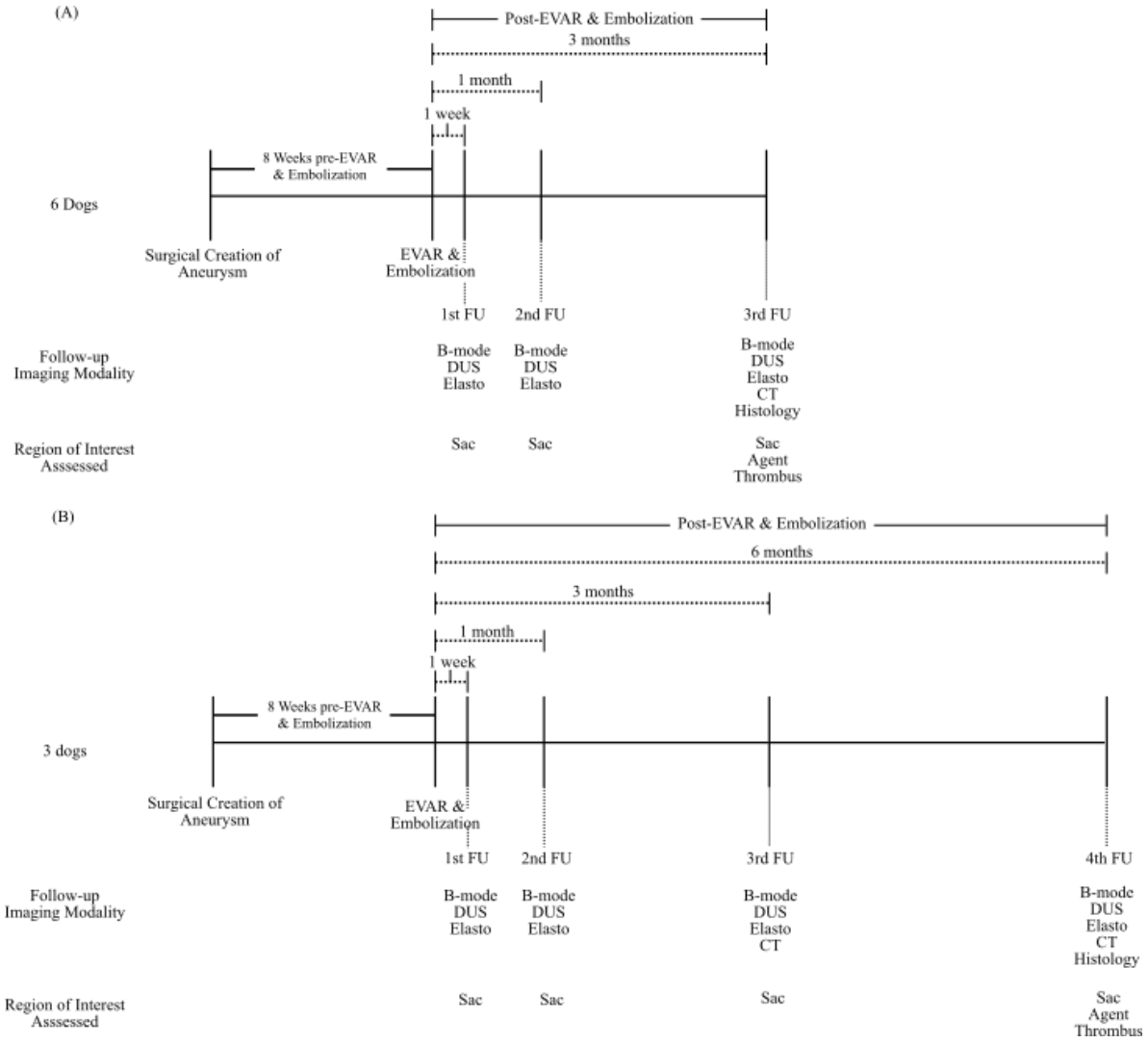

Figure 26 Procedural and imaging follow-up timeline. Surgical aneurysm creation was undertaken eight weeks prior to EVAR and endoleak creation. Embolization was performed on the same day as EVAR. (A) Six of the subjects were followed with imaging for three months after EVAR before sacrifice and histopathological analysis. Ultrasound-based acquisitions were obtained at all follow-up times (one week, one month, and three months); CT images were obtained at sacrifice. (B) Three of the subjects were followed with imaging for six months after EVAR before sacrifice and histopathological analysis. US-based acquisitions were obtained at all follow-up times (one week, one month, three months, and six months); CT was performed at three and six months. For both groups, all ultrasound-based acquisitions were obtained of the proximal, middle, and distal aneurysm sac. The aneurysm sac region of interest was segmented at all follow-up time points; the thrombus and embolic agent were only segmented at sacrifice. B-Mode: brightness mode ultrasound; CT: Computed tomography; DUS: Duplex ultrasound; Elasto: ultrasound cine loops for strain elastography; EVAR: endovascular aneurysm repair; FU: follow-up.

7.5 Elastographic Analysis

7.5.1 Defining Regions of Interest

The mechanical properties of three regions of interest (ROIs) were assessed:

1. Embolic agent. The embolic agent ROI refers to the region of the sac that contains either CH or CH-STS. Previously published data suggests that the embolic agent remains largely distinct from the associated ILT on histopathological analysis (43). Given the relative homogeneity of the agent in vivo, the ROI was only segmented at the level where it was best visualized (either proximal, middle, or distal aneurysm). This ROI was only segmented on the studies at the time of sacrifice as it required macroscopic and histopathological correlation to distinguish it reliably from the ILT.
2. ILT. This ROI was also only segmented at sacrifice using the level where it was best visualized, as it required macroscopic and histopathological correlation to distinguish it reliably from the embolic agent.
3. Aneurysm sac. The aneurysm sac ROI includes both the embolic agent and the ILT, corresponding to the entire aneurysm sac contents excluding the stent-graft and any endoleak. This region of interest was defined as a surrogate for the overall mechanical properties of the aneurysm. Clinically, this ROI would be useful for follow-up after post-embolization because of the poor contrast between thrombus and embolic agent on B-mode imaging. To account for the heterogeneity of the composition of this ROI throughout the aneurysm sac, the mechanical properties for all three levels (proximal, middle, and distal) of the aneurysm sac were measured. These measurements were performed at each imaging follow-up until sacrifice.

The imaging and histopathological characteristics of each of these regions of interest are outlined in **Table 3**.

7.5.2 Display of RF Data for Elastography and Image Co-registration

The raw RF acquisitions obtained of the proximal, middle, and distal sac of each aneurysm at each time point were imported to a third-party imaging platform (ORS Visual, Object Research Systems, Montreal, Canada) and were displayed as B-mode cines. The B-mode cines were then coregistered with the relevant static B-mode images, DUS images, CT studies, and histopathological studies at all applicable follow-up time points to help identify the various ROIs. Co-registration was based on the level of acquisition, the aneurysm size, and the relative position of the stent-graft in the aneurysm. See **Figure 27** for an example**.**

Region	B-mode/DUS	CT	Macroscopy	Microscopy
Embolic agent (CH or CH-STS)*	Hyperechoic to thrombus	Indistinguishable from thrombus†	Yellow-brown, homogenous, friable material	Red/purple material lacking cellular content or tissular organization
Thrombus*	Hypoechoic to embolic agent	Indistinguishable from embolic agent†	Organized: Dense yellow, organized tissue. Fresh: Dark blue, unorganized tissue.	Organized: Layered network of fibrin. Fresh: Free, unstructured erythrocytes
Aneurysm sac‡	Entire aneurysm content minus endoleak and stent-graft			
Endoleak¶	Mobile echoes on B-mode cine. Doppler signal on DUS.	Contrast enhancement within the aneurysm but outside of the stent-graft	Defect within the aneurysm sac	Defect within the aneurysm sac
Stent-graft	Hyperechoic ring	Hyperdense ring	Self-evident	Removed for histological processing

Table 3 Brightness mode (B-mode), Duplex ultrasound (DUS), CT (computed tomography), and histopathological appearance of various regions of interest (ROIs) to be characterized by strain ultrasound elastography (agent, thrombus, and aneurysm sac), as well as other ROIs used to help delineate them (endoleak and stent-graft). * Measured at the most representative level per aneurysm. † CH (CH hydrogel embolic agent) and CH-STS (chitosan hydrogel embolic agent with STS) are radiopaque given that they contain Visipaque™ (for visibility under fluoroscopy); however, their radiopacity lasts for only 48 hours (225). ‡The aneurysm sac mechanical properties represent sac stability. To account for the heterogeneity of the composition of the aneurysm sac, the mechanical properties for three levels of the sac (proximal, middle, and distal) were measured. ¶ Endoleaks were not assessed as an ROI using elastography because they had already been characterized as regions of high deformation caused by the heterogeneous effects of signal decorrelation due to slow blood flow and the presence of immature thrombus (28, 29).

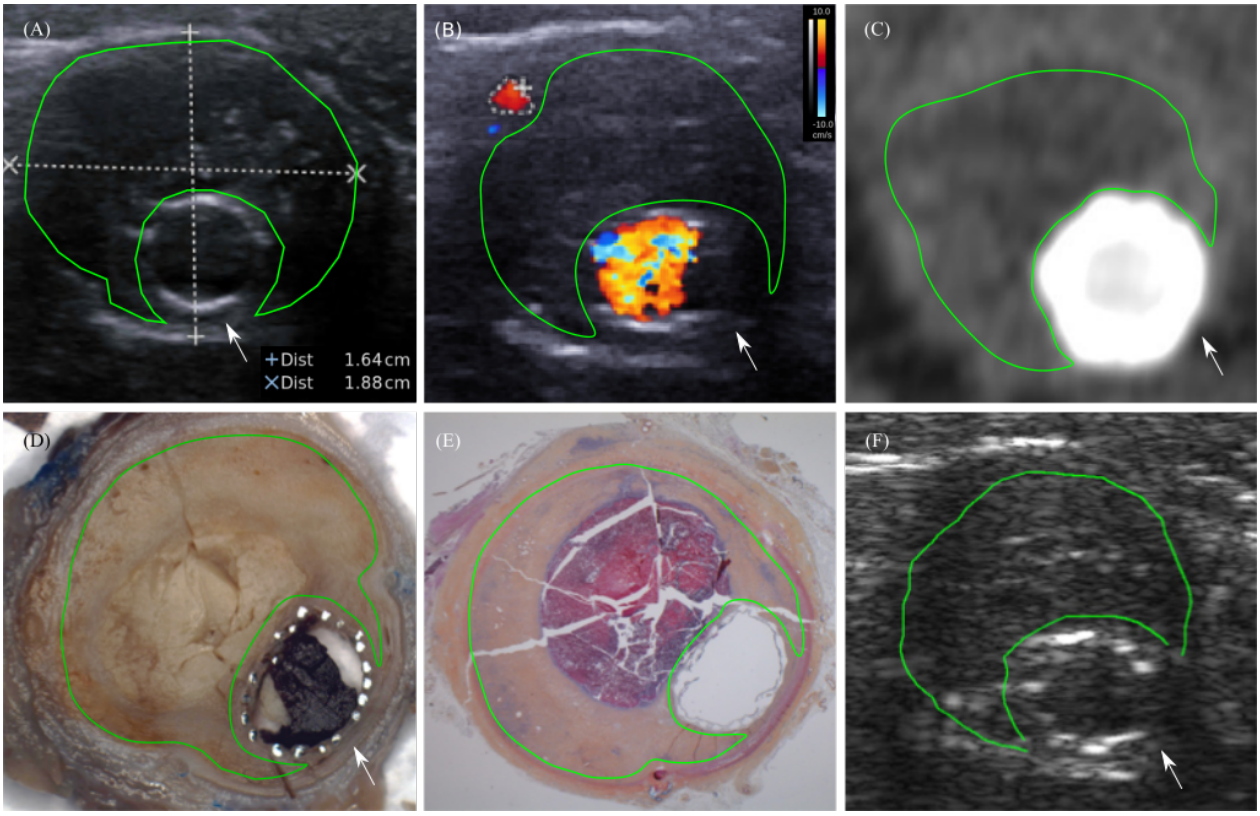

Figure 27 Multimodal image co-registration and segmentation at sacrifice of the mid-level aneurysm sac region of interest (segmented in green) for an endoleak three months post-embolization with the chitosan hydrogel embolic agent. The arrows indicate the stent-graft. (A) Selected B-mode image of the mid level of the aneurysm demonstrates the segmentation of the entire aneurysm sac. Note that the stent-graft was excluded. (B) Corresponding duplex ultrasound image suspected to have been taken at a slightly more caudal location, where an endoleak is visualized. Note that it has been excluded from the segmentation. (C) Contrast-enhanced CT examination of the aneurysm sac at the same level of (A) and the other remaining images. Note that an endoleak was not identified at this level, but was identified a few slices lower, suggesting that the image in (B) was more caudal. (D) and (E) Macroscopic cut and histopathological slide of the mid-level of the aneurysm; note that no endoleak is visible on these levels; an endoleak was confirmed more inferiorly (not shown). (F) Selected segmented B-mode image from the obtained cine loop used to produce the elastograms. Part of the aneurysm sac was not included because there was potentially an endoleak in this region; this was done to avoid the high strains associated with signal decorrelation. The segmentation mask was propagated through the remainder of the cine loop using a semiautomatic technique. Appropriate segmentation requires the integration of all of the imaging modalities.

7.5.3 Static Ultrasound Elastography of the Regions of Interest

SUE (via the LSME) was implemented in ORS Visual. The regions of interest defined in **Section 7.5.1** were manually segmented on the first frame of the B-mode cine loops by two independent readers (LS [radiology trainee] and GS [radiologist with 20 years' experience]) with reference to the co-registered studies (see **Section 7.5.2**). 39 ROIs were used to train the junior interpreter; these were resegmented by the junior interpreter one year later. Observers were blinded to the type of embolic agent used in each aneurysm. The segmentation curves were propagated to the remainder of the frames of the B-mode cine using a semi-automatic technique (226). Instantaneous strain and shear values between frames were calculated with the LSME using computational windows measuring 80 x 20 pixels (height x width). Their averaged value over the segmented area was then plotted over time. In the post-processing phase, performed by LS, the axial strain and shear curves were divided into cardiac cycles to generate three elastography parameters: maximum axial strain (main outcome), range cumulative axial strain, and range cumulative axial shear. Please see **Figures 28-31** for examples of the post-processing technique. Please see **Table 4** for the derivation of each of the parameters.

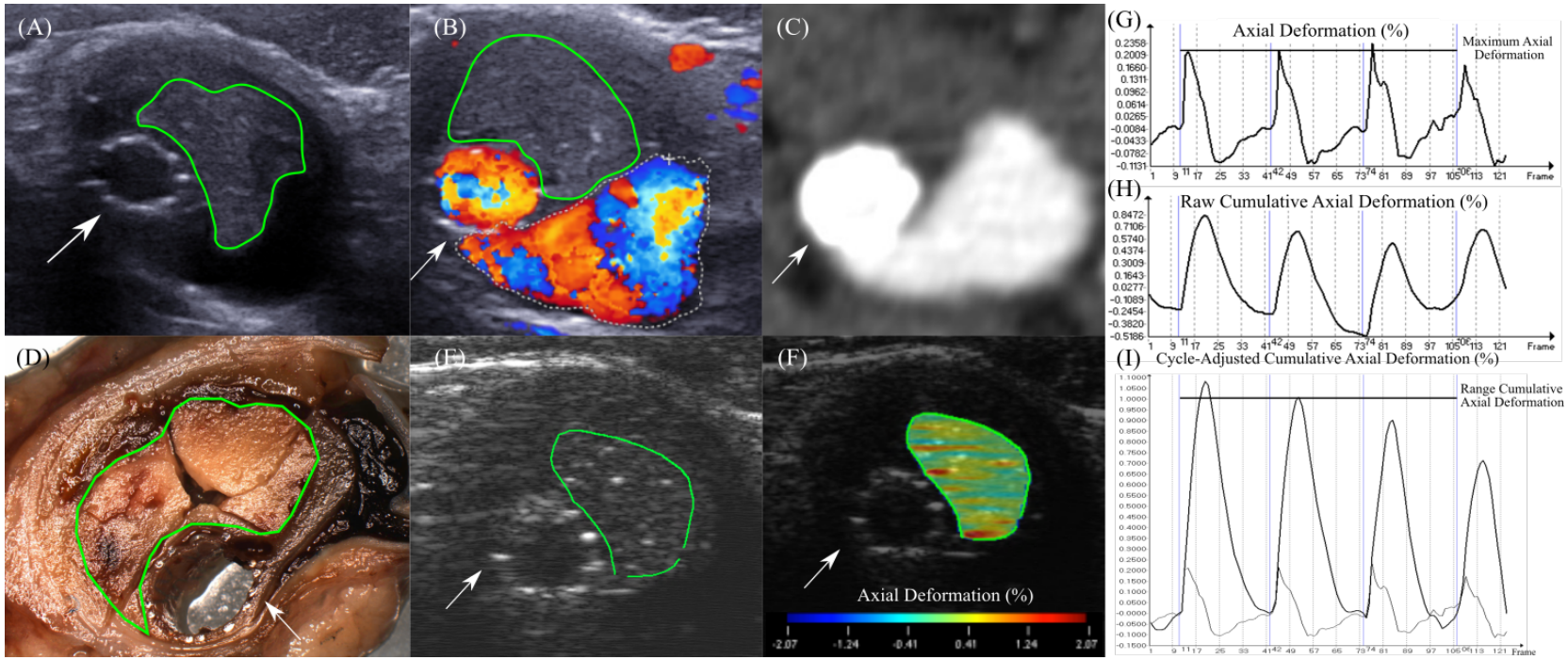

Figure 28 Multimodal image co-registration, segmentation, and post-processing of the embolic agent region of interest (segmented in green) for an endoleak three months post-embolization with the chitosan hydrogel embolic agent (CH) at sacrifice. (A) B-mode image of the mid level of the aneurysm demonstrates the segmentation of the embolic agent, which is slightly hyperechoic and heterogenous. (B) Duplex ultrasound image. Note that the endoleak has been excluded. (C) Contrast-enhanced CT examination. Note that the embolic agent and thrombus cannot be differentiated (the former's radiopacity is lost after 48 hours). (D) Macroscopic cut demonstrating the embolic agent. (E) Selected segmented B-mode image from the cine loop used to produce the elastogram. The segmentation mask was propagated through the remainder of the cine loop using a semiautomatic technique. (F) Instantaneous axial deformation elastogram of the embolic agent superimposed over a cine frame during systole. (G) Instantaneous axial deformation curve; the maximum axial deformation parameter (average of all peaks) is labelled. (H) Raw cumulative axial deformation curve. (I) Cycle-adjusted cumulative axial deformation curve adjusted for the cardiac cycle (thicker curve; the thinner curve is the axial deformation curve). The range cumulative axial deformation parameter is labelled. Some of these images have been included in (31, 43).

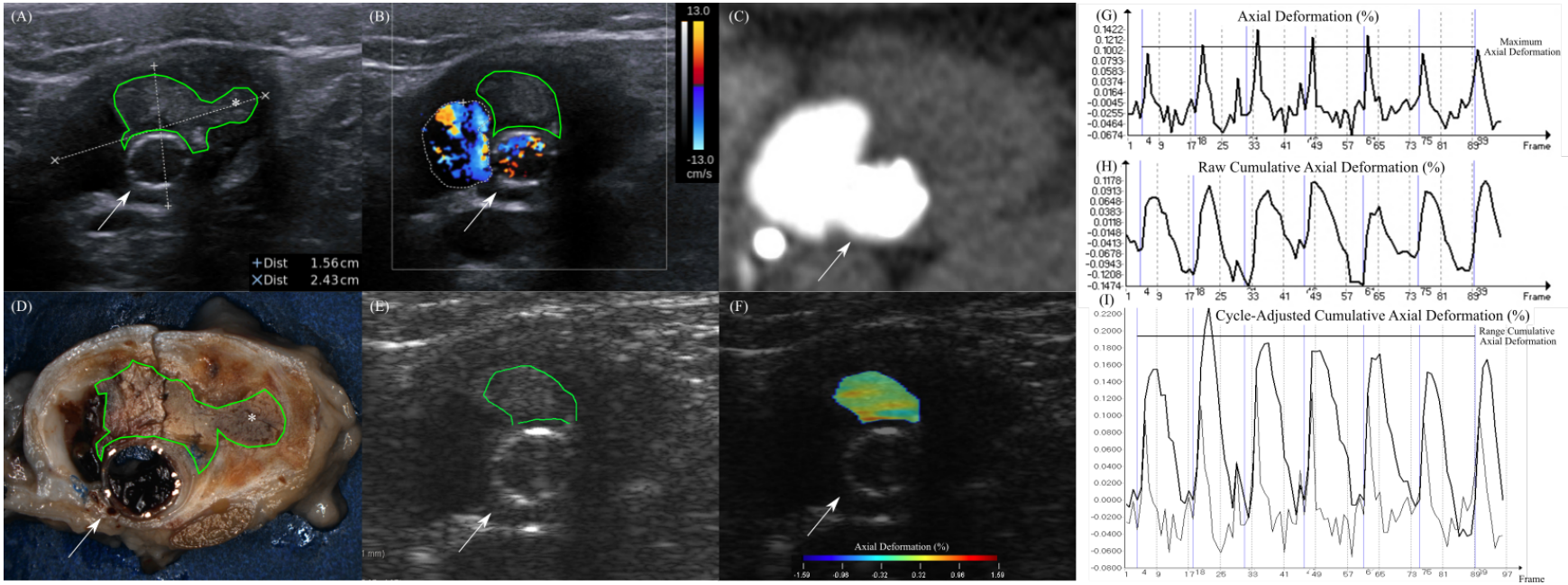

Figure 29 Multimodal image co-registration, segmentation, and post-processing of the agent region of interest (segmented in green) for an aneurysm three months after embolization with the chitosan hydrogel with sodium tetradecyl sulphate embolic agent (CH-STS) at sacrifice. The arrows indicate the stent-graft. All images were taken at approximately the same level but were subject to operator variability. The region indicated by (*) did not have a correlate on the cine loop and was therefore not included in the final segmentation. (A) B-mode image of the mid level of the aneurysm. The embolic agent is slightly hyperechoic and heterogenous. (B) Corresponding segmented duplex ultrasound image demonstrating an endoleak. (C) Corresponding contrast-enhanced CT confirming an endoleak. (D) Corresponding macroscopic cut demonstrating the agent and the endoleak. (E) Selected segmented B-mode image from the cine loop used to produce the elastograms. This image was likely obtained at a slightly different level compared to (A) and (D), resulting in a slightly different-appearing segmentation mask. It was important to exclude the endoleak and intraluminal thrombus to have a homogenous region of interest. (F) Instantaneous axial deformation elastogram of CH-STS superimposed over a cine frame during systole. (G) Instantaneous axial deformation curve. The maximum axial deformation parameter is labelled. (H) Raw cumulative axial deformation curve. (I) Cycle-adjusted cumulative axial deformation curve (thicker curve; the thinner curve is the axial deformation curve). The range cumulative axial deformation parameter is labelled.

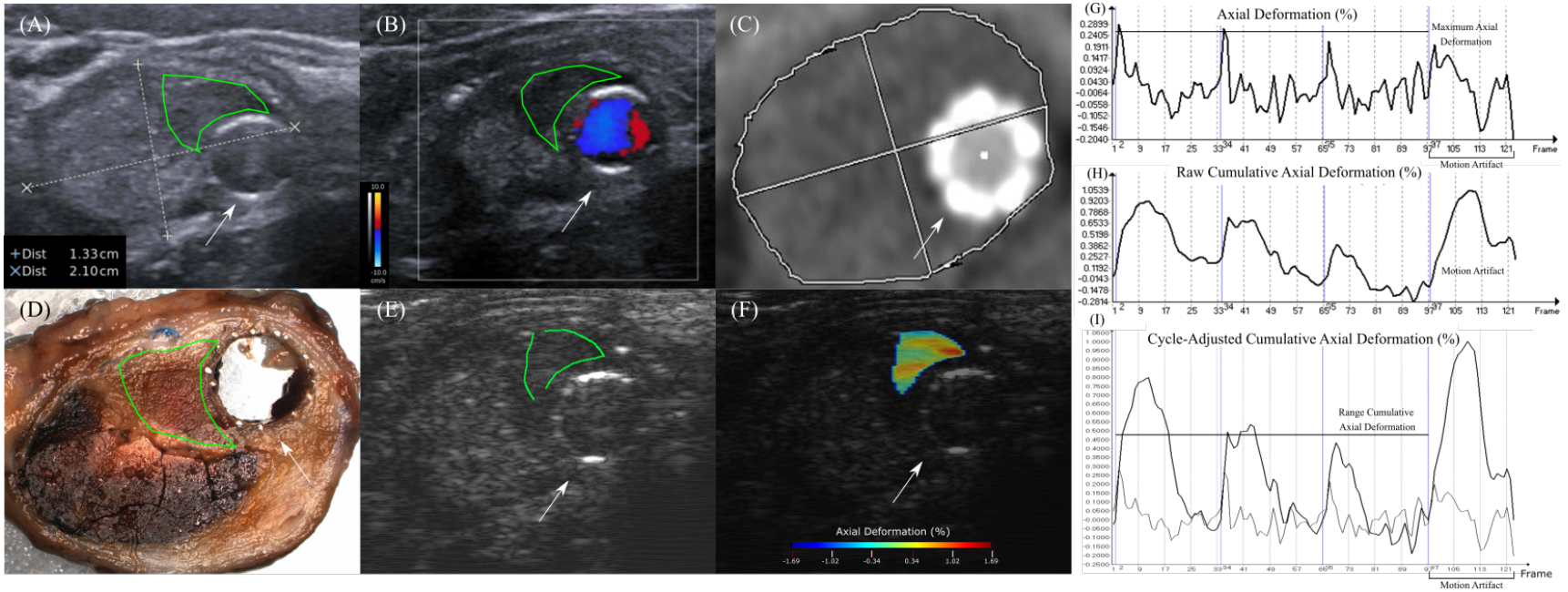

Figure 30 Multimodal image co-registration, segmentation, and post-processing of the thrombus region of interest (segmented in green) for an aneurysm three months post-embolization with the chitosan hydrogel with sodium tetradecyl sulphate embolic agent (CH-STS) at sacrifice. The arrows indicate the stent-graft. All images were taken at approximately the same level but were subject to operator variability. (A) B-mode image of the mid level of the aneurysm. The hyperechoic region corresponds to CH-STS and the hypoechoic regions correspond to thrombus. (B) Corresponding duplex ultrasound. (C) Corresponding contrast-enhanced CT image. (D) Corresponding macroscopic cut. (E) Selected segmented B-mode image from the cine loop used to produce the elastograms. (F) Cumulative axial deformation elastogram of the thrombus superimposed over a cine frame during systole. (G) Instantaneous axial deformation curve; the maximum axial deformation parameter is labelled. (H) Raw cumulative axial deformation curve. (I) The cycle-adjusted cumulative axial deformation curve (thicker curve; the thinner curve is the axial deformation curve). The range cumulative axial deformation parameter is labelled. Of note, only complete cardiac cycles without motion artifact (seen on the cine) were included in the post-processing.

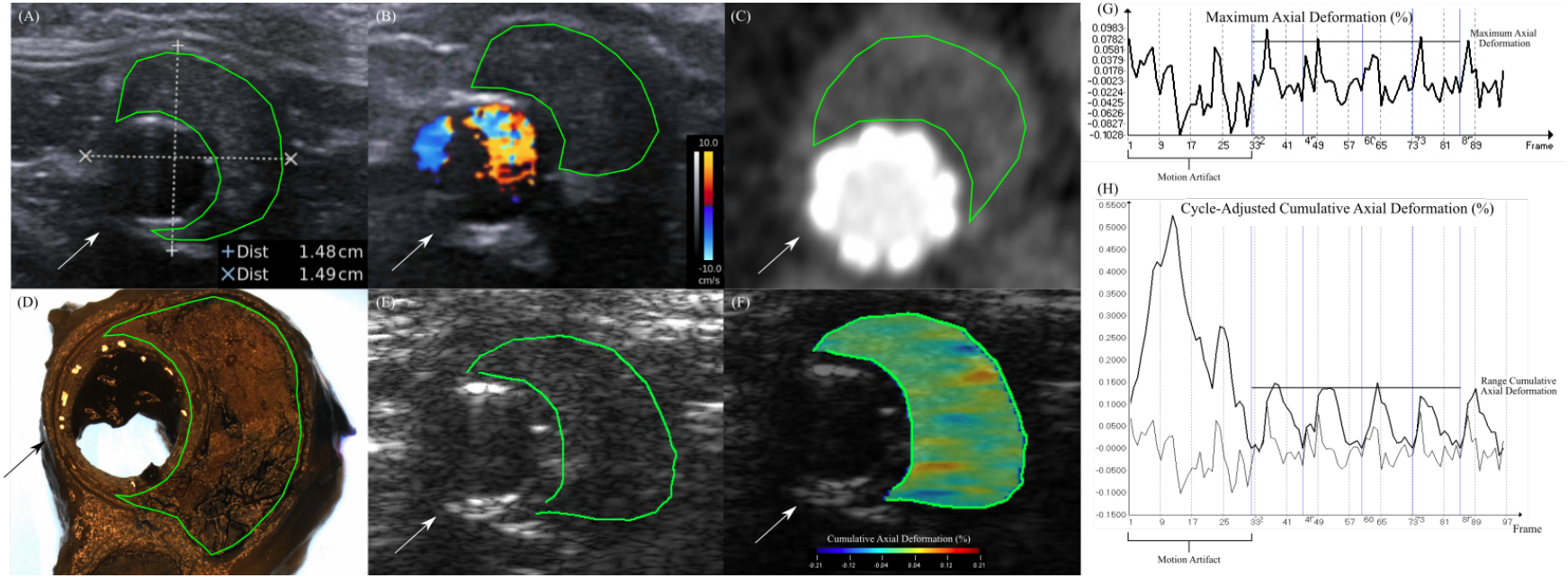

Figure 31 Multimodal image co-registration, segmentation, and post-processing of the aneurysm sac region of interest (segmented in green) for an aneurysm six months after successful embolization with the chitosan hydrogel embolic agent with sodium tetradecyl sulphate (CH-STS) at sacrifice. The arrows indicate the stent graft. (A) B-mode image of the distal level of the aneurysm demonstrates the segmentation of the sac. (B) Corresponding duplex ultrasound image; there is no endoleak to be excluded. (C) Corresponding contrast-enhanced CT image confirming the absence of endoleak. (D) Corresponding macroscopic cut. (E) Selected segmented B-mode image from the cine loop used to produce the elastograms. (F) Cumulative axial deformation elastogram of the sac superimposed over a cine frame during systole. (G) Instantaneous axial deformation curve; the maximum axial deformation parameter (average of all peaks) is labelled. (H) The cycle-adjusted cumulative axial deformation curve (thicker curve; the thinner curve is the axial deformation curve). The range cumulative axial deformation parameter is labelled. Note that frames containing motion artifact (seen on the cine loops) were excluded from the analysis.

Parameter	Derivation of parameter
Maximum axial deformation (%)	• This parameter is derived from the time-varying axial strain curve. • It is the average of the maximum strain value of the ROI during each cardiac cycle averaged across all cardiac cycles.
Range cumulative axial deformation (%)	• This parameter is derived from the time-varying cumulative axial strain curve. In this curve, each point corresponds to the sum of the previous average strain values of the ROI, which are reset at the beginning of each cardiac cycle. • To obtain this parameter, the range of the cumulative axial strain curve in each cardiac cycle is obtained and then averaged across the cardiac cycles.
Range cumulative axial shear (%)	• This parameter is derived from the time-varying cumulative axial shear curve. In this curve, each point corresponds to the sum of the previous average shear values of the ROI, which are reset at the beginning of each cardiac cycle. • To obtain this parameter, the range of the cumulative axial shear curve in each cardiac cycle is obtained and then averaged across the cardiac cycles.

Table 4 Derivation of the strain (deformation) and shear elastography parameters obtained using strain ultrasound elastography using a Lagrangian speckle model estimator. ROI: Region of interest.

7.6 Statistical Analysis

Statistical analysis was performed using R software (version 3.6.0; *R Foundation,* Vienna, Austria). Data generated from the segmentations performed by both readers are presented. Statistical analyses were performed on the outcomes obtained by reader GS' segmentations. The outcomes obtained by the segmentations performed by both GS' and LS' segmentations were used for inter-observer reliability assessment. Outcomes were log-transformed to produce better model fits. The level of significance for all comparisons was set at $\alpha = 0.05$. Multivariable linear mixed-effects models were used to model the mechanical properties of the agent and thrombus ROIs as well as to compare the mechanical properties of CH and CH-STS with those of the ILT. Multivariable linear mixed-effects models were also used to model the mechanical properties of the aneurysm sac ROI. The inter-observer reliability of the outcomes obtained by the two readers was calculated via intraclass correlation coefficients using a two-way random effects model for a single measure for consistency.

7.7 Relationship with Other Investigations and Original Contribution

In accordance with the guidelines of the Canadian Council on Animal Care—which mandates that the number of subjects used to test experimental hypotheses be minimized (227, 228)—a total of three studies were planned to be derived from the subjects included the present investigation. In the first study, Zehtabi et al optimized CH-STS and compared its effectiveness to CH for the treatment of endoleaks; the study included several of the subjects included in the present study (43). The second study, by Bertrand-Grenier et al, used SWI to characterize the mechanical properties of aneurysms after embolization with CH-STS and CH—using the same subjects as in the present study (with the exception of one)—with a similar imaging follow-up and coregistration paradigm as detailed in **Sections 7.4** and **7.5.2** (31). The present study, which represents the third of the three studies, characterizes the mechanical properties of the ROIs detailed in **Section 7.5**—again, using several of the same subjects in the prior two studies—but this time using SUE. Therefore, the study by Bertrand-Grenier et al and the present study could be viewed as complementary studies that use different techniques (SWI versus SUE) to characterize the in vivo mechanical properties of aneurysms after embolization with CH-STS and CH. The characterization of these ROIs via SUE is of relevance because it is thought to be a more penetrating and robust technique compared to SWI, and therefore may be better able to assess the mechanical properties of the intraluminal contents (30-32, 188); these differences will be expounded upon in the discussion section where appropriate. Since the present study represents one facet of a larger experimental investigation involving the subject cohort, and that it will be published third, it necessarily reincorporates data that have also been used in the aforementioned papers with respect to experimental model construction, agent preparation, non-strain related imaging acquisition, and histopathological preparation. As such, the contributions of the relevant authors of/contributors to the aforementioned papers have been noted in the **Acknowledgments** section of the mémoire; these individuals will also be included as co-authors or mentioned in the acknowledgments section in the submitted scientific article where appropriate. Additionally, individuals who have contributed exclusively to the present project have also been/will also be credited in a similar fashion.

Given the interrelatedness of the present investigation with the previously described studies, the originality of the present mémoire must be emphasized. In the present investigation, SUE analysis of the ROIs detailed in **Section 7.5** was performed on B-mode cine loop acquisitions of the proximal, middle, and distal aneurysm obtained at all follow-up times; these acquisitions were not analyzed in the studies by Bertrand et al and Zehtabi et al. As such, the resulting SUE analysis of these images has not been previously published in a scientific journal. Preliminary SUE results of the subjects in the present study were previously presented at conferences (229, 230); however, in the present study, the ROIs assessed at each of the follow-up time points were streamlined (and have actually evolved since the study by Bertrand-Grenier et al), more

reliable outcome parameters were selected, a completely revised segmentation protocol was implemented to improve accuracy (the previously described preliminary results were not suitable for publication), two new readers performed the segmentations with the revised technique to generate measures of reproducibility, the post-processing was re-performed, a formal statistical analysis was performed, and the results were reinterpreted. Therefore, all of the elastographic results and statistical analyses presented in this mémoire are unique and have not been presented or published previously. The results and discussion sections of this mémoire focus on the newly acquired data.

Finally, the role of the primary author of the mémoire must be emphasized. The author performed the background literature review. The author was responsible for all aspects of the project related to the SUE analysis of the cine loops and of the resultant interpretation. The author shared responsibility for the coding of the presence of residual endoleaks and identifying post-procedural complications. The author performed one of the two independent segmentations of the ROIs using the previously detailed coregistration technique. The author helped facilitate the independent segmentation of the ROIs by the other reader. The author was responsible for performing the post-processing of the segmentations to obtain the imaging parameters outlined in **Table 4**. The author shared responsibility for identifying the most relevant outcome parameters and collected the data from the post-processing software's output. The author performed preliminary analyses of the outcomes and was involved extensively in the designing of the statistical analysis plan (with the contribution of the study director and a statistician). The author either contributed to or created several of the figures included in the methods and results section. Finally, the author provided the interpretation of the outcomes, which are outlined in the discussion section.

Chapter 8 – Results

8.1 Baseline Characteristics

Surgical aneurysm construction, stent-graft deployment, and type Ia endoleak creation were successful in both iliac arteries of all nine canine subjects, creating a total of 18 paired type Ia endoleaks. Nine paired embolizations of CH and CH-STS were performed in each animal. Post-embolization, 7/9 (78%) of aneurysms embolized with CH had residual endoleaks while 4/9 (44%) of aneurysm embolized with CH-STS had residual endoleaks. There was one complication of stent-graft thrombosis in the CH group. This subject also had a residual endoleak, which may have prevented the development of lower extremity ischemia. Although stent-graft thrombosis may have entailed a loss of a primary internal deforming force, the subject was included in the final analysis.

RF cine acquisitions for SUE, static B-mode images, DUS images, CT examinations, and macro/microscopic images/slides were successfully obtained in both treatment groups and were successfully coregistered for all subjects. All anticipated ROIs on the B-mode cines were identified after image coregistration with one exception: one failed CH-STS embolization had no residual embolic agent remaining; thus, this ROI could not be identified. In total, 430 elastograms were generated, 215 from each reader. The following breakdown of elastograms is expressed per reader. For each treatment group, 90 total elastograms were generated each for the aneurysm sac ROI. Six of the animals had 9 observations for each aneurysm (three levels [proximal, middle, distal sac] at three follow-up time points [1 week, 1 month, 3 months]), while three of the animals had 12 observations for aneurysm (three levels at four follow-up time points [additional follow-up at 6 months]). Alternatively put, there were 27 observations per treatment group at each time point until 3 months, and there were 9 observations per treatment group at 6 months. There were 9 elastograms generated for each treatment group for the thrombus ROI per reader. There were 9 elastograms generated for the embolic agent ROI in the CH group per reader; there were only 8 elastograms generated for the embolic agent ROI in the CH-STS group per reader (one subject with failed embolization had no residual endoleak). See **Figure 32** for a summary of the elastograms generated.

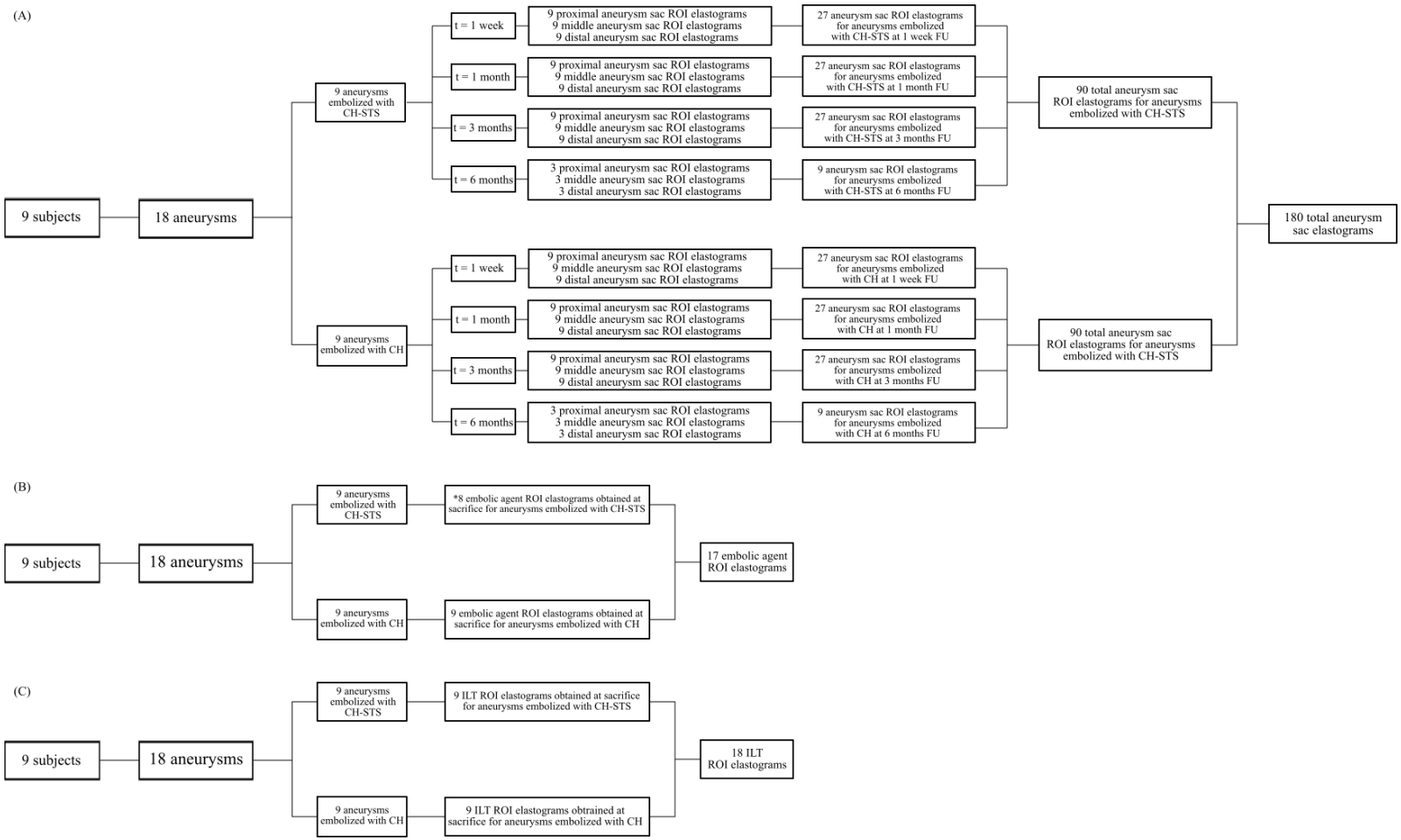

Figure 32 Breakdown of the elastograms generated using the segmentations independently performed by each reader. The elastograms contain the data used to derive the maximum axial deformation, range cumulative axial deformation, and the range cumulative axial shear. (A) Elastograms generated of the aneurysm sac ROI. (B) Elastograms generated of the embolic agent ROI. *One subject embolized with CH-STS did not have any residual embolic agent, thus this ROI could not be segmented for the subject. (C) Elastograms generated of the ILT ROI. CH: Chitosan hydrogel; CH-STS: Chitosan hydrogel with sodium tetradecyl sulphate; FU: follow-up; ILT: intraluminal thrombus; ROI: region of interest; t: time.

8.2 Elastograms of the Embolic Agent ROI

The means and standard deviations of the maximum axial deformation, range cumulative axial deformation, and range cumulative axial shear for the embolic agent ROI stratified by type of embolic agent used and presence of endoleak, as obtained from the GS and LS segmentations, are presented in **Table 5**. The multivariable linear mixed-effects model fitted to the outcomes obtained from the GS segmentations revealed that endoleak was not a clinically or statistically significant predictor and was removed from the final model. The final predictive model for the elastographic parameters stratified by agent used are presented in **Table 6**. CH-STS was associated with a 66% lower maximum axial deformation (95% confidence interval [CI]: -80% to -42%, $p < 0.001$) and a 67% lower range cumulative axial deformation (CI: -79% to -47%, $p < 0.001$) than CH. The range cumulative axial shears of the embolic agents were not significantly different between the two treatment groups.

(A)

Embolic agent	Endoleak Present	Maximum Axial Deformation (%)	Range Cumulative Axial Deformation (%)	Range Cumulative Axial Shear (%)
CH-STS	Yes (n=3)	0.111 ± 0.09	0.226 ± 0.098	0.759 ± 0.184
	No (n=5)	0.088 ± 0.082	0.188 ± 0.127	0.681 ± 0.210
CH	Yes (n=7)	0.224 ± 0.099	0.535 ± 0.280	0.855 ± 1.044
	No (n=2)	0.262 ± 0.056	0.691 ± 0.084	1.188 ± 0.934

(B)

Embolic agent	Endoleak Present	Maximum Axial Deformation (%)	Range Cumulative Axial Deformation (%)	Range Cumulative Axial Shear (%)
CH-STS	Yes (n=3)	0.093 ± 0.042	0.176 ± 0.058	0.745 ± 0.305
	No (n=5)	0.075 ± 0.070	0.138 ± 0.068	0.717 ± 0.205
CH	Yes (n=7)	0.171 ± 0.074	0.514 ± 0.297	0.911 ± 1.053
	No (n=2)	0.215 ± 0.017	0.633 ± 0.380	0.403 ± 0.108

Table 5 Mean (± standard deviation) of the maximum axial deformation, range cumulative axial deformation, and range cumulative axial shear of the embolic agent region of interest, at sacrifice, stratified by type of embolic agent used and presence of residual endoleak, as determined by (A) reader GS and (B) reader LS. CH: Chitosan hydrogel embolic agent; CH-STS: Chitosan hydrogel with sodium tetradecyl sulphate embolic agent; n: number of aneurysms.

Predictor	Maximum axial deformation			Range cumulative axial deformation			Range cumulative axial shear		
	Estimate	95% confidence interval	p-value	Estimate	95% confidence interval	p-value	Estimate	95% confidence interval	p-value
Intercept	0.22%	0.15% – 0.32%	**<0.001**	0.52%	0.37% – 0.73%	**<0.001**	0.65%	0.42% – 0.98%	**0.042**
Use of CH-STS	-66%	-80% – -42%	**<0.001**	-67%	-79% – -47%	**<0.001**	6%	-42% – 96%	0.845

Table 6 Multivariable linear mixed-effects model demonstrating the effect of use of CH-STS (versus CH) on the elastographic parameters of maximum axial deformation, range cumulative axial deformation, and range cumulative axial shear of the embolic agent region of interest obtained using the segmentations by reader GS. The estimate for the predictor CH-STS refers to the percentage change of the outcome parameter when CH-STS is used. CH: Chitosan hydrogel embolic agent. CH-STS: Chitosan hydrogel with sodium tetradecyl sulphate embolic agent.

8.3 Elastograms of the ILT ROI

The means and standard deviations for the maximum axial deformation, range cumulative axial deformation, and range cumulative axial shear for the ILT ROI stratified by type of embolic agent used and presence of endoleak—as obtained from the GS and LS segmentations—are presented in **Table 7**. The multivariable linear mixed-effects model fitted to the outcomes obtained from the GS segmentations revealed that neither the agent used nor presence of endoleak were significantly predictors of the outcomes (**Table 8**).

(A)

Embolic agent	Endoleak Present	Maximum Axial Deformation (%)	Range Cumulative Axial Deformation (%)	Range Cumulative Axial Shear (%)
CH-STS	Yes (n=4)	0.185 ± 0.108	0.380 ± 0.192	0.865 ± 0.793
	No (n=5)	0.126 ± 0.053	0.288 ± 0.164	0.458 ± 0.236
CH	Yes (n=7)	0.155 ± 0.076	0.366 ± 0.152	0.671 ± 0.419
	No (n=2)	0.133 ± 0.018	0.284 ± 0.069	0.462 ± 0.411

(B)

Embolic agent	Endoleak Present	Maximum Axial Deformation (%)	Range Cumulative Axial Deformation (%)	Range Cumulative Axial Shear (%)
CH-STS	Yes (n=4)	0.222 ± 0.136	0.470 ± 0.296	0.723 ± 0.199
	No (n=5)	0.112 ± 0.060	0.291 ± 0.149	0.672 ± 0.269
CH	Yes (n=7)	0.153 ± 0.055	0.308 ± 0.112	0.994 ± 0.614
	No (n=2)	0.135 ± 0.061	0.234 ± 0.061	0.527 ± 0.035

Table 7 Mean (± standard deviation) of the maximum axial deformation, range cumulative axial deformation, and range cumulative axial shear of the intraluminal thrombus region of interest stratified by type of embolic agent used and presence of endoleak at sacrifice as determined by (A) reader GS and (B) reader LS. CH: Chitosan hydrogel embolic agent. CH-STS: Chitosan hydrogel with sodium tetradecyl sulphate embolic agent.

Predictor	Maximum axial deformation			Range cumulative axial deformation			Range cumulative axial shear		
	Estimate	95% confidence interval	p-value	Estimate	95% confidence interval	p-value	Estimate	95% confidence interval	p-value
Intercept	0.11%	0.07% – 0.19%	**<0.001**	0.26%	0.17% – 0.39%	**<0.001**	-0.34%	0.16% – 0.69%	**0.003**
Use of CH-STS	3%	-32% – 58%	0.877	-3%	-28% – 32%	0.864	24%	-36% – 141%	0.529
Presence of endoleak	30%	-20% – 112%	0.292	35%	-7% – 97%	0.110	62%	-20% – 228%	0.183

Table 8 Multivariable linear mixed-effects model demonstrating the effect of embolization with CH-STS (versus CH) and presence of residual endoleak (versus not) on the elastographic parameters of maximum axial deformation, range cumulative axial deformation, and range cumulative axial shear of the intraluminal thrombus obtained using the segmentations performed by reader GS. The estimates for the non-intercept predictors refer to the percentage change of the outcome when CH-STS is used (in comparison to CH) or when a residual endoleak is present (in comparison to not). CH: Chitosan hydrogel embolic agent. CH-STS: Chitosan hydrogel with sodium tetradecyl sulphate embolic agent.

8.4 Comparison of the Embolic Agents and the ILT

The mechanical properties of the CH and CH-STS agent ROIs were compared with those of the ILT ROIs. Using the segmentations obtained by reader GS, the ILT was found to have a 37% lower maximum axial deformation (CI: -56 % to -10%, $p = 0.010$) and a 37% lower range cumulative axial deformation (CI: -57% to -8%, $p = 0.017$) than CH. In contrast, the ILT had a 77% greater maximum axial deformation (CI: -6% to 234%, $p = 0.079$; approaching significance) and a 59% greater range cumulative axial deformation (CI: 1% to 153%, $p = 0.047$) than CH-STS. Therefore, the strain values of the ILT were between those of CH and CH-STS, being stiffer than the former and less stiff than the latter. There was no significant difference between the shear values of CH or CH-STS compared to the ILT.

8.5 Elastographic Analysis of Aneurysm Sac ROI

The means and standard deviations of the maximum axial deformation, range cumulative axial deformation, and range cumulative axial shear of the aneurysm sac ROI—stratified by the type of embolic agent used, the presence of endoleak, and time—are presented in **Table 9** and **Table 10** for readers GS and LS, respectively. The initial multivariable linear mixed-effects model fitted to the outcomes for the aneurysm sac ROI obtained from the GS segmentations are presented in **Table 11**. Time and the interaction terms were either not clinically or statistically relevant and were excluded from the final model.

The final multivariable linear mixed-effects model included the type of embolic agent and the presence of endoleak as predictors (see **Table 12)**. The use of CH-STS was associated with a 29% decrease in maximum axial deformation (CI: -41% to -14%, $p < 0.001$), a 28% decrease in range cumulative axial deformation (CI: -40% to -14%, $p < 0.001$), and a 27% decrease in range cumulative axial shear (CI: -39% to -13%, $p < 0.001$), while controlling for the presence of endoleak. The presence of an endoleak was associated with a 53% increase in maximum axial deformation (CI: 21% to 92%, $p < 0.001$) and a 60% increase in range cumulative axial deformation (CI: 27% to 101%, $p < 0.001$), while controlling for the type of agent used. There was no significant impact of presence of endoleak on the range cumulative axial shear.

(A) Maximum Axial Deformation (%)

Embolic Agent	Presence of endoleak	1 week	1 month	3 months	6 months
CH-STS	Yes	0.143 ± 0.073 n = 4	0.124 ± 0.098 n = 4	0.151 ± 0.106 n= 4	0.117 ± 0.039 n = 1
	No	0.081 ± 0.037 n = 5	0.061 ± 0.028 n = 5	0.068 ± 0.046 n = 5	0.073 ± 0.023 n = 2
CH	Yes	0.230 ± 0.195 n = 7	0.172 ± 0.083 n = 7	0.122 ± 0.069 n = 7	0.122 ± 0.066 n = 1
	No	0.101 ± 0.053 n = 2	0.081 ± 0.042 n = 2	0.133 ± 0.043 n = 2	0.138 ± 0.087 n = 2

(B) Range Cumulative Axial Deformation (%)

Embolic Agent	Presence of endoleak	1 week	1 month	3 months	6 months
CH-STS	Yes	0.335 ± 0.197 n = 4	0.243 ± 0.177 n = 4	0.474 ± 0.541 n = 4	0.276 ± 0.091 n=1
	No	0.201 ± 0.090 n = 5	0.164 ± 0.092 n = 5	0.169 ± 0.118 n = 5	0.158 ± 0.079 n=2
CH	Yes	0.558 ± 0.484 n = 7	0.440 ± 0.268 n = 7	0.415 ± 0.419 n = 7	0.247 ± 0.157 n=1
	No	0.223 ± 0.106 n = 2	0.198 ± 0.133 n = 2	0.323 ± 0.130 n = 2	0.261 ± 0.089 n=2

(C) Range Cumulative Axial Shear (%)

Embolic Agent	Presence of endoleak	1 week	1 month	3 months	6 months
CH-STS	Yes	0.583 ± 0.311 n = 4	0.430 ± 0.285 n = 4	0.859 ± 0.853 n = 4	0.258 ± 0.084 n=1
	No	0.512 ± 0.367 n = 5	0.456 ± 0.277 n = 5	0.458 ± 0.244 n = 5	0.575 ± 0.209 n=2
CH	Yes	0.900 ± 0.698 n = 7	0.725 ± 0.390 n = 7	0.832 ± 1.114 n = 7	0.463 ± 0.362 n=1
	No	0.486 ± 0.405 n = 2	0.459 ± 0.270 n = 2	0.527 ± 0.164 n = 2	0.698 ± 0.396 n=2

Table 9 Mean (± standard deviation) of the (A) maximum axial deformation, (B) range cumulative axial deformation, and (C) range cumulative axial shear of the aneurysm sac region of interest stratified by embolic agent used (CH versus CH-STS), presence of residual endoleak, and time, as obtained by reader GS. CH: Chitosan hydrogel embolic agent. CH-STS: Chitosan hydrogel with sodium tetradecyl sulphate embolic agent; n: number of aneurysms (with three observations per aneurysm).

(A) Maximum Axial Deformation (%)

Embolic Agent	Presence of endoleak	1 week	1 month	3 months	6 months
CH-STS	Yes	0.190 ± 0.228 n = 4	0.131 ± 0.101 n = 4	0.138 ± 0.092 n= 4	0.102 ± 0.058 n = 1
	No	0.076 ± 0.035 n = 5	0.076 ± 0.046 n = 5	0.083 ± 0.045 n = 5	0.063 ± 0.020 n = 2
CH	Yes	0.230 ± 0.213 n = 7	0.175 ± 0.080 n = 7	0.109 ± 0.057 n = 7	0.105 ± 0.046 n = 1
	No	0.114 ± 0.018 n = 2	0.075 ± 0.012 n = 2	0.149 ± 0.043 n = 2	0.122 ± 0.033 n = 2

(B) Range Cumulative Axial Deformation (%)

Embolic Agent	Presence of endoleak	1 week	1 month	3 months	6 months
CH-STS	Yes	0.347 ± 0.307 n = 4	0.260 ± 0.176 n = 4	0.375 ± 0.329 n = 4	0.222 ± 0.125 n=1
	No	0.178 ± 0.083 n = 5	0.190 ± 0.108 n = 5	0.179 ± 0.095 n = 5	0.135 ± 0.021 n=2
CH	Yes	0.551 ± 0.485 n = 7	0.439 ± 0.252 n = 7	0.375 ± 0.329 n = 7	0.191 ± 0.090 n=1
	No	0.269 ± 0.125 n = 2	0.202 ± 0.072 n = 2	0.339 ± 0.110 n = 2	0.284 ± 0.066 n=2

(C) Range Cumulative Axial Shear (%)

Embolic Agent	Presence of endoleak	1 week	1 month	3 months	6 months
CH-STS	Yes	0.620 ± 0.376 n = 4	0.444 ± 0.305 n = 4	0.695 ± 0.632 n = 4	0.239 ± 0.020 n=1
	No	0.533 ± 0.383 n = 5	0.451 ± 0.228 n = 5	0.430 ± 0.206 n = 5	0.650 ± 0.344 n=2
CH	Yes	0.895 ± 0.696 n = 7	0.733 ± 0.421 n = 7	0.846 ± 1.207 n = 7	0.349 ± 0.306 n=1
	No	0.491 ± 0.307 n = 2	0.510 ± 0.443 n = 2	0.601 ± 0.284 n = 2	0.833 ± 0.289 n=2

Table 10 Mean (± standard deviation) of (A) maximum axial deformation, (B) range cumulative axial deformation, and (C) range cumulative axial shear of the aneurysm sac region of interest stratified by embolic agent, presence of residual endoleak, and time, as obtained by reader LS. CH: Chitosan hydrogel embolic agent. CH-STS: Chitosan hydrogel with sodium tetradecyl sulphate embolic agent; n: number of aneurysms (three observations per aneurysm).

Predictor	Maximum axial deformation			Range cumulative axial deformation			Range cumulative axial shear		
	Estimate	95% confidence interval	p-value	Estimate	95% confidence interval	p-value	Estimate	95% confidence interval	p-value
Intercept	0.11%	0.07% – 0.16%	**<0.001**	0.23	0.15% – 0.34%	**<0.001**	0.63	0.41% – 0.98%	**0.041**
CH-STS	-41%	-61% – -9%	**0.019**	-32%	-55% – 5%	0.084	-31%	-54% – 5%	0.083
Time	0%	0% – 0%	0.514	0%	0% – 0%	0.813	0%	0% – 0%	0.72
Presence of endoleak	38%	-5% – 99%	0.087	62%	12% – 132%	**0.01**	-12%	-39% – 26%	0.472
Interaction: Agent and time	0%	0% – 0%	0.387	0%	0% – 0%	0.515	0%	0% – 0%	0.339
Interaction: Agent and endoleak	17%	-30% – 95%	0.535	-3%	-41% – 60%	0.904	-6%	-42% – 54%	0.815

Table 11 Multivariable linear mixed-effects model demonstrating the effect of embolization with CH-STS (vs. CH), presence of residual endoleak (vs. not), and time on the elastographic parameters of maximum axial deformation, range cumulative axial deformation, and range cumulative axial shear obtained using the segmentations by reader GS. The estimates for the non-intercept predictors refer to the percentage change of the outcome when the predictor is present. CH: Chitosan hydrogel embolic agent. CH-STS: Chitosan hydrogel with sodium tetradecyl sulphate embolic agent.

Predictor	Maximum axial deformation			Range cumulative axial deformation			Range cumulative axial shear		
	Estimate	95% confidence interval	p-value	Estimate	95% confidence interval	p-value	Estimate	95% confidence interval	p-value
Intercept	0.09%	0.07% – 0.12%	**<0.001**	0.22%	0.17% – -0.30%	**<0.001**	0.66%	0.47% – 0.92%	**0.015**
Use of CH-STS	-29%	-41% – -14%	**<0.001**	-28%	-40% – -14%	**<0.001**	-27%	-39% – -13%	**<0.001**
Presence of endoleak	53%	21% – 92%	**<0.001**	60%	27% – 101%	**<0.001**	-14%	-31% – 8%	0.186

Table 12 Multivariable linear mixed-effects model examining the effect of embolization with CH-STS (vs. CH) and presence of residual endoleak (vs. not) on the elastographic parameters maximum axial deformation, range cumulative axial deformation, and range cumulative axial shear of the aneurysm sac obtained using the segmentations by reader GS. The estimates for the non-intercept predictors refer to the percentage change of the outcome when the predictor is present. CH: Chitosan hydrogel embolic agent. CH-STS: Chitosan hydrogel with sodium tetradecyl sulphate embolic agent.

8.6 Comparison Between Readers

The ICC of the maximum axial deformation, range cumulative axial deformation, and range cumulative axial shear obtained from the GS and LS segmentations are provided in **Table 13**. The ICC of the point estimates for all three outcomes were good (falling between the range of 0.75-0.9) as per Portney and Gross (231). Further interpretation of these findings will be presented in the discussion.

Parameter	Intraclass correlation	95% confidence interval
Maximum Axial Deformation	0.807	0.754 – 0.849
Range Cumulative Axial Deformation	0.842	0.798 – 0.877
Range Cumulative Axial Shear	0.874	0.838 – 0.902

Table 13 Intraclass correlation coefficients comparing the inter-observer reliability of the maximum axial deformation, range cumulative axial deformation, and range cumulative axial shear obtained from the segmentations performed by the readers GS and LS.

Chapter 9 – Discussion

9.1 Orientation of Discussion Section

The goal of the present study was to characterize the mechanical properties of the constituents of aneurysm sacs post-EVAR and embolization with sclerosing and non-sclerosing chitosan-based hydrogels using SUE. In the present chapter, the most important results will be summarized (**Section 9.2**). The mechanical properties of the embolic agents and the ILT will then be interpreted, as they represent the most homogenous structures (**Sections 9.3** and **9.4**, respectively); their mechanical properties will then be compared in **Section 9.5**. The interpretation of the aneurysm sac mechanical properties will be described subsequently (**Section 9.6**) as this builds upon the understanding of the mechanical properties of the former two ROIs. Next, the inter-observer reliability of the technique will be contextualized (**Section 9.7**). Finally, the limitations of the study will be described (**Section 9.8**).

9.2 Summary of Results

1. CH-STS demonstrated a 66 % lower maximum axial deformation ($p < 0.001$) and a 67% lower range cumulative axial deformation ($p < 0.001$) than CH.
2. There was no significant difference in the mechanical properties of the ILT ROIs between treatment groups.
3. CH-STS was stiffer than the ILT and the ILT was stiffer than CH.
    - The ILT had a 37% lower maximum axial deformation ($p = 0.010$) and a 37% lower range cumulative axial deformation ($p = 0.017$) than CH.
    - The ILT had a 77% greater maximum axial deformation ($p = 0.079$; trending towards significance) and a 59% greater range cumulative axial deformation ($p = 0.047$) than CH-STS.
4. (A) Aneurysm sacs embolized with CH-STS had a 29% lower maximum axial deformation ($p < 0.001$), a 28% lower range cumulative axial deformation ($p < 0.001$), and a 27% lower range cumulative axial shear ($p < 0.001$) than those embolized with CH, even when controlling for presence of endoleak.

   (B) The presence of residual endoleak post-embolization was associated with a 53% increase in maximum axial deformation ($p < 0.001$) and a 60% increase in range cumulative axial deformation ($p < 0.001$), even when controlling for type of agent used.
5. The ICCs of the mechanical properties obtained via SUE using the segmentations performed by two independent readers demonstrated good inter-observer reliability, with point estimates ranging between 0.807-0.874.

9.3 Elastographic Analysis of the Embolic Agents

The importance of embolic agent stiffness on the treatment of endoleaks reflects two fundamental principles: occlusivity and wall stress reduction. Agents that can withstand higher stresses are thought to be better able resist blood flow, theoretically reducing the risk of technical and clinical failure (42, 43). Stiffer embolic agents may also provide a stabilizing effect on the aneurysm by decreasing wall stress, which is an important determinant for aneurysm rupture (232).

CH-STS demonstrated significantly lower strain values than CH in vivo at sacrifice. This finding corresponds with the rheometry studies performed by Fatimi et al and Zehtabi et al, both of which demonstrated that the addition of STS to chitosan-based embolic agents increased the gels' storage moduli, likely by increasing chitosan chain aggregation (42, 43). Injected CH-STS had a storage modulus of approximately 6 kPa, while injected CH had a storage modulus of approximately 1 kPa. It should be noted, however, that both CH and CH-STS were able to achieve storage moduli over 0.8 kPa in these studies, which was considered the threshold for vascular occlusion based on an in vitro bench test (42, 43). Interestingly, the presence of endoleak was not a significant predictor of the strain or shear values of the embolic agent at sacrifice. The suggests that the measured differences in strain may actually represent intrinsic differences in the mechanical properties of the agents, rather than being significantly confounded by the presence of an additional deforming force.

The in vivo mechanical properties of CH and CH-STS have been previously assessed using SWI by Bertrand-Grenier et al (31). They found that CH-STS tended to have a greater elastic modulus than CH at three-months post-embolization, but not at six-months post-embolization. However, there were several limitations to their analysis. First, their observations at six months may have been biased given that there were fewer subjects. Second, statistical analyses were not performed to compare the treatment groups to determine if the aforementioned differences were significant. Third, the level of expertise of the observers performing the segmentations was different. Fourth, true differences between the embolic agents may have been masked due to inaccurate SWI measurements caused by (a) violations of the fundamental assumptions of SWI regarding tissue homogeneity and tissue isotropy, which are often inaccurate in intravascular tissues and (b) poor ARFI penetration (31, 32). Therefore, the results of the present SUE analysis, particularly given that they reflect the in vitro data, are thought to be more accurate. The study by Bertrand-Grenier et al did not attempt to control for the presence of endoleak as a predictor for the elasticity of the agent (31), therefore the impact of residual endoleak on elasticity cannot be compared directly between SUE and SWI. However, given that SWI utilizes ARFIs instead of an internal deforming force to generate tissue deformation, the presence of an endoleak should also not theoretically impact the elasticity measurements. There is limited

additional data in the literature regarding the in vivo characterization of other solid embolic agents for further comparison; this would be of interest for future studies.

9.4 Elastographic Analysis of the ILT

ILTs are found in the majority of AAAs (233). However, their role in the pathogenesis of aneurysmal rupture remain unclear. Some authors suggest that ILTs reduces sac pressure and peak wall stress, thereby acting as a mechanical shield/cushion (234, 235). Others state that ILTs are associated with pro-inflammatory processes (236) and that larger thrombi are associated with aneurysm expansion and rupture—perhaps acting as a surrogate marker for decreased aortic wall strength (27, 237, 238). In reality, both of these hypotheses may have merit. Regarding specifically the mechanical properties of ILTs, it has been demonstrated that not only does the presence of ILT impact the wall stresses, but that stiffer ILTs decrease wall stress better than less stiff ILTs (27). In general, thrombi become stiffer as they become more organized (28, 30, 31) and poor thrombus organization may account for the non-shrinkage of aneurysms and endotension, both of which may require subsequent intervention (26). The predictive value of thrombus organization on the presence of endoleak has not been established (26, 28, 32).

The impact of embolization with CH-STS versus CH as well as the presence of residual endoleak on overall ILT stiffness was assessed in the present study; there were no significant differences in the strain or shear parameters of the ILT with respect to these predictors. The finding that there was no difference in the ILT between the treatment groups was not necessarily surprising. First, while STS is thrombogenic (176), it is unclear as to whether its use would result in the formation of thrombus of greater quality, as thrombus formation is dependent on many factors, including endothelial damage, stasis, and coagulability (43, 239). Interestingly, while the use of low concentration STS (0.075–0.1%) is associated with strong clot formation, the use of high concentration STS (≥ 0.3%) has been shown to generate weak clots that are susceptible to lysis, likely due to inhibition/destruction of clotting factors (240). Since the concentration of STS released from CH-STS into the aneurysm sac is presently unknown, however, at maximum, the present study suggests that the quality of thrombus produced by CH-STS may not be superior. Second, given that the surgical creation of aneurysms was performed eight weeks before EVAR, it is possible that a portion of the sac thrombus was deposited prior to the intervention, as is seen with the deposition of ILT in human AAAs. Finally, as shown by Soulez et al in 2008, the presently used endoleak model is expected to generate ILT after EVAR even without embolization; this would have the effect of mitigating differences between treatment groups (171). The culmination of these factors suggests that the measured mechanical properties of the thrombus could reasonably be expected to be the same between treatment groups. Unfortunately, the SWI study by Bertrand-Grenier et al on the subjects used in the present study did not compare the elasticity of the total thrombus by the type of embolic agent used to verify these results (31).

The finding that the presence of endoleak was not a significant predictor of thrombus strain/shear values was somewhat unexpected. On the one hand, previous SUE results have shown that the mechanical properties of the thrombi generated in association with type I and type II endoleaks are similar (28); therefore, the primary deforming force may not be from the endoleak (as type I endoleaks are generally thought to provide a greater deforming force than type II endoleaks), but from the pulsations through the stent-graft. Additionally, the extent to which partially embolized endoleaks are able to deform the surrounding tissue is unclear and poorly described, particularly given the heterogeneity of the morphologies of the residual endoleaks (28, 241, 242). On the other hand, one might expect that the ILT in aneurysm sacs with residual endoleaks would be less stiff as they would be supplied directly with antithrombotic substances (243). The impact of residual endoleak on the measured strain and shear parameters of the thrombus may have therefore been limited by type II error given the relatively low sample sizes. This conclusion is supported by two findings: 1) There was a trend for decreased strain values of the thrombus in the no endoleak group in comparison to the endoleak group, regardless of agent used (see **Section 8.3**) and 2) the presence of endoleak did have an effect on the aneurysm sac ROI mechanical properties independent of the type of embolic agent (see **Section 9.6** for further details).

The mechanical properties of the ILT post-EVAR have been assessed via elastography in several studies, with conflicting results. SUE and SWI have both demonstrated that organized ILTs in a preclinical endoleak model have significantly lower strain values and significantly greater elastic moduli than fresh ILTs (28, 30). However, the clinical impact of these findings remains unclear, as these subtypes of thrombi cannot be distinguished on routine imaging. In a study by Bando et al, patients who underwent immediate post-EVAR 2D SWI that eventually went on to develop endoleaks had ILTs with a greater elasticity index (greater stiffness) compared to those who did not. The group suggested that a stiffer thrombus may prevent a decrease in sac contraction and pressure, creating favorable conditions for a type II endoleak (33). This is a controversial conclusion, however, as one could argue that a stiffer thrombus should *prevent* blood flow and recanalization. In contrast, a clinical study comparing patients with and without endoleaks using SWI demonstrated that thrombus elasticity was not statistically different between the groups (32). Finally, the study by Bertrand-Grenier et al using subjects in the present study found a trend towards increased thrombus stiffness in aneurysms without residual endoleak (although this was not statistically significant); the advantage of this study was that it could demonstrated thrombus evolution over time (31). Ultimately, there is no clear consensus within the literature regarding the predictive value of thrombus stiffness on presence of endoleak. However, it should be noted that there is heterogeneity amongst these studies with respect to the subjects (humans versus. animals), experimental conditions (status post embolization or not), time of elastography, and length of follow-up. Further studies with larger sample sizes are required to better elucidate the relationship between ILT mechanical properties and endoleaks in vivo.

9.5 Comparison of the Elastographic Properties of the Embolic Agents and the ILT

CH-STS was found to be stiffer than the ILT (as well as CH, as was discussed in **Section 9.3**) and CH was found to be less stiff than the ILT. Given the previously described benefits of incorporating a stiffer substance into the aneurysm sac to reduce wall stress and to prevent endoleak recurrence, this finding legitimizes the use of CH-STS as an embolic agent (27, 177). However, this difference is difficult to interpret in the context of real-world intrinsic mechanical properties given that 1) SUE gives measurements of strain/deformation as opposed to elastic moduli and 2) reported in vitro mechanical properties of CH-STS/CH and of ILTs are technique dependent and vary between sources. As previously described, prior studies have found that the storage moduli of CH-STS and CH—calculated using a rheometer with a fixed stress amplitude of 1 Pa—are approximately 6 kPa and 1 kPa, respectively (43, 177). Van Dam et al reported that the storage modulus of the ILT was approximately 1.7 ± 1.3 kPa for small strains using a different, non-linear multimode model (244). However, it is unclear as to whether these two techniques have reasonable agreement. There is also substantial variability in the moduli reported for ILTs in the literature, given the differences in techniques and the types of thrombi measured (245). Adding to the confusions, other commonly reported elasticity measures of the ILT, such as the Young's modulus, are currently unknown for CH-STS and CH. Therefore, caution must be used in comparing the mechanical properties of the gels and thrombi across studies. Future investigations studies could be geared towards more systematic in vitro comparisons of these entities as well as towards the direct correlation in vitro and in vivo findings.

The most direct comparison of the in vivo results obtained in the present study comes from the study by Bertrand-Grenier et al, which used SWI to characterize the subjects in the present study. In contrast to the SUE results, they found no significant difference between the agents (pooling CH and CH-STS together) and organized thrombus, with elasticity measurements on the order of approximately 50 kPa (31). However, these results are called into question because this technique did not show significant differences between the mechanical properties of CH and CH-STS, whereas SUE could (better reflecting the in vitro data (see **Section 9.3**)). The suspected superiority of SUE is this regard is thought to be due to the technical limitations of SWI. As previously described, SWI relies on several assumptions with regards to tissue homogeneity and isotropy that might not be accurate in the intravascular setting Furthermore, signal loss due to poor penetration of the ARFIs may have also decreased the sensitivity of SWI (31, 32, 188). Ultimately, further studies using similar techniques may be necessary to adequately compare the mechanical properties of the embolic agents in comparison to their associated ILT.

9.6 Elastographic Analysis of the Aneurysm Sac

The aneurysm sac is heterogeneous in its composition, containing both embolic agent and ILT. Therefore, the mechanical properties of this region of interest represent a composite of the mechanical properties of these two constituents. Aneurysm sac stiffness is a useful clinical parameter because it can be easily segmented on clinical follow-up imaging and can provide information regarding the overall stability of the aneurysm (31). In the context of an embolized endoleak, a stiffer sac is taken to represent a favorable outcome because it would indicate that there is an increased resistance to flow and that less stress would be transmitted to the aneurysm wall (27, 177) (see **Section 9.3**). To limit biasing secondary to the heterogeneous distribution of the embolic agent and ILT in the aneurysm sac, measurements of sac stiffness at multiple levels is mandatory.

Aneurysm sacs embolized with CH-STS had significantly lower strain and shear values than those embolized with CH, even when controlling for the presence of residual endoleak. It is suspected that the embolic agent—as opposed to the associated ILT—was the primer driver for this difference, as discussed in **Section 9.3**. While the ILT also contributes to the overall sac stiffness, it appears that their mechanical properties were not significantly different between the embolization groups, as outlined in **Section 9.4**.

The presence of a residual endoleak post-embolization was associated with greater aneurysm sac strain values. This has two potential interpretations. The first is that endoleaks create a second deforming force on the constituents of the sac—in addition to the pulsations through the aortic stent—which resulted in increased strain measurements not related to the sacs' mechanical properties. However, this raises the question as to why a similar relationship was not seen between endoleak persistence and the strain values of the individual agent ROIs and ILT ROIs. One possibility is that these were type II errors, particularly with respect to the ILT (as detailed previously in **Section 9.4**); since the aneurysm sac ROI had more data points, the significance of this relationship was only correctly elucidated for this parameter. Another possibility is that since the mechanical properties of the aneurysm sac were calculated to include three different levels, it was more sensitive to local deformations by residual endoleaks. For example, by only selecting one level for the characterization of the agent and ILT ROIs for each aneurysm, asymmetrically distributed sac pressures from a residual endoleak (which may have been located at another extreme of the aneurysm) may not have deformed the region of interest. However, this limitation was unavoidable because the individual ILT and embolic agent ROIs may not have been present at all levels of the aneurysm sac. A third possibility is that, although not significantly, time may have impacted the effect of endoleaks. On review of the mean strain values in **Tables 9** and **10**, it appears as though the greatest differences in the strain values between the endoleak and no endoleak groups were at 1 week, but that this difference was less

appreciable over time. Therefore, at sacrifice, a significant impact of endoleak on the mechanical properties of the agent or ILT may not have been elucidated.

A second interpretation of the observed relationship between the presence of residual endoleak and increased sac strain is that *because* certain aneurysm sacs were less stiff, endoleaks were more likely to form. This hypothesis is supported by the previously described role of mechanical occlusivity in preventing blood flow into the sac (43). However, other factors, such as vascular de-endothelialization, may have also played a role in this relationship. Ultimately, the potentially confounding role of endoleaks points to a weakness of SUE in measuring the mechanical properties of sac contents: the measured strains/shears are dependent on the magnitude of the force applied, which is unknown. In the study by Bertrand-Grenier et al, total aneurysm sac was not identified as a region of interest, therefore comparisons with SWI (which does not rely on internally derived deformations) cannot be made (31). However, given that the aneurysm sac ROI is inherently heterogenous, its characterization by SWI may not have been appropriate.

Regardless of the origin of this relationship, the finding that residual endoleaks are associated with greater sac strain values is a highly useful clinically. Salloum et al have demonstrated that SUE can characterize endoleaks as areas of high signal decorrelation (aliasing) (28). The present study demonstrates that even when these areas are excluded, there are differences in sac strain that can be detected in subjects with and without endoleaks. This information could be useful for future non-invasive characterization of aneurysm sacs, particularly when there is clinical equipoise regarding the presence of an endoleak or whether an identified endoleak is clinically significant (particularly with respect to type II or V endoleaks). It should be noted, however, that sac mechanical parameters were not used to predict the presence of endoleak; this would be of interest in future studies. Future studies could also be directed at using SUE to monitor sac healing with non-embolized aneurysm sacs.

That time was not a clinically significant predictor of sac mechanical properties or the embolized aneurysm sacs was an unexpected finding. The hypothesized natural history of successful EVAR, as well of successful endoleak embolization, is a progressive decrease in sac pressure (246, 247). The current findings somewhat challenge this hypothesis. One possible reason is that embolization is an all-or-nothing phenomenon; successful embolization decreases sac strain, while unsuccessful embolization does not. As previously descried, patient's status post EVAR may have high proportions of fresh thrombus within the aneurysm sac for years after EVAR (26), therefore progressive thrombus organization is not necessarily the rule. Another possibility is that there were two counteracting processes occurring over time. Bertrand-Grenier et al showed that there was a non-significant trend towards increased thrombus organization of embolized endoleaks over the course of follow-up (31). However, since the aneurysm sacs contained biodegradable CH-based agents, it is possible that decreased strain/shear values of the ILT were offset by

the degradation—and increased strain/shear values—of the gel agents over time (43). Ultimately, further studies regarding the evolution of sac stiffness and pressures over time following embolization are required.

9.7 Inter-observer Reliability

There was good inter-observer reliability of the strain and shear measurements derived from the independent segmentations of the aneurysm sac, embolic agent, and ILT ROIs, with point estimates ranging from 0.807 to 0.874 (231). Given that SUE is proposed as an adjunctive technique to conventional DUS, as opposed to one that will replace it, the authors believe that these early results indicate that SUE has sufficient inter-observer reliability to justify its further investigation clinically.

Upon review of **Tables 5, 7, 9, and 10**, however, there were important differences noted between the strain and shear parameters obtained by the two readers' segmentations. This was likely due to a combination of factors. First, there is expected variability with US-based segmentation techniques due to the limited contrast resolution. This is especially true given that that some of the ROIs (such as the ILT ROI and agent ROI) could not be precisely delineated on B-mode cines and that their distinction relied on correlation with other imaging and histopathology (which is subject to individual interpretation and misregistration). Second, the spurious inclusion of the stent-graft, the aneurysm wall, or any endoleak into any of the ROIs by one of the readers may have significantly biased the results; both readers attempted to mitigate this by segmenting conservatively. Third, there was an important difference in experience between the junior and senior interpreter; with interpreters of similar, advanced experience, the inter-observer variability would be expected to be improved. Finally, the small sample sizes for each subgroup presented in the aforementioned tables makes the individual means susceptible to sampling bias. Therefore, it is felt that the ICCs, which compare the obtained values more globally, were better suited for comparing the results of the two observers.

Unfortunately, there is little data available in the literature to contextualize the inter-observer reliability demonstrated in the present study. Shear wave imaging has been found to a have moderate-to-strong level of agreement with respect to its ability to detect endoleaks (30, 32, 248); however, the inter-observer reliability with respect to the prediction of a categorical outcome addresses a fundamentally different question than the one posed by the present study. Thus, at maximum, this study adds to the body of evidence that suggests elastography is a reliable tool for the characterization of aneurysms post-EVAR. Future studies with the inclusion of additional sources of variability that may arise in clinical practice—as well as the exclusion of parts of the imaging processing workflow that could be automated—are required for further validation.

9.8 Study Limitations

9.8.1 Limitations of the Canine Model

The use of a canine bilateral common iliac aneurysm model poses several limitations. Dogs are the standard experimental subjects for arterial graft studies given their similar thrombotic profile and similar resistance to neo-endothelial formation as compared to humans (249). However, the surgical creation of aneurysms in otherwise healthy subjects does not reflect the underlying cardiovascular pathologies from which AAAs tend to originate. For example, the surgically implanted venous patches do not have the features of inflammation or wall weakening that characterize AAAs (77, 81, 82). In contrast, the model did allow for the reliable recreation of similar aneurysms and endoleaks in an all subjects (171); furthermore, for the purposes of the present study, the wall characteristics were not particularly relevant. Secondly, the use of a bilateral common iliac aneurysm model may have removed some of the unique hemodynamic stresses that act upon the abdominal aorta (83). However, this approach did allow for the reliable creation of high flow type I endoleaks (which may be seen clinically with a communicating lumbar or inferior mesenteric artery) as well as for a more controlled comparison of the effects of CH-STS and CH with fewer subjects. Thirdly, the endoleaks in this model were created by deformation of a balloon expandable stent, which is dissimilar to EVAR in two ways: 1) EVAR stents are self-expandable and more rigid and 2) type I endoleaks tend to occur secondary to hostile landing zone anatomy or changes in the aneurysm configuration over time (117, 118). In contrast, the use of a self-expandable arterial stent in this model would have impeded balloon deformation, and the reliable recreation of hostile landing zone characteristics would have been untenable on a short-term scale. Finally, in clinical practice, transarterial endoleak embolization is first line therapy for type II endoleaks, as opposed to the type I endoleaks that were used in the present study (1). The type I endoleak model was favored, however, because it creates larger, more challenging endoleaks, which lends greater robustness to the conclusions regarding gels' impact (171). Moreover, embolization is an acceptable alternative for the treatment of type I endoleaks (1).

9.8.2 Limitations of SUE

There are several limitations associated with the use of SUE for the characterization of the contents of embolized endoleaks. First, as with all methods of strain elastography, SUE cannot calculate intrinsic tissue parameters (i.e. the elastic moduli) of the imaged regions of interest because the internal stress distribution is unknown (187). This makes the generalizability of the values obtained in the present study unclear. Of note, intrasac pressure measurements were not performed to attempt to quantify the stress distribution, as previous experiments indicated that mean sac pressures did not correlate with the strain of the sac contents (28). Furthermore, sac pressure measurements are invasive and are not routinely performed clinically. While

other forms of elastography (e.g. SWI) can attempt to calculate the tissue elastic moduli of the sac content, their limitations have already been described, and SUE tends to have greater penetration and robustness (30-32, 188). Second, the ultrasound probe used for SUE has superior axial, rather than lateral resolution. This was thought to be why the shear measurements tended to less frequently show significant differences for the various comparisons. Third, calculation of elastographic parameters using SUE is limited by the fact that it is a two-step process: in the first step, raw RF acquisition are obtained at the bedside, and in the second step, the acquisitions are post-processed on a separate workstation. This entails two separate issues: (a) repeat scans cannot be performed to improve the quality of the acquisitions prior to elastographic analysis (such as when there is out-of-plane or breathing motion); and (b) the multiple steps make the process labor intensive, which may limit clinical uptake. Future iterations of SUE that provide real-time elastographic analysis may mitigate these limitations. Fourth, the use of internal deformations to generate tissue stress in SUE is limited technically by the application of spurious additional forces (such as respiratory motion or patient movement), which result in out of plane artifacts as well as the application of an additional stresses not accounted for by the pulsations of the aorta. Clinically, an experienced operator who provides clear instructions (such for breath-holds) could be reduce these artifacts. Finally, with respect to characterizing the individual constituents of aneurysm sacs clinically, SUE is limited by the ability of B-mode imaging to distinguish different ROIs for segmentation. However, this is where the utility of composite measures (such as the aneurysm sac ROI) emerges. As such, post-embolization, SUE may be better suited for following changes in a given aneurysm sac's mechanical properties over time, rather than for comparing aneurysms that have been embolized with different agents.

9.8.3 Limitations of the Experimental Design

The major limitation of the study lies in its ability to predict future outcomes. For example, while the presence of residual endoleak was associated with significantly higher strain values of the aneurysm sac, this exploratory study was not designed to predict at what strain values an endoleak was likely to be present. Furthermore, while the strain/shear values added additional information to the characterization of embolized endoleaks, their relevance to hard clinical outcomes—such as sac expansion or rupture—cannot be extrapolated due to the short time frame and the limitations of the surgical model (see **Section 9.8.1**). Finally, while the use of a stiffer agent (CH-STS) was associated with favorable outcomes and supports its further development as an embolic agent, given that there are no current commercial agents that offer a similar therapeutic profile for the treatment of endoleaks (being both occlusive and sclerosing), the immediate clinical application of these results to embolic agent selection is limited.

Another important limitation of the study's experimental design is the low sample size. As previously described, it is possible that a significant relationship between the presence of residual endoleak and the ILT

strain/shear outcomes was not elucidated because of this limitation. Furthermore, actual differences in shear outcomes (with respect to other comparisons where significant differences between strain outcomes were identified) may have also gone undetected given the relatively low number of subjects coupled with the technical limitations of measuring shear described in **Section 9.8.2**. Ultimately, while the present study demonstrates that SUE shows promise for the characterization aneurysm contents, further studies with larger cohorts are required.

9.9 Conclusion

SUE was used to characterize the mechanical properties of endoleaks embolized with CH-STS and CH. CH-STS had significantly lower strain values than CH. CH-STS also had lower strain values than the ILT. Overall, aneurysm sacs embolized with CH-STS tended to have lower strain values than those embolized with CH, even when controlling for the presence of endoleak. These findings lend legitimacy to the use of CH-STS as an embolic agent for the treatment of endoleaks. Additionally, residual endoleaks were associated with greater sac strain, regardless of embolic agent used, which may be a useful clinical finding in the follow-up of patients post-embolization.

Bibliography

1. Chaikof EL, Dalman RL, Eskandari MK, Jackson BM, Lee WA, Mansour MA, et al. The Society for Vascular Surgery practice guidelines on the care of patients with an abdominal aortic aneurysm. J Vasc Surg. 2018;67(1):2-77.e2.
2. Norman PE, Curci JA. Understanding the effects of tobacco smoke on the pathogenesis of aortic aneurysm. Arterioscler Thromb Vasc Biol. 2013;33(7):1473-7.
3. Kent KC, Zwolak RM, Egorova NN, Riles TS, Manganaro A, Moskowitz AJ, et al. Analysis of risk factors for abdominal aortic aneurysm in a cohort of more than 3 million individuals. J Vasc Surg. 2010;52(3):539-48.
4. Li X, Zhao G, Zhang J, Duan Z, Xin S. Prevalence and trends of the abdominal aortic aneurysms epidemic in general population--a meta-analysis. PLoS One. 2013;8(12):e81260.
5. Karthikesalingam A, Holt PJ, Vidal-Diez A, Ozdemir BA, Poloniecki JD, Hinchliffe RJ, et al. Mortality from ruptured abdominal aortic aneurysms: clinical lessons from a comparison of outcomes in England and the USA. Lancet. 2014;383(9921):963-9.
6. Paravastu SC, Jayarajasingam R, Cottam R, Palfreyman SJ, Michaels JA, Thomas SM. Endovascular repair of abdominal aortic aneurysm. Cochrane Database Syst Rev. 2014(1):Cd004178.
7. Greenhalgh RM, Brown LC, Kwong GP, Powell JT, Thompson SG. Comparison of endovascular aneurysm repair with open repair in patients with abdominal aortic aneurysm (EVAR trial 1), 30-day operative mortality results: randomised controlled trial. Lancet. 2004;364(9437):843-8.
8. Lederle FA, Freischlag JA, Kyriakides TC, Padberg FT, Jr., Matsumura JS, Kohler TR, et al. Outcomes following endovascular vs open repair of abdominal aortic aneurysm: a randomized trial. JAMA. 2009;302(14):1535-42.
9. Prinssen M, Verhoeven EL, Buth J, Cuypers PW, van Sambeek MR, Balm R, et al. A randomized trial comparing conventional and endovascular repair of abdominal aortic aneurysms. N Engl J Med. 2004;351(16):1607-18.
10. Arko FR, Hill BB, Reeves TR, Olcott C, Harris EJ, Fogarty TJ, et al. Early and late functional outcome assessments following endovascular and open aneurysm repair. J Endovasc Ther. 2003;10(1):2-9.
11. Parodi JC, Palmaz JC, Barone HD. Transfemoral intraluminal graft implantation for abdominal aortic aneurysms. Ann Vasc Surg. 1991;5(6):491-9.
12. Malas M, Arhuidese I, Qazi U, Black J, Perler B, Freischlag JA. Perioperative mortality following repair of abdominal aortic aneurysms: application of a randomized clinical trial to real-world practice using a validated nationwide data set. JAMA Surg. 2014;149(12):1260-5.

13. Greenhalgh RM, Brown LC, Powell JT, Thompson SG, Epstein D, Sculpher MJ. Endovascular versus open repair of abdominal aortic aneurysm. N Engl J Med. 2010;362(20):1863-71.
14. De Bruin JL, Baas AF, Buth J, Prinssen M, Verhoeven EL, Cuypers PW, et al. Long-term outcome of open or endovascular repair of abdominal aortic aneurysm. N Engl J Med. 2010;362(20):1881-9.
15. Tadros RO, Faries PL, Ellozy SH, Lookstein RA, Vouyouka AG, Schrier R, et al. The impact of stent graft evolution on the results of endovascular abdominal aortic aneurysm repair. J Vasc Surg. 2014;59(6):1518-27.
16. Zaiem F, Almasri J, Tello M, Prokop LJ, Chaikof EL, Murad MH. A systematic review of surveillance after endovascular aortic repair. J Vasc Surg. 2018;67(1):320-31.e37.
17. Abraha I, Luchetta ML, De Florio R, Cozzolino F, Casazza G, Duca P, et al. Ultrasonography for endoleak detection after endoluminal abdominal aortic aneurysm repair. Cochrane Database Syst Rev. 2017;6(6):Cd010296.
18. Ashoke R, Brown LC, Rodway A, Choke E, Thompson MM, Greenhalgh RM, et al. Color duplex ultrasonography is insensitive for the detection of endoleak after aortic endografting: a systematic review. J Endovasc Ther. 2005;12(3):297-305.
19. Armerding MD, Rubin GD, Beaulieu CF, Slonim SM, Olcott EW, Samuels SL, et al. Aortic aneurysmal disease: assessment of stent-graft treatment-CT versus conventional angiography. Radiology. 2000;215(1):138-46.
20. Pandey N, Litt HI. Surveillance Imaging Following Endovascular Aneurysm Repair. Semin Intervent Radiol. 2015;32(3):239-48.
21. Habets J, Zandvoort HJ, Reitsma JB, Bartels LW, Moll FL, Leiner T, et al. Magnetic resonance imaging is more sensitive than computed tomography angiography for the detection of endoleaks after endovascular abdominal aortic aneurysm repair: a systematic review. Eur J Vasc Endovasc Surg. 2013;45(4):340-50.
22. Ophir J, Cespedes I, Ponnekanti H, Yazdi Y, Li X. Elastography: a quantitative method for imaging the elasticity of biological tissues. Ultrason Imaging. 1991;13(2):111-34.
23. Maurice RL, Ohayon J, Fretigny Y, Bertrand M, Soulez G, Cloutier G. Noninvasive vascular elastography: theoretical framework. IEEE Trans Med Imaging. 2004;23(2):164-80.
24. Maurice RL, Bertrand M. Lagrangian speckle model and tissue-motion estimation--theory. IEEE Trans Med Imaging. 1999;18(7):593-603.
25. Nguyen VL, Leiner T, Hellenthal FA, Backes WH, Wishaupt MC, van der Geest RJ, et al. Abdominal Aortic Aneurysms with High Thrombus Signal Intensity on Magnetic Resonance Imaging are Associated with High Growth Rate. J Vasc Surg. 2014;60(6):1713.

26. Cornelissen SA, Verhagen HJ, van Herwaarden JA, Vonken EJ, Moll FL, Bartels LW. Lack of thrombus organization in nonshrinking aneurysms years after endovascular abdominal aortic aneurysm repair. J Vasc Surg. 2012;56(4):938-42.
27. Speelman L, Schurink GW, Bosboom EM, Buth J, Breeuwer M, van de Vosse FN, et al. The mechanical role of thrombus on the growth rate of an abdominal aortic aneurysm. J Vasc Surg. 2010;51(1):19-26.
28. Salloum E, Bertrand-Grenier A, Lerouge S, Kauffman C, Heon H, Therasse E, et al. Endovascular Repair of Abdominal Aortic Aneurysm: Follow-up with Noninvasive Vascular Elastography in a Canine Model. Radiology. 2016;279(2):410-9.
29. Fromageau J, Lerouge S, Maurice RL, Soulez G, Cloutier G. Noninvasive vascular ultrasound elastography applied to the characterization of experimental aneurysms and follow-up after endovascular repair. Phys Med Biol. 2008;53(22):6475-90.
30. Bertrand-Grenier A, Lerouge S, Tang A, Salloum E, Therasse E, Kauffmann C, et al. Abdominal aortic aneurysm follow-up by shear wave elasticity imaging after endovascular repair in a canine model. Eur Radiol. 2017;27(5):2161-9.
31. Bertrand-Grenier A, Zehtabi F, Lerouge S, Alturkistani H, Kauffmann C, Bodson-Clermont P, et al. Shear wave elasticity imaging for residual endoleak and thrombus characterisation after endoleak embolisation following endovascular aneurysm repair: a canine animal study. Eur Radiol Exp. 2018;2(1):28.
32. Voizard N, Bertrand-Grenier A, Alturkistani H, Therasse E, Tang A, Kauffmann C, et al. Feasibility of shear wave sonoelastography to detect endoleak and evaluate thrombus organization after endovascular repair of abdominal aortic aneurysm. Eur Radiol. 2020;30:3879–89.
33. Bando Y, Kitase M, Shimohira M, Honda J, Furuta Y, Kasuya A, et al. 2D-shear wave elastography in the prediction of type II endoleaks after endovascular aneurysm repair. Minim Invasive Ther Allied Technol. 2019:1-6.
34. Guo Q, Du X, Zhao J, Ma Y, Huang B, Yuan D, et al. Prevalence and risk factors of type II endoleaks after endovascular aneurysm repair: A meta-analysis. PloS one. 2017;12(2):e0170600-e.
35. Abularrage CJ, Patel VI, Conrad MF, Schneider EB, Cambria RP, Kwolek CJ. Improved long-term results using Onyx glue for the treatment of persistent type 2 endoleak after endovascular aneurysm repair. J Vasc Surg. 2012;56(3):630-6.
36. Bryce Y, Schiro B, Cooper K, Ganguli S, Khayat M, Lam CK, et al. Type II endoleaks: diagnosis and treatment algorithm. Cardiovasc Diagn Ther. 2018;8(Suppl 1):S131-s7.
37. Massis K, Carson WG, 3rd, Rozas A, Patel V, Zwiebel B. Treatment of type II endoleaks with ethylene-vinyl-alcohol copolymer (Onyx). Vasc Endovascular Surg. 2012;46(3):251-7.

38. Muthu C, Maani J, Plank LD, Holden A, Hill A. Strategies to reduce the rate of type II endoleaks: routine intraoperative embolization of the inferior mesenteric artery and thrombin injection into the aneurysm sac. J Endovasc Ther. 2007;14(5):661-8.
39. Dayal R, Mousa A, Bernheim J, Hollenbeck S, Henderson P, Prince M, et al. Characterization of retrograde collateral (type II) endoleak using a new canine model. J Vasc Surg. 2004;40(5):985-94.
40. Lerouge S, Raymond J, Salazkin I, Qin Z, Gaboury L, Cloutier G, et al. Endovascular aortic aneurysm repair with stent-grafts: experimental models can reproduce endoleaks. J Vasc Interv Radiol. 2004;15(9):971-9.
41. Chabrot P, Fatimi A, Fraine PD, Ouchchane L, Dauplat MM, Rivard A, et al. Embolization and endothelial ablation with chitosan and sodium sotradecol sulfate: preliminary results in an animal model. J Endovasc Ther. 2012;19(3):439-49.
42. Fatimi A, Chabrot P, Berrahmoune S, Coutu JM, Soulez G, Lerouge S. A new injectable radiopaque chitosan-based sclerosing embolizing hydrogel for endovascular therapies. Acta Biomater. 2012;8(7):2712-21.
43. Zehtabi F, Dumont-Mackay V, Fatimi A, Bertrand-Grenier A, Heon H, Soulez G, et al. Chitosan-Sodium Tetradecyl Sulfate Hydrogel: Characterization and Preclinical Evaluation of a Novel Sclerosing Embolizing Agent for the Treatment of Endoleaks. Cardiovasc Intervent Radiol. 2017;40(4):576-84.
44. Standring S. Smooth muscle and the cardiovascular and lymphatic systems. In: Standring S, editor. Gray's Anatomy: The Anatomical Basis of Clinical Practice. 41 ed. London, UK: Elsevier; 2016. p. 123-40.e1.
45. Guven G, Hilty MP, Ince C. Microcirculation: Physiology, Pathophysiology, and Clinical Application. Blood purification. 2020;49(1-2):143-50.
46. Pappano AJ, Wier WG. Overview of the Circulation and Blood. In: Pappano AJ, Wier WG, editors. Cardiovascular Physiology. 11 ed. Philadelphia, PA: Elsevier; 2019. p. 1-9.
47. Ho SY, Sheppard MN. The aorta: embryology, anatomy, and pathology. In: Boudoulas H, Stefanadis C, editors. The aorta : structure, function, dysfunction, and diseases New York, New York: Informa Healthcare; 2008. p. 9-12.
48. Standring S. Posterior abdominal wall and retroperitoneum. In: Standring S, editor. Gray's Anatomy: The Anatomical Basis of Clinical Practice. 41 ed. London, UK: Elsevier; 2016. p. 1083-97.e2.
49. Standring S. Great vessels. In: Standring S, editor. Gray's Anatomy: The Anatomical Basis of Clinical Practice. London, UK: Elsevier; 2016. p. 1024-8.e2.
50. Hansen JT. Abdomen. In: Hansen JT, editor. Netter's Clinical Anatomy. 4 ed. Philadelphia, PA: Elsevier; 2019. p. 157-231.

51. Liddington MI, Heather BP. The relationship between aortic diameter and body habitus. Eur J Vasc Surg. 1992;6(1):89-92.
52. Carrell TW, Burnand KG, Wells GM, Clements JM, Smith A. Stromelysin-1 (matrix metalloproteinase-3) and tissue inhibitor of metalloproteinase-3 are overexpressed in the wall of abdominal aortic aneurysms. Circulation. 2002;105(4):477-82.
53. Mithieux SM, Weiss AS. Elastin. Adv Protein Chem. 2005;70:437-61.
54. Pappano AJ, Wier WG. The Arterial System. In: Pappano AJ, Wier WG, editors. Cardiovascular Physiology. Philadelphia, PA: Elsevier; 2019. p. 123-38.
55. Manuela G, Azevedo H, Malafaya P, Silva S, Oliveira J, Silva G, et al. Natural Polymers in Tissue Engineering Applications. In: Ebnesajjad S, editor. Handbook of Biopolymers and Biodegradable Plastics: Properties, Properties, and Applications. Plastics Design Library Handbook Series. Waltham, MA: William Andrew: Elsevier; 2013. p. 385-425.
56. Ahn SS, Rutherford RB, Johnston KW, May J, Veith FJ, Baker JD, et al. Reporting standards for infrarenal endovascular abdominal aortic aneurysm repair. Ad Hoc Committee for Standardized Reporting Practices in Vascular Surgery of The Society for Vascular Surgery/International Society for Cardiovascular Surgery. J Vasc Surg. 1997;25(2):405-10.
57. Creager MA, Elmore JG, Givens J. Screening for abdominal aortic aneurysm. In: Post TW, editor. Uptodate. Waltham, MA. 2020. (Accessed on June 29, 2020.)
58. Sakalihasan N, Limet R, Defawe OD. Abdominal aortic aneurysm. Lancet. 2005;365(9470):1577-89.
59. Massara M, Prunella R, Gerardi P, Lillo A, De Caridi G, Serra R, et al. Infrarenal Abdominal Aortic Pseudoaneurysm: Is It a Real Emergency? Ann Vasc Dis. 2017;10(4):423-5.
60. Marcu CB, Nijveldt R, Van Rossum AC. Unsuspected chronic traumatic aortic pseudoaneurysm--what to do about it. Late post-traumatic aortic pseudoaneurysm. Can J Cardiol. 2008;24(2):143-4.
61. Vlachou PA, Karkos CD, Bains S, McCarthy MJ, Fishwick G, Bolia A. Percutaneous ultrasound-guided thrombin injection for the treatment of iatrogenic femoral artery pseudoaneurysms. Eur J Radiol. 2011;77(1):172-4.
62. Kim CS, Choi YH, So YH, Choi J-S. A Spontaneous Abdominal Aortic Pseudoaneurysm Treated with N-butyl Cyanoacrylate and Coil Embolization: A Case Report. Ann Cardiothorac Surg. 2018;24(1):43-6.
63. Jesinger RA, Thoreson AA, Lamba R. Abdominal and pelvic aneurysms and pseudoaneurysms: imaging review with clinical, radiologic, and treatment correlation. Radiographics. 2013;33(3):E71-E96.
64. Forsdahl SH, Singh K, Solberg S, Jacobsen BK. Risk factors for abdominal aortic aneurysms: a 7-year prospective study: the Tromso Study, 1994-2001. Circulation. 2009;119(16):2202-8.

65. Singh K, Bønaa KH, Jacobsen BK, Bjørk L, Solberg S. Prevalence of and risk factors for abdominal aortic aneurysms in a population-based study : The Tromsø Study. Am J Epidemiol. 2001;154(3):236-44.
66. Norman PE, Powell JT. Abdominal aortic aneurysm: the prognosis in women is worse than in men. Circulation. 2007;115(22):2865-9.
67. Lee A, Dake MD. Abdominal and Thoracic Aortic Aneurysms. In: Keefe N, Haskal Z, Park A, Angle J, editors. IR Playbook: Springer, Cham; 2018. p. 197-207.
68. Owens DK, Davidson KW, Krist AH, Barry MJ, Cabana M, Caughey AB, et al. Screening for Abdominal Aortic Aneurysm: US Preventive Services Task Force Recommendation Statement. JAMA. 2019;322(22):2211-8.
69. Svensjö S, Björck M, Gürtelschmid M, Djavani Gidlund K, Hellberg A, Wanhainen A. Low prevalence of abdominal aortic aneurysm among 65-year-old Swedish men indicates a change in the epidemiology of the disease. Circulation. 2011;124(10):1118-23.
70. Lederle FA, Johnson GR, Wilson SE, Chute EP, Hye RJ, Makaroun MS, et al. The aneurysm detection and management study screening program: validation cohort and final results. Aneurysm Detection and Management Veterans Affairs Cooperative Study Investigators. Arch Intern Med. 2000;160(10):1425-30.
71. Lemaître V, Dabo AJ, D'Armiento J. Cigarette smoke components induce matrix metalloproteinase-1 in aortic endothelial cells through inhibition of mTOR signaling. Toxicol Sci. 2011;123(2):542-9.
72. Thompson RW. Basic science of abdominal aortic aneurysms: emerging therapeutic strategies for an unresolved clinical problem. Curr Opin Cardiol. 1996;11(5):504-18.
73. Sakalihasan N, Defraigne JO, Kerstenne MA, Cheramy-Bien JP, Smelser DT, Tromp G, et al. Family members of patients with abdominal aortic aneurysms are at increased risk for aneurysms: analysis of 618 probands and their families from the Liège AAA Family Study. Ann Vasc Surg. 2014;28(4):787-97.
74. Wahlgren CM, Larsson E, Magnusson PK, Hultgren R, Swedenborg J. Genetic and environmental contributions to abdominal aortic aneurysm development in a twin population. J Vasc Surg. 2010;51(1):3-7; discussion
75. Kontusaari S, Tromp G, Kuivaniemi H, Ladda RL, Prockop DJ. Inheritance of an RNA splicing mutation (G+ 1 IVS20) in the type III procollagen gene (COL3A1) in a family having aortic aneurysms and easy bruisability: phenotypic overlap between familial arterial aneurysms and Ehlers-Danlos syndrome type IV. Am J Hum Genet. 1990;47(1):112-20.
76. Verloes A, Sakalihasan N, Koulischer L, Limet R. Aneurysms of the abdominal aorta: familial and genetic aspects in three hundred thirteen pedigrees. J Vasc Surg. 1995;21(4):646-55.
77. Kuivaniemi H, Ryer EJ, Elmore JR, Tromp G. Understanding the pathogenesis of abdominal aortic aneurysms. Expert Rev Cardiovasc Ther. 2015;13(9):975-87.

78. Hagerty T, Geraghty P, Braverman AC. Abdominal Aortic Aneurysm in Marfan Syndrome. Ann Vasc Surg. 2017;40:294.e1-.e6.
79. Cury M, Zeidan F, Lobato AC. Aortic disease in the young: genetic aneurysm syndromes, connective tissue disorders, and familial aortic aneurysms and dissections. Int J Vasc. 2013;2013:267215-.
80. Reed D, Reed C, Stemmermann G, Hayashi T. Are aortic aneurysms caused by atherosclerosis? Circulation. 1992;85(1):205-11.
81. Shah PK. Inflammation, metalloproteinases, and increased proteolysis: an emerging pathophysiological paradigm in aortic aneurysm. Circulation. 1997;96(7):2115-7.
82. Freestone T, Turner RJ, Coady A, Higman DJ, Greenhalgh RM, Powell JT. Inflammation and matrix metalloproteinases in the enlarging abdominal aortic aneurysm. Arterioscler Thromb Vasc Biol. 1995;15(8):1145-51.
83. Chung J, Eidt JF, Mills JL, Creager MA, Collins KA. Epidemiology, risk factors, pathogenesis, and natural history of abdominal aortic aneurysm. In: Post TW, editor. UpToDate. Waltham, MA. 2020. (Accessed on May 20, 2020.)
84. Dobrin PB, Mrkvicka R. Failure of elastin or collagen as possible critical connective tissue alterations underlying aneurysmal dilatation. Cardiovasc Surg. 1994;2(4):484-8.
85. Perlstein TS, Lee RT. Smoking, metalloproteinases, and vascular disease. Arterioscler Thromb Vasc Biol. 2006;26(2):250-6.
86. Wu XF, Zhang J, Paskauskas S, Xin SJ, Duan ZQ. The role of estrogen in the formation of experimental abdominal aortic aneurysm. Am J Surg. 2009;197(1):49-54.
87. Hirsch AT, Haskal ZJ, Hertzer NR, Bakal CW, Creager MA, Halperin JL, et al. ACC/AHA 2005 Practice Guidelines for the management of patients with peripheral arterial disease (lower extremity, renal, mesenteric, and abdominal aortic): a collaborative report from the American Association for Vascular Surgery/Society for Vascular Surgery, Society for Cardiovascular Angiography and Interventions, Society for Vascular Medicine and Biology, Society of Interventional Radiology, and the ACC/AHA Task Force on Practice Guidelines (Writing Committee to Develop Guidelines for the Management of Patients With Peripheral Arterial Disease): endorsed by the American Association of Cardiovascular and Pulmonary Rehabilitation; National Heart, Lung, and Blood Institute; Society for Vascular Nursing; TransAtlantic Inter-Society Consensus; and Vascular Disease Foundation. Circulation. 2006;113(11):e463-654.
88. Vorp DA, Vande Geest JP. Biomechanical determinants of abdominal aortic aneurysm rupture. Arterioscler Thromb Vasc Biol. 2005;25(8):1558-66.
89. Jim J, Thompson RW, Mills JL, Eidt JF, Creager MA, Collins KA. Clinical features and diagnosis of abdominal aortic aneurysm. In: Post TW, editor. UpToDate. Waltham, MA. 2020. (Accessed on June 29, 2020.)

90. Vu K-N, Kaitoukov Y, Morin-Roy F, Kauffmann C, Giroux M-F, Thérasse E, et al. Rupture signs on computed tomography, treatment, and outcome of abdominal aortic aneurysms. Insights Imaging. 2014;5(3):281-93.

91. Lederle FA, Johnson GR, Wilson SE, Ballard DJ, Jordan WD, Jr., Blebea J, et al. Rupture rate of large abdominal aortic aneurysms in patients refusing or unfit for elective repair. JAMA. 2002;287(22):2968-72.

92. Brewster DC, Cronenwett JL, Hallett JW, Jr., Johnston KW, Krupski WC, Matsumura JS. Guidelines for the treatment of abdominal aortic aneurysms. Report of a subcommittee of the Joint Council of the American Association for Vascular Surgery and Society for Vascular Surgery. J Vasc Surg. 2003;37(5):1106-17.

93. Brady AR, Thompson SG, Fowkes FG, Greenhalgh RM, Powell JT. Abdominal aortic aneurysm expansion: risk factors and time intervals for surveillance. Circulation. 2004;110(1):16-21.

94. McPhee JT, Hill JS, Eslami MH. The impact of gender on presentation, therapy, and mortality of abdominal aortic aneurysm in the United States, 2001-2004. J Vasc Surg. 2007;45(5):891-9.

95. Hollier LH, Taylor LM, Ochsner J. Recommended indications for operative treatment of abdominal aortic aneurysms. Report of a subcommittee of the Joint Council of the Society for Vascular Surgery and the North American Chapter of the International Society for Cardiovascular Surgery. J Vasc Surg. 1992;15(6):1046-56.

96. Nathan DP, Xu C, Pouch AM, Chandran KB, Desjardins B, Gorman JH, 3rd, et al. Increased wall stress of saccular versus fusiform aneurysms of the descending thoracic aorta. Ann Vasc Surg. 2011;25(8):1129-37.

97. Shang EK, Nathan DP, Boonn WW, Lys-Dobradin IA, Fairman RM, Woo EY, et al. A modern experience with saccular aortic aneurysms. J Vasc Surg. 2013;57(1):84-8.

98. United States Preventive Services Task Force. Screening for Abdominal Aortic Aneurysm: US Preventive Services Task Force Recommendation Statement. JAMA. 2019;322(22):2211-8.

99. Fink HA, Lederle FA, Roth CS, Bowles CA, Nelson DB, Haas MA. The accuracy of physical examination to detect abdominal aortic aneurysm. Arch Intern Med. 2000;160(6):833-6.

100. van Walraven C, Wong J, Morant K, Jennings A, Jetty P, Forster AJ. Incidence, follow-up, and outcomes of incidental abdominal aortic aneurysms. J Vasc Surg. 2010;52(2):282-9.e1-2.

101. Cambria RA, Gloviczki P, Stanson AW, Cherry KJ, Jr., Hallett JW, Jr., Bower TC, et al. Symptomatic, nonruptured abdominal aortic aneurysms: are emergent operations necessary? Ann Vasc Surg. 1994;8(2):121-6.

102. Baxter BT, McGee GS, Flinn WR, McCarthy WJ, Pearce WH, Yao JS. Distal embolization as a presenting symptom of aortic aneurysms. Am J Surg. 1990;160(2):197-201.

103. United States Preventive Services Task Force. Screening for abdominal aortic aneurysm: recommendation statement. Ann Intern Med. 2005;142(3):198-202.
104. Chaikof EL, Brewster DC, Dalman RL, Makaroun MS, Illig KA, Sicard GA, et al. The care of patients with an abdominal aortic aneurysm: the Society for Vascular Surgery practice guidelines. J Vasc Surg. 2009;50(4 Suppl):S2-49.
105. Guirguis-Blake JM, Beil TL, Senger CA, Coppola EL. Primary Care Screening for Abdominal Aortic Aneurysm: Updated Evidence Report and Systematic Review for the US Preventive Services Task Force. JAMA. 2019;322(22):2219-38.
106. Schermerhorn ML, O'Malley AJ, Jhaveri A, Cotterill P, Pomposelli F, Landon BE. Endovascular vs. open repair of abdominal aortic aneurysms in the Medicare population. N Engl J Med. 2008;358(5):464-74.
107. Eidt JF, Mills JL, Collins KA. Open surgical repair of abdominal aortic aneurysm. In: Post TW, editor. UpToDate. Waltham, MA. 2020. (Accessed on May 20, 2020.)
108. Schermerhorn ML, Buck DB, O'Malley AJ, Curran T, McCallum JC, Darling J, et al. Long-Term Outcomes of Abdominal Aortic Aneurysm in the Medicare Population. N Engl J Med. 2015;373(4):328-38.
109. Kent KC. Clinical practice. Abdominal aortic aneurysms. N Engl J Med. 2014;371(22):2101-8.
110. Yamanouchi D, Matsumura J. Abdominal Aortic Aneurysms. In: Geschwind JFH, Dake MD, editors. Abrams' Angiography: Interventional Radiology. 3 ed. Philadelphia, PA: Lippincott Williams & Wilkins, Walters Kluwer; 2014. p. 677-85.
111. Becquemin JP, Pillet JC, Lescalie F, Sapoval M, Goueffic Y, Lermusiaux P, et al. A randomized controlled trial of endovascular aneurysm repair versus open surgery for abdominal aortic aneurysms in low- to moderate-risk patients. J Vasc Surg. 2011;53(5):1167-73 e1.
112. Badger S, Forster R, Blair PH, Ellis P, Kee F, Harkin DW. Endovascular treatment for ruptured abdominal aortic aneurysm. Cochrane Database Syst Rev. 2017;5(5):Cd005261.
113. Chambers D, Epstein D, Walker S, Fayter D, Paton F, Wright K, et al. Endovascular stents for abdominal aortic aneurysms: a systematic review and economic model. Health Technol Assess. 2009;13(48):1-189, 215-318, iii.
114. Epstein D, Sculpher MJ, Powell JT, Thompson SG, Brown LC, Greenhalgh RM. Long-term cost-effectiveness analysis of endovascular versus open repair for abdominal aortic aneurysm based on four randomized clinical trials. Br J Surg. 2014;101(6):623-31.
115. van Bochove CA, Burgers LT, Vahl AC, Birnie E, van Schothorst MG, Redekop WK. Cost-effectiveness of open versus endovascular repair of abdominal aortic aneurysm. J Vasc Surg. 2016;63(3):827-38.e2.
116. White GH, Yu W, May J. Endoleak--a proposed new terminology to describe incomplete aneurysm exclusion by an endoluminal graft. J Endovasc Surg. 1996;3(1):124-5.

117. Stavropoulos SW, Charagundla SR. Imaging techniques for detection and management of endoleaks after endovascular aortic aneurysm repair. Radiology. 2007;243(3):641-55.
118. Bashir MR, Ferral H, Jacobs C, McCarthy W, Goldin M. Endoleaks after endovascular abdominal aortic aneurysm repair: management strategies according to CT findings. AJR Am J Roentgenol. 2009;192(4):W178-86.
119. Ellozy SH, Carroccio A, Lookstein RA, Minor ME, Sheahan CM, Juta J, et al. First experience in human beings with a permanently implantable intrasac pressure transducer for monitoring endovascular repair of abdominal aortic aneurysms. J Vasc Surg. 2004;40(3):405-12.
120. Tolia AJ, Landis R, Lamparello P, Rosen R, Macari M. Type II endoleaks after endovascular repair of abdominal aortic aneurysms: natural history. Radiology. 2005;235(2):683-6.
121. Jones JE, Atkins MD, Brewster DC, Chung TK, Kwolek CJ, LaMuraglia GM, et al. Persistent type 2 endoleak after endovascular repair of abdominal aortic aneurysm is associated with adverse late outcomes. J Vasc Surg. 2007;46(1):1-8.
122. Veith FJ, Baum RA, Ohki T, Amor M, Adiseshiah M, Blankensteijn JD, et al. Nature and significance of endoleaks and endotension: summary of opinions expressed at an international conference. J Vasc Surg. 2002;35(5):1029-35.
123. Huda W, Abrahams RB. CT I. Review of Radiological Physics. 4 ed. Philedelphia, PA: Wolters Kluwer; 2016. p. 147-58.
124. Bae KT. Intravenous contrast medium administration and scan timing at CT: considerations and approaches. Radiology. 2010;256(1):32-61.
125. Allisy-Roberts P, Williams J. Computed tomography. Farr's Physics for Medical Imaging. 2 ed. Edinburgh, Scotland: Saunders/Elsevier; 2008. p. 103-19.
126. Stavropoulos SW, Clark TW, Carpenter JP, Fairman RM, Litt H, Velazquez OC, et al. Use of CT angiography to classify endoleaks after endovascular repair of abdominal aortic aneurysms. J Vasc Interv Radiol. 2005;16(5):663-7.
127. Bryce Y, Rogoff P, Romanelli D, Reichle R. Endovascular repair of abdominal aortic aneurysms: vascular anatomy, device selection, procedure, and procedure-specific complications. Radiographics. 2015;35(2):593-615.
128. Huda W, Abrahams RB. Magnetic Resonance I. Review of Radiology Physics. 4 ed. Philadelphia, PA: Wolters Kluwer; 2016. p. 205-16.
129. Huda W, Abrahams RB. Magnetic Resonance II. Review of Radiology Physis. 4 ed. Philadelphia, PA: Wolters Kluwer; 2016. p. 221-33.
130. Pitton MB, Schweitzer H, Herber S, Schmiedt W, Neufang A, Kalden P, et al. MRI versus helical CT for endoleak detection after endovascular aneurysm repair. Am J Roentgenol. 2005;185(5):1275-81.

131. van der Laan MJ, Bartels LW, Viergever MA, Blankensteijn JD. Computed tomography versus magnetic resonance imaging of endoleaks after EVAR. Eur J Vasc Endovasc Surg. 2006;32(4):361-5.
132. van der Laan MJ, Bakker CJ, Blankensteijn JD, Bartels LW. Dynamic CE-MRA for endoleak classification after endovascular aneurysm repair. Eur J Vasc Endovasc Surg. 2006;31(2):130-5.
133. Huda W, Abrahams RB. Ultrasound I. Review of Radiologic Physics. 4 ed. Philadelphia, PA: Wolters Kluwer; 2016. p. 237-48.
134. Huda W, Abrahams RB. Ultrasound II. Review of Radiology Physics. 4 ed. Philadelphia, PA: Wolters Kluwer; 2016. p. 251-60.
135. Samei E, Peck DJ. Ultrasonography. Hendee's Physics of Medical Imaging. 5 ed. Hoboken, NJ.: John Wiley & Sons, Inc.; 2019. p. 305-38.
136. Han SM, Patel K, Rowe VL, Perese S, Bond A, Weaver FA. Ultrasound-determined diameter measurements are more accurate than axial computed tomography after endovascular aortic aneurysm repair. J Vasc Surg. 2010;51(6):1381-7; discussion 7-9.
137. Beeman BR, Murtha K, Doerr K, McAfee-Bennett S, Dougherty MJ, Calligaro KD. Duplex ultrasound factors predicting persistent type II endoleak and increasing AAA sac diameter after EVAR. J Vasc Surg. 2010;52(5):1147-52.
138. Schmieder GC, Stout CL, Stokes GK, Parent FN, Panneton JM. Endoleak after endovascular aneurysm repair: duplex ultrasound imaging is better than computed tomography at determining the need for intervention. J Vasc Surg. 2009;50(5):1012-7; discussion 7-8.
139. Cantisani V, Ricci P, Grazhdani H, Napoli A, Fanelli F, Catalano C, et al. Prospective comparative analysis of colour-Doppler ultrasound, contrast-enhanced ultrasound, computed tomography and magnetic resonance in detecting endoleak after endovascular abdominal aortic aneurysm repair. Eur J Vasc Endovasc Surg. 2011;41(2):186-92.
140. Hangiandreou NJ. AAPM/RSNA physics tutorial for residents. Topics in US: B-mode US: basic concepts and new technology. Radiographics. 2003;23(4):1019-33.
141. Elkouri S, Panneton JM, Andrews JC, Lewis BD, McKusick MA, Noel AA, et al. Computed tomography and ultrasound in follow-up of patients after endovascular repair of abdominal aortic aneurysm. Ann Vasc Surg. 2004;18(3):271-9.
142. AbuRahma AF, Welch CA, Mullins BB, Dyer B. Computed tomography versus color duplex ultrasound for surveillance of abdominal aortic stent-grafts. J Endovasc Ther. 2005;12(5):568-73.
143. Mirza TA, Karthikesalingam A, Jackson D, Walsh SR, Holt PJ, Hayes PD, et al. Duplex ultrasound and contrast-enhanced ultrasound versus computed tomography for the detection of endoleak after EVAR: systematic review and bivariate meta-analysis. Eur J Vasc Endovasc Surg. 2010;39(4):418-28.

144. Millen A, Canavati R, Harrison G, McWilliams RG, Wallace S, Vallabhaneni SR, et al. Defining a role for contrast-enhanced ultrasound in endovascular aneurysm repair surveillance. J Vasc Surg. 2013;58(1):18-23.
145. Wilson SR, Greenbaum LD, Goldberg BB. Contrast-enhanced ultrasound: what is the evidence and what are the obstacles? Am J Roentgenol. 2009;193(1):55-60.
146. Chen J, Stavropoulos SW. Management of Endoleaks. Semin Intervent Radiol. 2015;32(3):259-64.
147. Maldonado TS, Rosen RJ, Rockman CB, Adelman MA, Bajakian D, Jacobowitz GR, et al. Initial successful management of type I endoleak after endovascular aortic aneurysm repair with n-butyl cyanoacrylate adhesive. J Vasc Surg. 2003;38(4):664-70.
148. Kray J, Kirk S, Franko J, Chew DK. Role of type II endoleak in sac regression after endovascular repair of infrarenal abdominal aortic aneurysms. J Vasc Surg. 2015;61(4):869-74.
149. Pineda DM, Calligaro KD, Tyagi S, Troutman DA, Dougherty MJ. Late type II endoleaks after endovascular aneurysm repair require intervention more frequently than early type II endoleaks. J Vasc Surg. 2018;67(2):449-52.
150. Karthikesalingam A, Thrumurthy SG, Jackson D, Choke E, Sayers RD, Loftus IM, et al. Current evidence is insufficient to define an optimal threshold for intervention in isolated type II endoleak after endovascular aneurysm repair. J Endovasc Ther. 2012;19(2):200-8.
151. Steinmetz E, Rubin BG, Sanchez LA, Choi ET, Geraghty PJ, Baty J, et al. Type II endoleak after endovascular abdominal aortic aneurysm repair: a conservative approach with selective intervention is safe and cost-effective. J Vasc Surg. 2004;39(2):306-13.
152. Gelfand DV, White GH, Wilson SE. Clinical significance of type II endoleak after endovascular repair of abdominal aortic aneurysm. Ann Vasc Surg. 2006;20(1):69-74.
153. Abularrage CJ, Crawford RS, Conrad MF, Lee H, Kwolek CJ, Brewster DC, et al. Preoperative variables predict persistent type 2 endoleak after endovascular aneurysm repair. J Vasc Surg. 2010;52(1):19-24.
154. Stavropoulos SW, Park J, Fairman R, Carpenter J. Type 2 endoleak embolization comparison: translumbar embolization versus modified transarterial embolization. J Vasc Interv Radiol. 2009;20(10):1299-302.
155. Baum RA, Carpenter JP, Golden MA, Velazquez OC, Clark TW, Stavropoulos SW, et al. Treatment of type 2 endoleaks after endovascular repair of abdominal aortic aneurysms: comparison of transarterial and translumbar techniques. J Vasc Surg. 2002;35(1):23-9.
156. Sheehan MK, Barbato J, Compton CN, Zajko A, Rhee R, Makaroun MS. Effectiveness of coiling in the treatment of endoleaks after endovascular repair. J Vasc Surg. 2004;40(3):430-4.

157. Jamieson RW, Bachoo P, Tambyraja AL. Evidence for Ethylene-Vinyl-Alcohol-Copolymer Liquid Embolic Agent as a Monotherapy in Treatment of Endoleaks. Eur J Vasc Endovasc Surg. 2016;51(6):810-4.
158. Gorlitzer M, Mertikian G, Trnka H, Froeschl A, Meinhart J, Weiss G, et al. Translumbar treatment of type II endoleaks after endovascular repair of abdominal aortic aneurysm. Interact Cardiovasc Thorac Surg. 2008;7(5):781-4.
159. Binkert CA, Alencar H, Singh J, Baum RA. Translumbar type II endoleak repair using angiographic CT. J Vasc Interv Radiol. 2006;17(8):1349-53.
160. Khaja MS, Park AW, Swee W, Evans AJ, Fritz Angle J, Turba UC, et al. Treatment of Type II Endoleak Using Onyx With Long-Term Imaging Follow-Up. Cardiovasc Intervent Radiol. 2014;37(3):613-22
161. Scali ST, Vlada A, Chang CK, Beck AW. Transcaval embolization as an alternative technique for the treatment of type II endoleak after endovascular aortic aneurysm repair. J Vasc Surg. 2013;57(3):869-74.
162. Wee I, Marjot T, Patel K, Bhrugubanda V, Choong A. Laparoscopic ligation of Type II endoleaks following endovascular aneurysm repair: A systematic review. Vascular. 2018;26(6):657-69.
163. Walker SR, Macierewicz J, Hopkinson BR. Endovascular AAA repair: prevention of side branch endoleaks with thrombogenic sponge. J Endovasc Surg. 1999;6(4):350-3.
164. Axelrod DJ, Lookstein RA, Guller J, Nowakowski FS, Ellozy S, Carroccio A, et al. Inferior mesenteric artery embolization before endovascular aneurysm repair: technique and initial results. J Vasc Interv Radiol. 2004;15(11):1263-7.
165. Ronsivalle S, Faresin F, Franz F, Rettore C, Zanchetta M, Olivieri A. Aneurysm sac "thrombization" and stabilization in EVAR: a technique to reduce the risk of type II endoleak. J Endovasc Ther. 2010;17(4):517-24.
166. Gould DA, McWilliams R, Edwards RD, Martin J, White D, Joekes E, et al. Aortic side branch embolization before endovascular aneurysm repair: incidence of type II endoleak. J Vasc Interv Radiol. 2001;12(3):337-41.
167. Sarac TP, Gibbons C, Vargas L, Liu J, Srivastava S, Bena J, et al. Long-term follow-up of type II endoleak embolization reveals the need for close surveillance. J Vasc Surg. 2012;55(1):33-40.
168. Stavropoulos SW, Kim H, Clark TW, Fairman RM, Velazquez O, Carpenter JP. Embolization of type 2 endoleaks after endovascular repair of abdominal aortic aneurysms with use of cyanoacrylate with or without coils. J Vasc Interv Radiol. 2005;16(6):857-61.
169. Raymond J, Guilbert F, Gevry G, Salazkin I, Robledo O. Role of the endothelial lining in recurrences after coil embolization: prevention of recanalization by endothelial denudation. Stroke. 2004;35:1471-5.

170. Soulez G, Lerouge S, Darsaut T, Salazkin I, Oliva VL, Raymond J. Role of the endothelial lining in endoleak formation and persistence after endovascular repair of aneurysm. J Vasc Interv Radiol. 2008;19(7):1070-8.
171. Soulez G, Lerouge S, Salazkin I, Darsaut T, Oliva VL, Raymond J. Type I and collateral flow in experimental aneurysm models treated with stent-grafts. J Vasc Interv Radiol. 2007;18(2):265-72.
172. Lerouge S, Bonneviot MC, Salazkin I, Raymond J, Soulez G. Endothelial denudation combined with embolization in the prevention of endoleaks after endovascular aneurysm repair: an animal study. J Endovasc Ther. 2011;18(5):686-96.
173. Kumar MNVR. A review of chitin and chitosan applications. React Funct Polym. 2000;46(1):1-27.
174. Zhou HY, Jiang LJ, Cao PP, Li JB, Chen XG. Glycerophosphate-based chitosan thermosensitive hydrogels and their biomedical applications. Carbohydr Polym. 2015;117:524-36.
175. Ganji F, Abdekhodaie M, SA AR. Gelation time and degradation rate of chitosan-based injectable hydrogel. J Solgel Sci Technol. 2007;42(1):47-53.
176. Albanese G, Kondo KL. Pharmacology of sclerotherapy. Semin Intervent Rad. 2010;27(4):391-9.
177. Fatimi A, Zehtabi F, Lerouge S. Optimization and characterization of injectable chitosan-iodixanol-based hydrogels for the embolization of blood vessels. J Biomed Mater Res B Appl Biomater. 2016;104(8):1551-1562
178. Ophir J, Alam SK, Garra B, Kallel F, Konofagou E, Krouskop T, et al. Elastography: Ultrasonic estimation and imaging of the elastic properties of tissues. Proc Inst Mech Eng H. 1999;213(3):203-33.
179. Gennisson JL, Deffieux T, Fink M, Tanter M. Ultrasound elastography: principles and techniques. Diagn Interv Imaging. 2013;94(5):487-95.
180. Sigrist RMS, Liau J, Kaffas AE, Chammas MC, Willmann JK. Ultrasound Elastography: Review of Techniques and Clinical Applications. Theranostics. 2017;7(5):1303-29.
181. Nightingale K, Bentley R, Trahey G. Observations of tissue response to acoustic radiation force: opportunities for imaging. Ultrason Imaging. 2002;24(3):129-38.
182. Mercure E, Cloutier G, Schmitt C, Maurice RL. Performance evaluation of different implementations of the Lagrangian speckle model estimator for non-invasive vascular ultrasound elastography. Med Phys. 2008;35(7):3116-26.
183. Sarvazyan AP, Rudenko OV, Swanson SD, Fowlkes JB, Emelianov SY. Shear wave elasticity imaging: a new ultrasonic technology of medical diagnostics. Ultrasound Med Biol. 1998;24(9):1419-35.
184. Jiang Y, Li GY, Qian LX, Hu XD, Liu D, Liang S, et al. Characterization of the nonlinear elastic properties of soft tissues using the supersonic shear imaging (SSI) technique: inverse method, ex vivo and in vivo experiments. Med Image Anal. 2015;20(1):97-111.
185. Varghese T. Quasi-Static Ultrasound Elastography. Ultrasound clinics. 2009;4(3):323-38.

186. Dietrich CF, Barr RG, Farrokh A, Dighe M, Hocke M, Jenssen C, et al. Strain Elastography - How To Do It? Ultrasound Int Open. 2017;3(4):E137-E49.
187. Doyley MM, Parker KJ. Elastography: general principles and clincial applications. Ultrasound Clinics. 2014;9(1):1-11.
188. Carlsen JF, Pedersen MR, Ewertsen C, Săftoiu A, Lönn L, Rafaelsen SR, et al. A comparative study of strain and shear-wave elastography in an elasticity phantom. Am J Roentgenol. 2015;204(3):W236-42.
189. Barr RG, Nakashima K, Amy D, Cosgrove D, Farrokh A, Schafer F, et al. WFUMB guidelines and recommendations for clinical use of ultrasound elastography: Part 2: breast. Ultrasound Med Biol. 2015;41(5):1148-60.
190. Cosgrove D, Barr R, Bojunga J, Cantisani V, Chammas MC, Dighe M, et al. WFUMB Guidelines and Recommendations on the Clinical Use of Ultrasound Elastography: Part 4. Thyroid. Ultrasound Med Biol. 2017;43(1):4-26.
191. Cosgrove D, Piscaglia F, Bamber J, Bojunga J, Correas JM, Gilja OH, et al. EFSUMB guidelines and recommendations on the clinical use of ultrasound elastography. Part 2: Clinical applications. Ultraschall Med. 2013;34(3):238-53.
192. Varghese T, Zagzebski JA, Frank G, Madsen EL. Elastographic imaging using a handheld compressor. Ultrason Imaging. 2002;24(1):25-35.
193. Varghese T, Ophir J, Céspedes I. Noise reduction in elastograms using temporal stretching with multicompression averaging. Ultrasound Med Biol. 1996;22(8):1043-52.
194. Hall TJ, Zhu Y, Spalding CS. In vivo real-time freehand palpation imaging. Ultrasound Med Biol. 2003;29(3):427-35.
195. Hu X, Shao J, Bai J, Wang J, Qian L. New noninvasive assessment of liver fibrosis in chronic hepatitis B: maximal accumulative respiration strain. J Ultrasound Med. 2010;29(8):1213-21.
196. Bae U, Dighe M, Dubinsky T, Minoshima S, Shamdasani V, Kim Y. Ultrasound thyroid elastography using carotid artery pulsation: preliminary study. J Ultrasound Med. 2007;26(6):797-805.
197. Varghese T, Zagzebski JA, Rahko P, Breburda CS. Ultrasonic imaging of myocardial strain using cardiac elastography. Ultrason Imaging. 2003;25(1):1-16.
198. Roy Cardinal MH, Heusinkveld MHG, Qin Z, Lopata RGP, Naim C, Soulez G, et al. Carotid Artery Plaque Vulnerability Assessment Using Noninvasive Ultrasound Elastography: Validation With MRI. AJR Am J Roentgenol. 2017;209(1):142-51.
199. Nightingale KR, Palmeri ML, Nightingale RW, Trahey GE. On the feasibility of remote palpation using acoustic radiation force. J Acoust Soc Am. 2001;110(1):625-34.
200. Li G-Y, Cao Y. Mechanics of ultrasound elastography. Proceedings Mathematical, physical, and engineering sciences. 2017;473(2199):20160841-.

201. Yamakoshi Y, Sato J, Sato T. Ultrasonic imaging of internal vibration of soft tissue under forced vibration. IEEE Trans Ultrason Ferroelectr Freq Control. 1990;37(2):45-53.
202. Parker KJ, Huang SR, Musulin RA, Lerner RM. Tissue response to mechanical vibrations for "sonoelasticity imaging". Ultrasound Med Biol. 1990;16(3):241-6.
203. Henni AH, Schmitt C, Cloutier G. Shear wave induced resonance elastography of soft heterogeneous media. J Biomech. 2010;43(8):1488-93.
204. Fatemi M, Greenleaf JF. Ultrasound-stimulated vibro-acoustic spectrography. Science. 1998;280(5360):82-5.
205. Konofagou EE, Hynynen K. Localized harmonic motion imaging: theory, simulations and experiments. Ultrasound Med Biol. 2003;29(10):1405-13.
206. Sandrin L, Tanter M, Catheline S, Fink M. Shear modulus imaging with 2-D transient elastography. IEEE Trans Ultrason Ferroelectr Freq Control. 2002;49(4):426-35.
207. Catheline S, Thomas J, Wu F, Fink MA. Diffraction field of a low frequency vibrator in soft tissues using transient elastography. IEEE Transactions on Ultrasonics, Ferroelectrics, and Frequency Control. 1999;46(4):1013-9.
208. Sandrin L, Tanter M, Gennisson JL, Catheline S, Fink M. Shear elasticity probe for soft tissues with 1-D transient elastography. IEEE Trans Ultrason Ferroelectr Freq Control. 2002;49(4):436-46.
209. Foucher J, Chanteloup E, Vergniol J, Castéra L, Le Bail B, Adhoute X, et al. Diagnosis of cirrhosis by transient elastography (FibroScan): a prospective study. Gut. 2006;55(3):403-8.
210. Bercoff J, Tanter M, Fink M. Supersonic shear imaging: a new technique for soft tissue elasticity mapping. IEEE Trans Ultrason Ferroelectr Freq Control. 2004;51(4):396-409.
211. Palmeri ML, Wang MH, Dahl JJ, Frinkley KD, Nightingale KR. Quantifying hepatic shear modulus in vivo using acoustic radiation force. Ultrasound Med Biol. 2008;34(4):546-58.
212. Taljanovic MS, Gimber LH, Becker GW, Latt LD, Klauser AS, Melville DM, et al. Shear-Wave Elastography: Basic Physics and Musculoskeletal Applications. Radiographics. 2017;37(3):855-70.
213. Nightingale K, McAleavey S, Trahey G. Shear-wave generation using acoustic radiation force: in vivo and ex vivo results. Ultrasound Med Biol. 2003;29(12):1715-23.
214. Mahmood B, Ewertsen C, Carlsen J, Nielsen MB. Ultrasound Vascular Elastography as a Tool for Assessing Atherosclerotic Plaques - A Systematic Literature Review. Ultrasound Int Open. 2016;2(4):E106-E12.
215. Keshavarz-Motamed Z, Saijo Y, Majdouline Y, Riou L, Ohayon J, Cloutier G. Coronary artery atherectomy reduces plaque shear strains: an endovascular elastography imaging study. Atherosclerosis. 2014;235(1):140-9.

216. de Korte CL, van der Steen AF. Intravascular ultrasound elastography: an overview. Ultrasonics. 2002;40(1-8):859-65.
217. De Korte C, Carlier S, Mastik F, Doyley M, Van Der Steen A, Serruys P, et al. Morphological and mechanical information of coronary arteries obtained with intravascular elastography. Feasibility study in vivo. Eur Heart J. 2002;23(5):405-13.
218. Maurice RL, Brusseau E, Finet G, Cloutier G. On the potential of the Lagrangian speckle model estimator to characterize atherosclerotic plaques in endovascular elastography: in vitro experiments using an excised human carotid artery. Ultrasound Med Biol. 2005;31(1):85-91.
219. Ramnarine KV, Garrard JW, Dexter K, Nduwayo S, Panerai RB, Robinson TG. Shear wave elastography assessment of carotid plaque stiffness: in vitro reproducibility study. Ultrasound Med Biol. 2014;40(1):200-9.
220. Dahl JJ, Dumont DM, Allen JD, Miller EM, Trahey GE. Acoustic radiation force impulse imaging for noninvasive characterization of carotid artery atherosclerotic plaques: a feasibility study. Ultrasound Med Biol. 2009;35(5):707-16.
221. Takimura H, Hirano K, Muramatsu T, Tsukahara R, Ito Y, Sakai T, et al. Vascular elastography: a novel method to characterize occluded lower limb arteries prior to endovascular therapy. J Endovasc Ther. 2014;21(5):654-61.
222. Maurice RL, Daronat M, Ohayon J, Stoyanova E, Foster FS, Cloutier G. Non-invasive high-frequency vascular ultrasound elastography. Phys Med Biol. 2005;50(7):1611-28.
223. Darling RC, Messina CR, Brewster DC, Ottinger LW. Autopsy study of unoperated abdominal aortic aneurysms. The case for early resection. Circulation. 1977;56(3 Suppl):II161-4.
224. Hall AJ, Busse EF, McCarville DJ, Burgess JJ. Aortic wall tension as a predictive factor for abdominal aortic aneurysm rupture: improving the selection of patients for abdominal aortic aneurysm repair. Ann Vasc Surg. 2000;14(2):152-7.
225. Coutu JM, Fatimi A, Berrahmoune S, Soulez G, Lerouge S. A new radiopaque embolizing agent for the treatment of endoleaks after endovascular repair: influence of contrast agent on chitosan thermogel properties. J Biomed Mater Res B Appl Biomater. 2013;101(1):153-61.
226. Destrempes F, Meunier J, Giroux MF, Soulez G, Cloutier G. Segmentation of plaques in sequences of ultrasonic B-mode images of carotid arteries based on motion estimation and a Bayesian model. IEEE Trans Biomed Eng. 2011;58(8).
227. Canadian Council on Animal Care, Olfert ED, Cross BM, McWilliam AA. Guide to the Care and Use of Experimental Animals. Volume 1, 2nd Edition. 2020 [Available from: https://www.ccac.ca/Documents/Standards/Guidelines/Experimental_Animals_Vol1.pdf]. (Accessed October 1, 2020.)

228. Fenwick N, Griffin G, Gauthier C. The welfare of animals used in science: how the "Three Rs" ethic guides improvements. The Canadian Veterinary Journal. 2009;50(5):523-30.
229. Alturkistani H, Bertrand-Grenier A, Salloum E, Cloutier G, Lerouge S, Soulez G. Quasi-static ultrasound elastography characterization of thrombus maturation in the aneurysmal sac after embolization of endoleaks with chitosan gels. 15ième Congrès annuel de la Société des sciences vasculaires du Québec. 2015 Quebec, Canada.
230. Alturkistani H, Bertrand-Grenier A, Salloum E, Cloutier G, Lerouge S, Soulez G. Quasi-static ultrasound elastography characterization of thrombus maturation in the aneurysmal sac after embolization of endoleaks with chitosan gels. 101st Radiological Society of North America Scientific Assembly and Annual Meeting. 2015; Chicago, Illinois.
231. Portney LG, Gross G. Measurement Revisited: Reliability and Validity Statistics. Foundations of Clinical Research : Applications to Evidence-based Practice. 4 ed. Philadelphia, PA: F.A. Davis.; 2020. p. 486-508.
232. Khosla S, Morris DR, Moxon JV, Walker PJ, Gasser TC, Golledge J. Meta-analysis of peak wall stress in ruptured, symptomatic and intact abdominal aortic aneurysms. Br J Surg. 2014;101(11):1350-7; discussion 7.
233. Harter LP, Gross BH, Callen PW, Barth RA. Ultrasonic evaluation of abdominal aortic thrombus. J Ultrasound Med. 1982;1(8):315-8.
234. Wang DH, Makaroun MS, Webster MW, Vorp DA. Effect of intraluminal thrombus on wall stress in patient-specific models of abdominal aortic aneurysm. J Vasc Surg. 2002;36(3):598-604.
235. Hinnen JW, Koning OH, Visser MJ, Van Bockel HJ. Effect of intraluminal thrombus on pressure transmission in the abdominal aortic aneurysm. J Vasc Surg. 2005;42(6):1176-82.
236. Piechota-Polanczyk A, Jozkowicz A, Nowak W, Eilenberg W, Neumayer C, Malinski T, et al. The abdominal aortic aneurysm and intraluminal thrombus: Current concepts of development and treatment. Front Cardiovasc Med. 2015;2:19-.
237. Wolf YG, Thomas WS, Brennan FJ, Goff WG, Sise MJ, Bernstein EF. Computed tomography scanning findings associated with rapid expansion of abdominal aortic aneurysms. J Vasc Surg. 1994;20(4):529-35; discussion 35-8.
238. Haller SJ, Crawford JD, Courchaine KM, Bohannan CJ, Landry GJ, Moneta GL, et al. Intraluminal thrombus is associated with early rupture of abdominal aortic aneurysm. J Vasc Surg. 2018;67(4):1051-8.e1.
239. Kumar DR, Hanlin E, Glurich I, Mazza JJ, Yale SH. Virchow's contribution to the understanding of thrombosis and cellular biology. Clin Med Res. 2010;8(3-4):168-72.

240. Parsi K, Exner T, Low J, Fung Ma DD, Joseph JE. In vitro effects of detergent sclerosants on clot formation and fibrinolysis. Eur J Vasc Endovasc Surg. 2011;41(2):267-77.
241. Xenos ES, Stevens SL, Freeman MB, Pacanowski JP, Cassada DC, Goldman MH. Distribution of sac pressure in an experimental aneurysm model after endovascular repair: the effect of endoleak types I and II. J Endovasc Ther. 2003;10(3):516-23.
242. Timaran CH, Ohki T, Veith FJ, Lipsitz EC, Gargiulo NJ, 3rd, Rhee SJ, et al. Influence of type II endoleak volume on aneurysm wall pressure and distribution in an experimental model. J Vasc Surg. 2005;41(4):657-63.
243. Ajjan R, Standeven K, Khanbhai M, Phoenix F, Gersh K, Weisel J, et al. Effects of aspirin on clot structure and fibrinolysis using a novel in vitro cellular system. Arterioscler Thromb Vasc Biol. 2009;29(5):712-7.
244. van Dam EA, Dams SD, Peters GWM, Rutten MCM, Schurink GWH, Buth J, et al. Non-linear viscoelastic behavior of abdominal aortic aneurysm thrombus. Biomech Model Mechanobiol. 2008;7(2):127-37.
245. Wang DH, Makaroun M, Webster MW, Vorp DA. Mechanical properties and microstructure of intraluminal thrombus from abdominal aortic aneurysm. J Biomech Eng. 2001;123(6):536-9.
246. Hinnen JW, Koning OH, van Bockel JH, Hamming JF. Aneurysm sac pressure after EVAR: the role of endoleak. Eur J Vasc Endovasc Surg. 2007;34(4):432-41; discussion 42-3.
247. Dias NV, Ivancev K, Resch TA, Malina M, Sonesson B. Endoleaks after endovascular aneurysm repair lead to nonuniform intra-aneurysm sac pressure. J Vasc Surg. 2007;46(2):197-203.
248. Landis JR, Koch GG. The measurement of observer agreement for categorical data. Biometrics. 1977;33(1):159-74.
249. Abbott WM, Callow A, Moore W, Rutherford R, Veith F, Weinberg S. Evaluation and performance standards for arterial prostheses. J Vasc Surg. 1993;17(4):746-56.